Lab on a Chip

ROYAL SOCIETY OF CHEMISTRY

CRITICAL REVIEW

View Article Online
View Journal | View Issue

Cite this: *Lab Chip*, 2026, **26**, 1610

A deep dive into hydrodynamic dispersion in microfluidic systems

Seyed Nezameddin Ashrafizadeh, * Mahdi Khatibi and Iman Aslani

Hydrodynamic dispersion of solutes is a pivotal phenomenon in microfluidic systems, wherein the axial spreading of various dissolved species—including ions, chemical compounds, biomolecules, dyes, pharmaceuticals, and nanoparticles—occurs due to the coupled effects of molecular diffusion and the non-uniform velocity profiles inherent to confined laminar flows. Given its profound impact on a broad range of applications—spanning analytical, diagnostic, bioengineering, pharmaceutical, environmental, and chemical processing systems—mastering the mechanisms of dispersion is crucial for enhancing separation efficiency, reproducibility, reaction performance, and analytical throughput, while minimizing sample volume, energy consumption, and undesired side effects. This comprehensive review provides a structured synthesis of the fundamental concepts, historical development, and governing mechanisms underlying Taylor–Aris dispersion in micro- and nanofluidic systems. Special emphasis is placed on the role of flow profile design, channel cross-sectional geometry, and surface physicochemical properties in modulating dispersion intensity. Through a systematic analysis of analytical, numerical, and experimental studies conducted from 2000 to 2025, we identify prevailing challenges, unresolved questions, and methodological gaps in the literature. Notably, this work addresses a key void by offering the first coherent classification that concurrently explores the mechanistic origins and engineering control strategies of hydrodynamic dispersion across diverse operating regimes. By bridging classical theories with emerging microfluidic architectures, this article not only deepens the understanding of dispersion phenomena but also lays the foundation for future innovations in colloid and interface science. As such, it provides an essential resource for researchers aiming to optimize transport, separation, and energy conversion processes in advanced fluidic systems.

Received 12th September 2025,
Accepted 10th November 2025

DOI: 10.1039/d5lc00869g

rsc.li/loc

1. Introduction

Microfluidic systems emerged in the late 1980s and early 1990s as a promising and transformative technology at the intersection of miniaturization, fluid dynamics, and analytical science. Operating across micrometer, nanometer, and even millimeter scales, these systems allow for the precise manipulation and control of fluid flows and suspended particles at small volumes and short timescales.[1–4] Initially developed within the context of microelectromechanical systems (MEMS) and subsequently integrated into micro total analysis systems (μTAS), microfluidics has rapidly evolved into a multidisciplinary research field.[5–7]

The convergence of MEMS and μTAS technologies has endowed microfluidic systems with several distinctive advantages: high surface-to-volume ratios, low power

Research Lab for Advanced Separation Processes, Department of Chemical Engineering, Iran University of Science and Technology, Narmak, Tehran 16846-13114, Iran. E-mail: ashrafi@iust.ac.ir, m_khatibi@alumni.iust.ac.ir, iman_aslani@chemeng.iust.ac.ir

Seyed Nezameddin Ashrafizadeh

Prof. Seyed Nezameddin Ashrafizadeh is a faculty member at the School of Chemical Engineering in Iran University of Science and Technology. His research lies at the intersection of advanced separation processes, surface science, electrokinetic transport, and microfluidics. He leads multidisciplinary efforts to harness surface-driven and electrokinetic mechanisms for enhanced transport, mixing, and reaction at micro- and nanoscale dimensions. Prof. Ashrafizadeh's work spans from theoretical modeling to experimental validation, bridging fundamentals with real-world applications in energy, environment, and biomedical systems. A distinguished researcher and mentor, he continues to advance innovation in micro/nanofluidics and interfacial transport phenomena.

consumption, reduced sample and reagent usage, high resolution and efficiency, low fabrication costs, and rapid process response times. These features have collectively enabled significant improvements in chemical reaction kinetics, species separation, biochemical detection, and enhanced control over analyte dispersion, mass transport, heat transfer, and momentum exchange within confined microscale domains.[8–10]

Typically constructed as micro- or nanochannels integrated onto small chips, microfluidic platforms are fabricated using a variety of substrates such as glass, silicon, and polymers—including polydimethylsiloxane (PDMS), one of the most widely used materials in soft lithography and microdevice fabrication.[11,12] The breadth of their applications spans diverse areas including biomedicine, analytical chemistry, pharmaceutical engineering, and environmental diagnostics. Key examples include molecular and cellular purification, microscale sample analysis and separation,[11] mixing and dispersion of ionic, neutral, and biochemical analytes,[13,14] controlled drug release *via* capillary vascular networks,[15,16] protein and DNA synthesis, cell culture,[17] nano-drug screening,[18] medical and environmental sensing,[19] capillary electrophoresis,[20] energy generation,[21–24] tissue engineering,[25] size-based particle and cell sorting through passive pinched-flow separation,[26] and membrane desalination processes.[27]

Commercial applications have also flourished, with innovations such as lab-on-a-chip (LOC) systems, microvalves, micropumps, microreactors, and micromixers now forming the backbone of numerous integrated platforms.[28–31] Among these various functions, the dispersion and transport of biological and chemical species—and especially the ability to control such dispersion—has recently emerged as a focal point of research interest within the microfluidics community.

Electrokinetics and microfluidics are intrinsically linked, as electrokinetic science investigates the behavior and interactions of charged species under the influence of electric fields at micro- and nanoscale dimensions. When an external electric field interacts with the electric double layers (EDLs) formed at the interface between an electrolyte solution and solid channel walls, a range of electrokinetic phenomena can emerge within microfluidic systems.[32,33]

Electrokinetic effects are commonly classified based on the presence or absence of an externally applied driving force and the mobility of the dispersed phase. In the presence of an applied electric field, active electrokinetic phenomena such as electroosmosis, electrophoresis, and dielectrophoresis are induced, enabling controlled transport of charged particles or fluids. Conversely, passive electrokinetic phenomena do not require an external field; instead, they arise due to inherent gradients within the system—such as concentration, pressure, or temperature gradients—which give rise to internally induced electric fields *via* mechanical fluxes. Examples include streaming potential, sedimentation potential, and thermoelectric migration under various gradient-driven conditions.[34,35]

Among these diverse electrokinetic mechanisms, pressure-driven flow and electroosmotic flow are particularly fundamental. Together, they play a pivotal role in driving solute transport, dispersion, separation, and analysis within micro- and nanofluidic channels. Their combined or competing effects govern the mobility and distribution of ions, pharmaceutical compounds, and biomolecules, making them central to both theoretical modeling and practical applications in microfluidic platforms.

Mahdi Khatibi

Dr. Mahdi Khatibi is a researcher in Chemical Engineering whose work focuses on electrokinetic transport, micro/nanofluidic systems, and energy conversion. He earned his Ph.D. from Iran University of Science and Technology, where he developed advanced models of electroosmotic flow and dispersion in soft nanochannels. His research combines theory, simulation, and design optimization using CFD tools to explore microscale separation, blue energy generation, and dynamic fluid control. Dr. Khatibi's interdisciplinary approach integrates transport physics with smart system design, contributing to the development of next-generation lab-on-a-chip and membrane technologies.

Iman Aslani

Iman Aslani received his B.Sc. in Chemical Engineering and is currently pursuing his M.Sc. at Iran University of Science and Technology, specializing in separation processes and microscale transport phenomena. His research focuses on electrokinetic dispersion and solute transport in micro- and nanoscale systems, emphasizing modeling and simulation. He explores how surface charge, channel geometry, and external fields influence analyte dispersion in microchannels, with implications for drug delivery, biosensing, and analytical microfluidics. Aslani's work reflects a strong theoretical foundation and growing expertise in computational micro/nanofluidics.

The dispersion of biological, ionic, neutral, and chemical species—such as bacteria, viruses, cells, proteins, metal ions, pharmaceutical compounds, gases, and nanoparticles—within microfluidic flows is governed by several factors, including fluid flow characteristics and environmental or interfacial conditions.[36–38] Among the dispersion mechanisms, hydrodynamic dispersion—commonly referred to as Taylor dispersion—is a well-established physical phenomenon resulting from the combined effects of two dominant mechanisms: (1) shear-induced advection due to non-uniform velocity profiles in laminar flows, and (2) molecular diffusion caused by the random thermal motion of solute molecules in the fluid. This phenomenon typically occurs in micro- and nanochannels, capillaries, and conduits under steady-state flow regimes.

Taylor dispersion arises when solutes spread along the flow direction under the influence of both mechanisms: the parabolic velocity profile associated with laminar flow causes differential axial transport, while cross-sectional molecular diffusion acts to redistribute solute molecules from regions of high to low concentration. These processes occur concurrently along the axial (flow) direction and across the radial (transverse) direction of the channel geometry.[39–42]

The contribution of velocity profile non-uniformity is particularly significant under low Reynolds number conditions. In such regimes, the axial velocity varies radially across the channel cross-section—reaching its maximum at the centerline and approaching zero near the walls due to the no-slip boundary condition. This velocity gradient results in solutes being advected at different speeds, creating an asymmetric radial concentration distribution and ultimately an axial spreading of the analyte band. Meanwhile, radial molecular diffusion mitigates these concentration gradients by promoting solute transport from regions of higher concentrations to lower concentrations, effectively acting as a homogenizing agent.[43,44]

The interplay between these mechanisms produces an effective axial dispersion that significantly exceeds what would be expected from molecular diffusion alone. Therefore, in analytical and separation-based microfluidic systems, it is crucial to minimize this enhanced longitudinal spreading to avoid excessive broadening of the analyte bands. Ideally, the flow should transition from a parabolic (Poiseuille) velocity profile toward a more uniform, plug-like profile, thereby improving resolution, analytical efficiency, and the precision of downstream processes.

The phenomenon of hydrodynamic dispersion was first elucidated by G. I. Taylor (1953)[45] and later generalized by R. Aris (1956),[46] forming the classical Taylor–Aris framework that links convective shear and molecular diffusion in laminar flow. This theory laid the groundwork for understanding solute band broadening in confined channels and remains the cornerstone of modern microfluidic transport analysis. This foundational theory has since been extended by numerous researchers to accommodate more complex conditions and system architectures. Investigations have explored solute dispersion under non-Poiseuille flow profiles,[47–50] various microchannel cross-sectional geometries,[51] different fluid types,[52] and the influence of external forces such as alternating and direct electric fields, as well as magnetic fields.[53–55] Additional studies have also examined the effects of different boundary conditions at the channel walls,[56–59] among other parameters—all of which are comprehensively reviewed in this article.

Fig. 1 illustrates the number of publications related to Taylor dispersion indexed in the Scopus database from 2000 to the present. As seen, there has been a gradual increase in research output from 2000 to 2013, with a peak occurring in 2012 and 2013. Following this period, a slight decline was observed until 2019, after which interest resurged, resulting in a renewed upward trend in recent years. Notably, many recent efforts have focused on modulating Taylor dispersion through various control parameters in different microfluidic systems, further emphasizing the need for a unified and analytical review such as the present work.

In modern microfluidic systems—particularly those involving analytical separations, sample mixing, and diagnostic analysis—the dispersion of analyte bands plays a critical role in overall system performance. Uncontrolled dispersion of solute species within analyte bands can lead to significant degradation in separation quality, reduced detection accuracy, lower throughput, and diminished operational efficiency.[60] Therefore, a comprehensive understanding of the underlying mechanisms of Taylor dispersion, coupled with the strategic application of dispersion control techniques, is essential for achieving precise, targeted solute transport in microfluidic environments.

A variety of strategies have been developed to mitigate or modulate Taylor dispersion in microscale systems. These approaches can be broadly classified into primary and alternative (secondary) methods. Primary strategies often

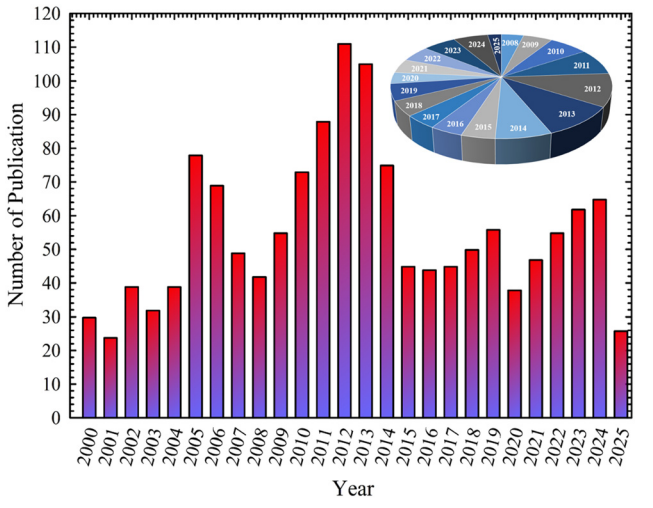

Fig. 1 Trends in the number of publications related to Taylor dispersion from 2000 to 2025 based on the Scopus database. The search included the keywords: "dispersion", "Taylor dispersion", "Taylor–Aris dispersion", "Taylor dispersion analysis", "mass transport", "solute transport", and "dispersion coefficient".

involve direct manipulation of wall properties, such as varying the surface zeta potential, introducing structured wall roughness or patterned topography, modifying slip lengths, enabling heterogeneous chemical reactions, tuning adsorption–desorption dynamics, or adjusting the physicochemical properties of polyelectrolyte layers and electrolyte solutions.

In parallel, alternative control routes include geometric modifications of the channel cross-section, the inclusion of nanoparticles or suspended phases, the use of alternating (AC) rather than direct (DC) electric fields, tailoring dimensionless numbers to match system-specific operating regimes, and introducing transverse or secondary flows across the channel's radial cross-section. These approaches collectively offer a robust and versatile toolkit for fine-tuning dispersion behavior under diverse conditions.[61–65]

Taylor hydrodynamic dispersion finds applications in a wide range of technologies, including microfluidic separation devices, targeted drug delivery systems (particularly for minimizing off-target diffusion in bloodstream transport), chromatographic columns, capillary electrophoresis (CE), lab-on-a-chip (LOC) and lab-on-a-disk (LOD) platforms, mass transport in porous media, environmental engineering, biological diagnostics, microscale mixing processes, and beyond.[66–71] Fig. 2 presents a comprehensive classification of Taylor dispersion based on its governing mechanisms, application domains, and both primary and secondary control strategies.

To contextualize the contribution of this review, we briefly contrast it with representative recent surveys that address related but narrower aspects of micro/nanofluidic transport and mixing. Tutorial and measurement-oriented treatments of Taylor dispersion and Taylor-dispersion analysis provide indispensable guidance for quantifying band broadening in capillaries and channels.[72] Physics-oriented reviews of micromixing summarize mechanisms and passive/active mixer designs aimed at enhancing local interfacial deformation and mixing.[73] Computational reviews clarify multiscale numerical approaches to electroosmotic and nanopore transport where electrostatics–hydrodynamics coupling is.[74] Reviews focused on device geometry and experimental design synthesize how channel layouts and mixer architectures determine residence time distributions and mixing quality.[17] Finally, surveys of polyelectrolyte and soft-surface engineering summarize how responsive surface layers alter near-wall partitioning, slip, and interfacial electrostatics.[75] Importantly, while these authoritative reviews deepen our understanding of individual themes, none provides a cross-regime mechanistic control synthesis that (i) classifies the physical origins of longitudinal dispersion across pressure-driven, electroosmotic and hybrid flows, (ii) quantifies the parametric limits in which each mechanism dominates (*e.g.*, thin *vs.* thick EDL, Pe regimes, viscoelastic effects), and (iii) maps those mechanisms to explicit engineering levers (geometry, surface chemistry/PEL design, zeta/slip modulation, AC/oscillatory actuation, and numerical optimization workflows). The present review fills that gap by offering an integrated conceptual map linking physics, modelling practices, and actionable design strategies for dispersion management in lab-on-a-chip devices.

This review article presents a comprehensive and in-depth overview of the evolution of Taylor dispersion—from its theoretical origins to the elucidation of its governing mechanisms, control strategies under diverse flow scenarios,

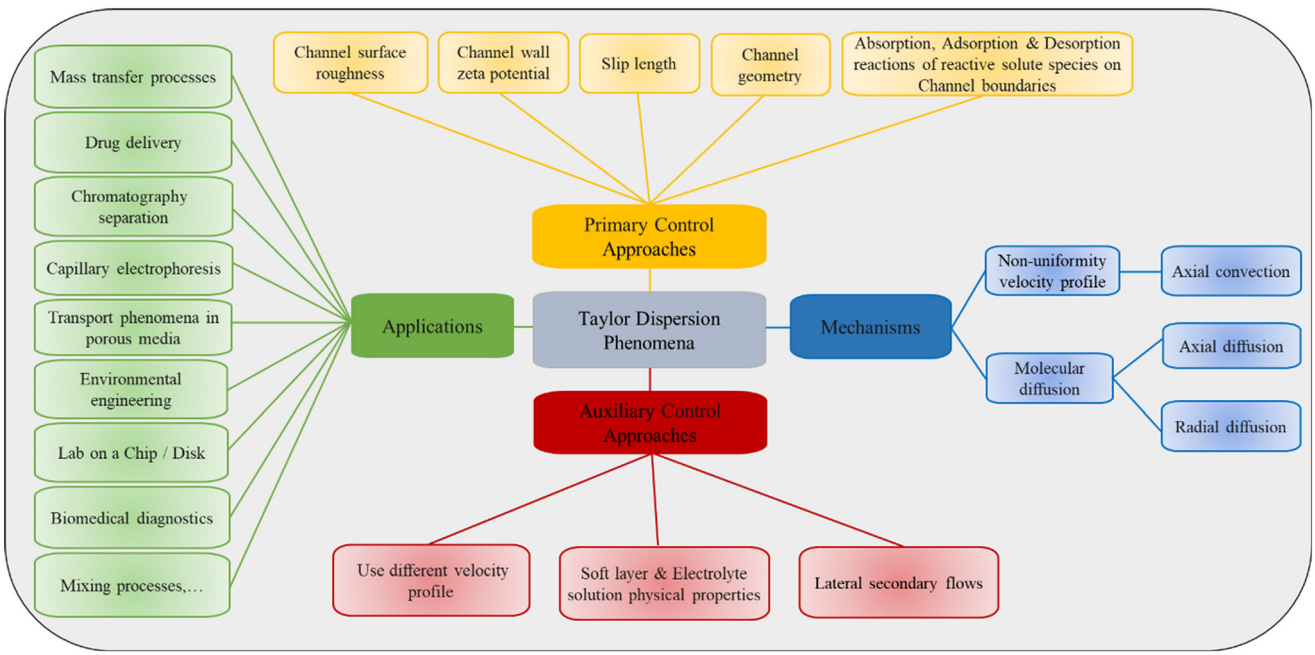

Fig. 2 Schematic overview illustrating the relationships among the governing mechanisms, primary and alternative control strategies, and the wide-ranging applications of Taylor dispersion across various scientific and engineering domains.

influential parameters, and practical implementations in microfluidic systems from 2000 to 2025. Building upon the valuable contributions of earlier studies, the present work seeks to unify past findings with recent advancements and emerging themes, thereby offering a consolidated and updated perspective on the state of the art in Taylor dispersion research.

As illustrated in Fig. 3, the number of publications related to this topic has significantly increased between 2000 and 2025, with the majority originating from disciplines such as chemistry, chemical engineering, and selected branches of engineering. This review also aims to critically analyze and compare both numerical and experimental studies, shedding light on the fundamental aspects of the phenomenon and exploring the technical and scientific challenges that remain unresolved. Furthermore, this article thoroughly discusses the multitude of parameters influencing Taylor dispersion, highlights approaches to control and mitigate its effects, and surveys its wide-ranging applications in various systems and operational settings. By integrating the dispersed literature into a coherent framework, this work seeks to offer a holistic understanding of the phenomenon, identify persistent research gaps, and propose forward-looking directions for future investigations.

It is worth noting that despite extensive theoretical advancements, the commercial translation of Taylor dispersion-based technologies remains limited, primarily due to the incomplete understanding of some underlying mechanisms and practical challenges. Addressing these gaps is essential for bridging the divide between academic research and real-world implementation. The renewed need for a unified review arises from the rapid evolution of microfluidic technologies that extend far beyond the assumptions of classical Taylor–Aris dispersion. Modern lab-on-a-chip systems increasingly integrate AI-guided design optimization, multi-field actuation (electro-, magneto-, and acoustic-driven flows), and the manipulation of non-Newtonian and nanoconfined fluids. These developments have transformed the context in which dispersion operates—from a purely theoretical phenomenon to a key performance determinant in smart and adaptive microfluidic platforms. The present review thus aims to bridge the classical foundations of hydrodynamic dispersion with the emerging paradigms shaping next-generation micro- and nanofluidic applications.

2. Fundamentals of hydrodynamic dispersion in microfluidic systems

2.1. Origins and foundational theory of Taylor dispersion

Taylor demonstrated that the effective dispersion coefficient, which governs the long-term rate of band broadening, is strongly influenced by the axial variation in the velocity profile. He showed that this coefficient is dependent on the axial position and scales with the square of the Peclét number. The classical expression for Pe includes the average flow velocity, characteristic channel length (*e.g.*, radius or width), and molecular diffusion coefficient.[76]

It is important to note that in microfluidic systems involving electrokinetically driven flows—such as electroosmotic or pressure-assisted flows—alternative

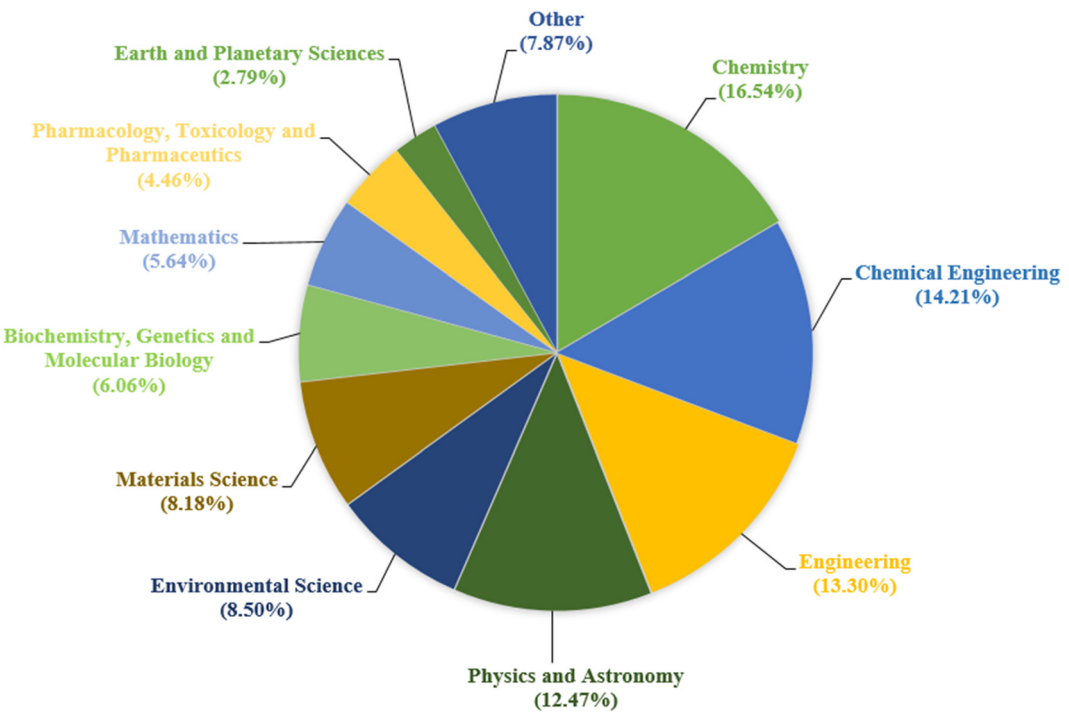

Fig. 3 Disciplinary distribution of scientific contributions related to Taylor dispersion, highlighting the relative share of different fields in advancing the understanding and significance of this phenomenon.

characteristic velocities can replace the conventional average flow velocity in the definition of the Peclét number, depending on the governing transport mechanism. As shown in eqn (1), the general expression for the Taylor dispersion coefficient, which accounts for both flow and channel geometry, has been widely used to characterize solute dispersion in micro- and nanofluidic environments.[69]

$$D_{TH} = 1 + \frac{Pe^2}{a} \quad (1)$$

where, D_{TH}, Pe, and a represent the Taylor hydrodynamic dispersion coefficient, the Peclét number, and a dimensionless constant, respectively. It is important to note that the value of the constant a depends on the velocity profile and the cross-sectional geometry of the flow channel. For instance, in the case of classical Poiseuille flow through a circular tube, a takes the value of 48. However, this value varies for other velocity profiles and non-circular geometries, reflecting the influence of flow field characteristics on the extent of dispersion.

One of the key contributions of Aris in refining Taylor's model was the introduction of the concept of the effective dispersion coefficient, commonly denoted as K_{eff}, also known as the Taylor–Aris effective diffusivity. Aris demonstrated that this coefficient is obtained by summing the molecular diffusion coefficient and the hydrodynamic dispersion term derived from Taylor's analysis (as presented in eqn (1)), leading to the generalized formulation expressed in eqn (2). This formulation revealed that the effective dispersion in the axial direction is greater than the molecular diffusion alone by an amount equal to the Taylor hydrodynamic dispersion contribution. In essence, the Taylor–Aris effective dispersion quantifies the total spreading of solute species as a combined outcome of molecular-scale diffusion and convective effects driven by non-uniform flow.

$$K_{eff} = D_m + D_{TH} = D_m\left(1 + \frac{D_{TH}}{D_m}\right) = D_m\left(1 + f_g f_v \hat{D}_{TH} Pe^2\right) \quad (2)$$

According to eqn (2), K_{eff} represents the Taylor–Aris effective dispersion coefficient, while $\hat{D}_{TH} = \frac{D_{TH}}{\left(\frac{d^2 U^2}{D_m}\right)}$ is the normalized form of the Taylor hydrodynamic dispersion term. In this formulation, f_g denotes the geometric factor and f_v denotes the velocity profile factor. These parameters vary depending on the channel cross-sectional geometry—such as rectangular, circular, trapezoidal, elliptical, or parallel plate configurations—as well as the flow-driving mechanisms, including electroosmotic, pressure-driven, magnetic, or hybrid flows.[77,78] For instance, in a parallel-plate channel with pressure-driven flow, the velocity profile factor f_v equals 1.210, and the geometric factor f_g is 1. Naturally, for other geometries and flow conditions, these values differ and must be determined accordingly. As seen in eqn (2), when the ratio $\hat{D}_{TH}Pe^2$—that is, the normalized Taylor dispersion relative to molecular diffusivity—is significantly greater than 1, or equivalently when the molecular diffusion coefficient is small, the hydrodynamic (Taylor) dispersion resulting from velocity field non-uniformity becomes the dominant mechanism over molecular diffusion.[79]

2.2. Historical development of the Taylor dispersion phenomenon

Building upon the foundational Taylor–Aris framework, subsequent research progressively expanded its applicability to unsteady, electroosmotic, and magnetohydrodynamic flows. Over the decades, this evolution has enabled modeling of increasingly complex microscale transport phenomena. Fig. 4 illustrates the evolution of Taylor dispersion research, highlighting the progression from foundational theories to advanced analytical, numerical, and—though limited—experimental investigations.

In subsequent years, researchers expanded upon Taylor's original model by examining solute dispersion under unsteady (time-dependent) flow conditions across all time scales following solute injection—moving beyond the steady-state assumptions made by Taylor.[80,81] In 1983, Watson[82] conducted one of the first analytical investigations of Taylor dispersion in oscillatory flows through circular tubes and two-dimensional channels. He derived a formula for the effective axial dispersion coefficient under oscillatory conditions and demonstrated that it is possible to analytically determine the solute flux for any oscillation frequency—thus enabling precise analysis of how oscillatory motion affects mass transfer.

With the rise of interest in oscillatory and pulsatile flows and their pronounced influence on solute dispersion, numerous studies have since investigated Taylor dispersion under such conditions—both in isolation and in combination with electroosmotic,[83,84] Couette,[85] and electromagnetohydrodynamic flows,[86–88] as well as with steady-state flows.[89] These investigations have also incorporated effects such as reversible and irreversible wall adsorption, boundary slip, and non-Newtonian fluid behavior, aiming to improve mass transport, separation, drug delivery, and mixing performance in microscale channels of various geometries.

In 1989, Frankel and Brenner[90] proposed the generalized Taylor dispersion theory (GTDT) to extend classical Taylor–Aris theory to more complex environments—including porous media, chromatographic separations, heat transfer in cellular structures, and flow systems with non-ideal velocity profiles. This theory provided a broader and more versatile framework for modeling convection–diffusion phenomena in real-world systems. One of the earliest numerical and analytical studies of electroosmotic flow-based dispersion in microchannels was conducted by Griffiths and Nilson,[91] who examined the electric potential, velocity field, and long-term solute distribution of a neutral, non-reactive species at high zeta potentials. Later, in 2003, Zholkovskij *et al.*[92] explored

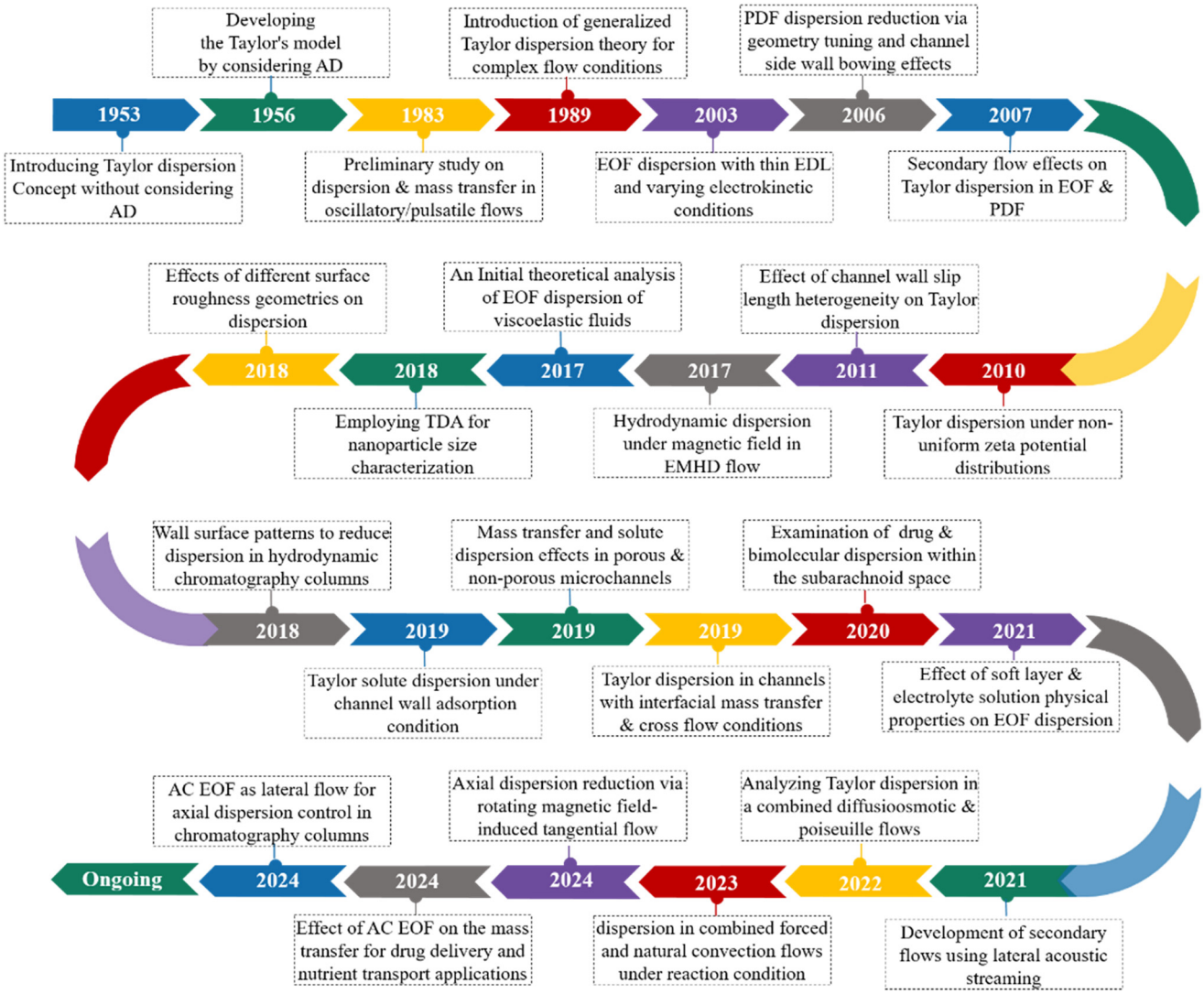

Fig. 4 Historical timeline and evolutionary progress of key scientific advancements related to Taylor dispersion, highlighting major studies and impactful innovations that have contributed to improved modeling and deeper understanding of the phenomenon under various conditions.

dispersion in electroosmotic flows using the thin Debye layer approximation, evaluating the effects of various applied electric potentials, electrolyte concentrations, and channel geometries. Zholkovskij and Masliyah[93] further extended this model to account for combined pressure-driven and electroosmotic flows. In 2006, Dutta *et al.*[94] investigated solute dispersion in microchannels with isotropic secondary surface structures and showed that optimized side-wall patterns in curved and twisted channels could significantly reduce dispersion in pressure-driven flows.

Shortly thereafter, Zhao and Bau[95] examined the influence of secondary flows on Taylor dispersion under combined electroosmotic and pressure-driven flow. They demonstrated that secondary (transverse) flows enhance lateral mixing and cross-sectional mass transfer, thereby reducing axial dispersion. Building on this idea, Adrover[96] extended the study of secondary flow effects to infinitely wide channels at high Peclét numbers, further deepening our understanding of dispersion mechanisms in complex microscale flow systems.

In 2010, Zholkovskij *et al.*[97] conducted one of the first investigations into how spatial variations in wall zeta potential affect analyte band broadening in electroosmotic flow through submicron channels. The following year, Ng[61,77] extended this concept to circular microchannels by incorporating both gradually varying zeta potential and differential hydrodynamic slip conditions along the channel walls. His findings highlighted that the greater the difference in wall slip lengths, the more pronounced the hydrodynamic dispersion becomes. In 2017, Vargas *et al.*[76] developed a model for hydrodynamic dispersion in parallel-plate microchannels by combining the effects of spatially varying zeta potential with coupled electroosmotic and magnetohydrodynamic flows. They demonstrated that two key parameters—the Hartmann number and the ratio of the channel half-height to the Debye length—play a critical role in determining solute dispersion under the

influence of magnetic fields. In a related study, Hoshyargar *et al.*[98] examined the impact of fluid elasticity on electroosmotic dispersion in slit microchannels. Focusing on viscoelastic (non-Newtonian) fluids with symmetric and constant zeta potentials, they found that fluid rheology significantly affects dispersion characteristics. In 2018, Dejam *et al.*[99] proposed a comprehensive analytical solution to study shear dispersion in a coupled system consisting of a porous matrix and a slit-like channel with rough walls. Their model accounted for surface roughness as a function of both the Peclét number and geometric roughness parameters, offering new insights into wall-induced dispersion mechanisms across a range of geometries.

In another important advancement, Urban *et al.*[100] introduced Taylor dispersion analysis (TDA) as a powerful technique for measuring the diffusion coefficients of small molecules and proteins, as well as for characterizing inorganic nanoparticles across different material types and size distributions. They demonstrated that TDA offers several advantages over other analytical techniques commonly used for nanoparticle characterization, such as dynamic light scattering (DLS) and transmission electron microscopy (TEM).

In light of the importance of minimizing axial dispersion and enhancing the separation efficiency of suspended particles with finite sizes, Adrover *et al.*[101] in 2018 conducted a case study focused on improving hydrodynamic chromatography performance. They theoretically applied a generalized version of Brenner's macrotransport framework by introducing a periodic sequence of slip and no-slip boundary strips along both longitudinal and transverse directions of microchannel walls. Their goal was to mitigate limitations and challenges in systems where microspheres exhibit imperfect confinement, and to compare results with conventional no-slip boundary conditions. Molecular adsorption on channel walls can also significantly influence hydrodynamic dispersion. To address this, Marbach and Alim[41] in 2019 proposed an analytical model that examined the active control of Taylor dispersion through various scenarios, including modulation of inlet velocity profiles, wall slip lengths, and especially solute adsorption along oscillating channel walls under Poiseuille flow. The oscillating (pulsating) wall boundaries were modeled to simulate periodic mechanical vibrations, which can dramatically alter solute transport and dispersion patterns. One of their key findings was that solute-wall adsorption affects Taylor dispersion nonlinearly, with the magnitude of dispersion strongly depending on the adsorption rate.

In another study, Dejam[50] in 2019 utilized a generalized Poiseuille flow equation originally proposed by Amatore *et al.*,[102] which incorporates a bluntness parameter that characterizes the sharpness or flatness of the velocity profile. A reduced-order model was developed to assess how different velocity profiles influence the hydrodynamic dispersion coefficient and convective–diffusive mass transport in microchannels with both porous and nonporous walls. The results revealed that, unlike pressure-driven flows, decreasing the bluntness parameter leads to reduced dispersion and mass transfer rates in electroosmotic flows. Also in 2019, Lin and Shaqfeh[103] applied perturbation theory, Brownian dynamics simulations, and a modified one-dimensional advection–diffusion–reaction equation to study the effects of crossflow and interfacial mass transfer on axial dispersion. They modeled a microchannel with a primary Poiseuille flow in the longitudinal direction and a secondary transverse flow across the channel width. Their results showed that Taylor dispersion is inversely proportional to the fourth power of the transverse flow velocity and directly proportional to the cube of the Brownian diffusion coefficient—implying that strong crossflow substantially suppresses dispersion.

In a further development, Li and Jian[104] carried out an analytical and time-dependent study of solute dispersion in 2019 using series expansion methods, homogenization theory, and Fourier transform solutions under the linearized Debye–Hückel approximation. Their model focused on an AC electroosmotic flow through a nanochannel coated with a polyelectrolyte layer and subject to surface slip boundary conditions. Their work shed light on the complex interplay between surface characteristics, electric field modulation, and solute transport dynamics in confined nanofluidic environments.

In 2020, Salerno *et al.*[38] conducted a compelling analytical and numerical investigation that combined the statistical moment method from Taylor–Aris theory with the Brinkman model to study both solute dispersion and flow dynamics in porous environments. Their work focused on predicting time-dependent dispersion coefficients for passive solutes, specifically within an annular cavity simulating the subarachnoid space. The model addressed drug and biomolecule dispersion under oscillatory cerebrospinal fluid (CSF) flow induced by intrathecal injection. Their findings have direct implications for optimizing drug delivery strategies in the central nervous system (CNS), allowing for more targeted, efficient, and precise treatment protocols while minimizing adverse side effects due to over- or under-dosing.

In 2021, Talebi and co-workers[105] examined solute dispersion in electroosmotic flow through soft microchannels, incorporating ion separation effects between the electrolyte and polyelectrolyte layers—an extension beyond earlier models such as that of Hoshyargar *et al.*[106] Their analysis accounted for mismatches in physical properties such as density, viscosity, and permittivity between the electrolyte solution and the soft interface.

From 2021 to 2024, several studies—both theoretical and experimental—focused on reducing Taylor–Aris axial dispersion by enhancing secondary crossflows. Researchers investigated acoustic streaming, tangential wall-driven rotation, and alternating current (AC) electroosmotic flow in the presence of wall retention effects. These efforts targeted

improvements in chemical separation efficiency, residence time uniformity in micromixers and microreactors, and mixing enhancement in low-Reynolds-number capillary flows. Notable studies include works by Gelin *et al.*,[63] Larbi *et al.*,[107] and Bihi *et al.*,[108] each contributing to applications such as vortex chromatography columns and sorption-based separation systems. While most Taylor dispersion studies have focused on flows driven by electroosmosis, pressure gradients, or pulsatile oscillations, much less attention has been given to alternative flow profiles. To address this gap, recent work—particularly from 2022 onward—has explored solute dispersion under diffusiophoretic and electrophoretic drift-driven conditions in colloidal suspensions.[109]

In 2023, Saha *et al.*[47] investigated tracer dispersion and spatiotemporal concentration profiles under combined forced and natural convection flows between parallel plates with thermal gradients, wall reactions, and adsorption effects. They employed Mei's multi-scale homogenization technique to derive effective dispersion coefficients in the presence of the grash of number, which quantifies buoyancy effects from thermal gradients. One of their key findings was that both cooling (negative grash of number) and heating (positive grash of number) influence axial and transverse concentration distributions, but the overall Taylor dispersion coefficient remains largely unaffected by the sign of the grash of number.

Finally, in a 2024 study, Kumar and De[53] analyzed the influence of AC electroosmotic flow profiles on neutral solute transport through porous-walled microtubes. Their work targeted mass and heat transfer enhancement, selective solute separation, and nutrient delivery in physiological and drug-delivery systems. They demonstrated that modulation of AC frequency could enhance solute permeation through porous walls by up to 13% compared to direct current (DC) fields, highlighting its potential for improving targeted and efficient mass transfer in engineered microfluidic systems.

Over the past seven decades, the understanding of Taylor dispersion has evolved from a classical theoretical framework into a diverse, multidimensional field with broad scientific and technological relevance. Beginning with the foundational models of Taylor and Aris, subsequent research has progressively addressed the limitations of idealized systems by incorporating unsteady flows, non-Newtonian fluids, wall interactions, magnetic and electric field effects, and porous geometries. These studies have enriched the theoretical landscape and advanced practical applications in drug delivery, microreactors, chromatography, and nanofluidics. Recent works, particularly from 2020 onward, have demonstrated a growing emphasis on dynamic boundary conditions, field-modulated flows, secondary crossflows, and surface-specific interactions—revealing the need for precise control strategies tailored to specific microfluidic functions. Despite the breadth of investigation, gaps remain in exploring non-conventional flow profiles and coupling effects in emerging nanostructured systems, underscoring both the complexity and continued relevance of Taylor dispersion as a field of active inquiry.

2.3. Mechanisms governing Taylor (hydrodynamic) dispersion

As discussed in earlier sections, Taylor dispersion—also known as hydrodynamic dispersion—is a fundamental phenomenon in numerous engineered and natural transport processes. It plays a dual role across various microfluidic and analytical systems. In separation and purification processes, Taylor dispersion often has a detrimental effect, as it broadens solute bands and reduces resolution, leading to lower separation efficiency and diminished operational accuracy. In contrast, in micromixing applications, this very same dispersion phenomenon becomes beneficial—enhancing species mixing, improving homogeneity, and accelerating reaction kinetics by promoting faster equilibrium.[110,111]

In microchemical and bioanalytical technologies—such as capillary electrophoresis, microchromatography, and lab-on-a-chip (LOC) systems—the impact of Taylor dispersion is context-dependent. While it can limit performance in systems sensitive to axial band broadening, it may also improve analytical throughput and sensitivity in cases where enhanced mixing or solute transport is desirable.[112,113] In LOC platforms, where separation and mixing must often occur concurrently or sequentially in confined geometries, achieving a balance between these opposing effects is critical. The challenge lies in optimizing both processes within the same system by understanding and managing the underlying transport mechanisms.

Ultimately, despite its occasionally beneficial role in specific micromixing applications, minimizing and controlling Taylor dispersion remains essential for improving the precision and efficiency of a wide range of microfluidic operations, especially those involving separations.[114] As previously mentioned, Taylor dispersion arises from the combined effects of convective transport (advection) and molecular diffusion.[115] While advection dominates solute motion along the flow direction, molecular diffusion contributes to solute spreading both axially and transversely. This interplay governs solute dispersion in diverse systems—including groundwater and river pollutant analysis,[116] microbial transport,[117] cross-flow filtration processes,[118] and even the design of chemical reactors at commercial scales.

Fig. 5 schematically illustrates how axial advection and radial diffusion jointly influence band broadening in a microfluidic channel under electroosmotic flow. The diagram captures a time-resolved sequence of solute pulse injection and its evolution through a parallel-plate microchannel filled with electrolyte solution. An external electric field, applied *via* a power source, generates an electroosmotic flow profile along the channel axis. The figure shows how solute band shape, centerline velocity, and cross-sectional concentration gradients evolve from the initial time $t = 0$ until a quasi-steady state is reached at long times. In the following

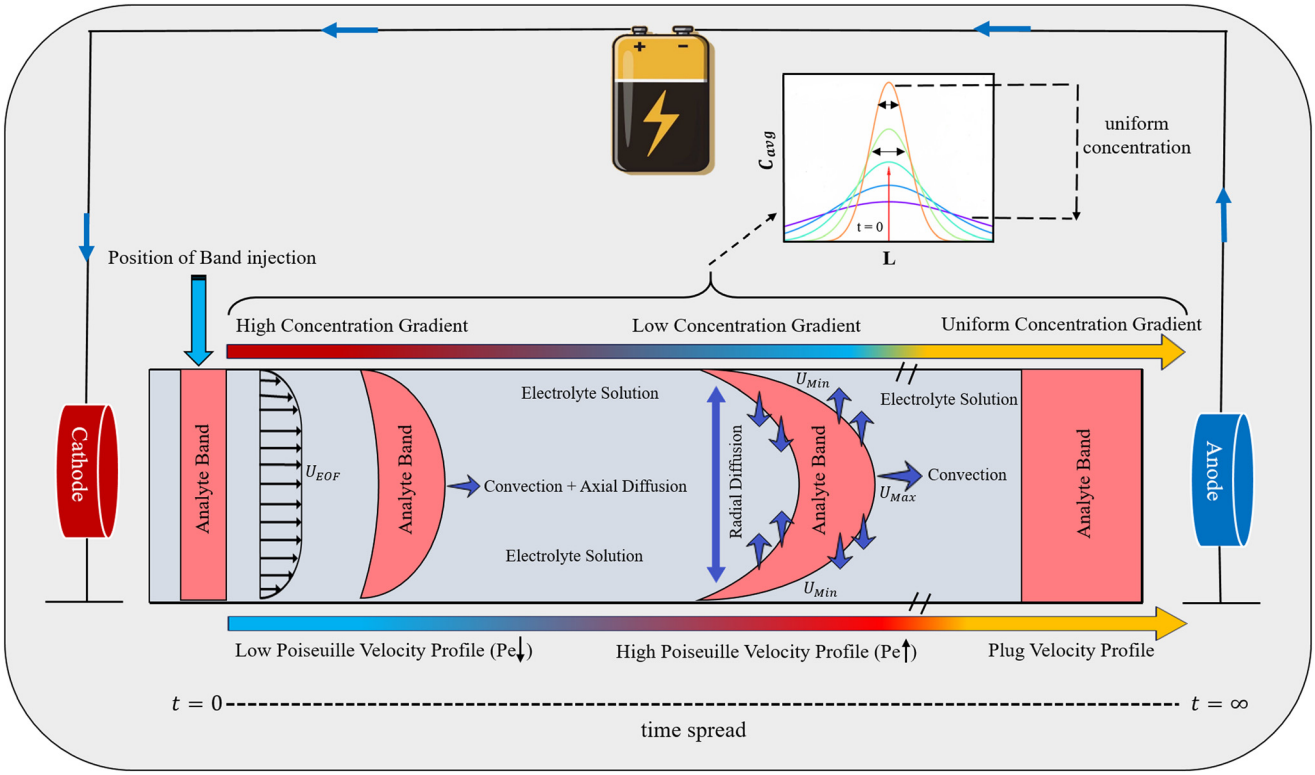

Fig. 5 Schematic representation of the spatiotemporal evolution of a neutrally charged analyte band injected into an electrolyte-filled microchannel under the combined influence of axial advection and molecular diffusion. An external electric field applied *via* electrodes induces an electroosmotic flow profile along the channel to control the relative motion of the analyte band and the fluid. Colored regions depict the degree of concentration gradient and velocity profile development over time: blue zones correspond to sharp radial concentration gradients and low Poiseuille-like velocity, red zones indicate higher concentration gradients and elevated flow velocities, while yellow zones represent uniform (plug-like) velocity and concentration profiles. Blue arrows inside the channel denote the key transport mechanisms: axial advection, axial diffusion, and transverse (radial) diffusion. The upper portion of the schematic illustrates the evolution of axial concentration profiles as a function of time.

subsections, we aim to develop a detailed and systematic understanding of the two core mechanisms—advection and diffusion—that govern Taylor dispersion, exploring their individual contributions and interactions under varying physical and operational conditions.

2.3.1. Effect of velocity profile non-uniformity on solute transport. The first mechanism responsible for Taylor dispersion in micro- and nanochannels arises from the non-uniform velocity profile across the channel cross-section, often referred to as the advection mechanism. To isolate the effects of advection and molecular diffusion on solute band transport, it is useful to examine each mechanism individually—first considering advection alone in the absence of diffusion, and subsequently analyzing diffusion independently, followed by their combined interaction. In the absence of molecular diffusion—particularly in the radial direction and during early to intermediate time scales—a neutrally charged analyte band with an initially uniform concentration begins to travel downstream upon instantaneous injection into the microchannel (as illustrated in Fig. 5).[119] As time progresses, the front and rear of the moving band gradually assume a parabolic shape due to the development of a Poiseuille velocity profile, especially under laminar flow conditions. This occurs because solute particles at different radial positions travel at different speeds: the velocity is highest at the channel center and lowest near the walls. This differential velocity leads to axial band stretching as various segments of the band are convected downstream at unequal rates.[120] For example, in cylindrical channels under pressure-driven flow, this non-uniformity in axial velocity causes solute molecules near the centerline to move more rapidly than those adjacent to the walls. With increasing mean flow velocity and elapsed time, the resulting dispersion becomes more pronounced, and the impact of the velocity profile non-uniformity becomes increasingly significant.[121]

Additionally, this non-uniform velocity distribution introduces a transverse concentration gradient within the solute band, which in turn induces a diffusive flux perpendicular to the flow direction. Consequently, the initial uniform radial concentration profile becomes distorted, further contributing to band broadening.[122] In essence, the non-uniformity of the velocity field is a primary factor underlying non-uniform solute distribution across the channel cross-section.

As seen in Fig. 5, the radial concentration gradient evolves from steep and asymmetric in the early stages to increasingly

uniform at later times. While this homogenization is ultimately achieved through radial molecular diffusion (discussed in the next section), the role of advection is dominant during the initial stretching phase. The concentration profile in the upper panel of Fig. 5 shows the temporal evolution of the analyte band: initially appearing as a sharp pulse (red peak), the variance of the profile decreases over time, eventually leading to a narrower, more uniform distribution. Meanwhile, the evolution of the velocity profile follows a different trajectory. Initially, the flow resembles a weak Poiseuille profile (at low Péclet numbers), but as the flow develops and Pe increases, the profile becomes increasingly parabolic. Eventually, at long times, the velocity distribution transitions toward a plug-like electroosmotic flow profile, minimizing axial dispersion and stabilizing the band shape.[123] Clearly, if the velocity field were fully uniform, the hydrodynamic dispersion would be substantially reduced. Although analyzing each mechanism in isolation is useful for understanding their individual roles, it is important to note that even in advection-dominated systems, axial molecular diffusion still contributes to overall dispersion. However, in pure fluid flows (*i.e.*, those free from structural barriers or porous media), axial diffusion plays a relatively minor role compared to advection. In contrast, in packed media or porous environments, axial diffusion can become significant. One study[124] specifically investigated the influence of axial diffusion on concentration distribution under these differing transport regimes.

2.3.2. Role of molecular diffusion in solute band transport. Diffusion refers to the random thermal motion of solute molecules that causes them to move from regions of higher concentration to regions of lower concentration.[125] In ionic systems, diffusion manifests in two distinct forms: mass diffusion—driven purely by stochastic molecular motion—and migrative diffusion, which occurs in response to an applied electric field. The resulting concentration gradients across narrow channels or capillaries, especially at the microscale, make diffusion one of the key mechanisms contributing to the broadening of solute bands across the transverse section of the channel. As illustrated in Fig. 5, molecular diffusion becomes particularly relevant in regions where axial stretching of the analyte band has already occurred due to advection. At the leading edge of the analyte pulse, the highest solute concentration is observed near the center of the channel. This radial concentration gradient induces outward molecular diffusion, causing solute molecules to migrate toward the channel walls. Since fluid velocity is significantly higher at the center than near the walls, this radial migration leads to a reduction in the average axial velocity of the solute molecules.

Conversely, at the trailing edge of the analyte band, the concentration distribution is reversed: higher near the walls and lower at the center. This reversed gradient causes inward radial diffusion toward the centerline, effectively increasing the average axial velocity of solute particles. Together, these opposing diffusion currents reduce the overall extent of axial band stretching that would otherwise result from advection alone. As the schematic arrows in Fig. 5 indicate, this radial molecular diffusion plays two essential roles:

- It counteracts excessive axial broadening caused by advection and axial diffusion, and
- It diminishes the overall effect of hydrodynamic dispersion.

In other words, once radial diffusion becomes significant, the front and rear regions of the solute band respectively slow down and speed up, compressing the band and making the axial distribution more compact and uniform than in cases governed purely by advection. Over time, the synergistic interaction between axial advection and radial diffusion leads to a cross-sectional homogenization of solute concentration. This process ultimately results in a symmetric, well-defined solute pulse with a longitudinal spread much larger than what would be observed in pure diffusion without flow. Hence, both mechanisms are essential for accurate modeling and control of mass transport and dispersion in microfluidic systems.[126]

With a clear understanding of the underlying mechanisms, one can now evaluate the relative dominance of advection or diffusion under different flow conditions. The Péclet number serves as the key dimensionless parameter for this purpose. It quantifies the relative importance of convective transport *versus* molecular diffusion. When the Péclet number is large—indicating high flow velocities—advection dominates the dispersion process. Conversely, at low Péclet numbers, molecular diffusion plays a more critical role in the axial transport of solute bands.

2.4. Analytical context and applications of Taylor dispersion analysis

Taylor dispersion analysis (TDA), grounded in the classical principles of Taylor dispersion, has emerged as a distinctive analytical and laboratory technique characterized by non-destructiveness, operational simplicity, independence from molecular identity, high sensitivity, and precise performance. It is widely employed for molecular characterization, particularly in the measurement of diffusion coefficients and hydrodynamic radii of solutes of varying sizes under well-controlled laminar flow conditions. This method has consistently attracted the interest of researchers across decades due to its versatile analytical capabilities.[127–129] For example, Ye *et al.*[130] applied TDA to determine the hydrodynamic radii and diffusion coefficients of four pharmaceutical compounds in viscous solvent systems including acetonitrile, propylene glycol, isopropyl myristate, and medium-chain triglycerides. In another study, Lewandrowska and colleagues[131] introduced an empirical equation aimed at significantly reducing the analysis time required for measuring diffusion coefficients of analytes such as salts, drugs, amino acids, and proteins. Their work demonstrated that the use of spiral-shaped capillaries at high flow rates could reduce analysis time to just a few minutes,

in contrast to the nearly hour-long durations required for traditional TDA performed in straight capillaries with lower flow rates. In certain contexts, TDA is also referred to as Taylor–Aris dispersion analysis. During its early application phases, the method was mainly used to determine gas diffusion coefficients,[132] and subsequently for liquids,[133] often utilizing wide-bore tubing. However, with the integration of fused silica capillaries, the TDA technique experienced renewed attention due to its ability to perform measurements with sub-nanoliter sample volumes—an advantage that significantly reduces sample consumption. Under these improved conditions, TDA has enabled researchers to determine diffusion coefficients and hydrodynamic radii for solutes spanning a wide size range, from angstrom-scale molecules to submicron particles and molecular complexes.[72]

A broad spectrum of chemical and biological analytes has been successfully evaluated using TDA, including small molecules,[134] macromolecules,[135] synthetic and natural polymers,[136,137] ions, colloidal particles,[138] amino acids, peptides,[139] liposomes,[140] nanoparticles,[141–143] pharmaceutical compounds,[130] therapeutic proteins,[144] and dendrimers. The technique's utility extends beyond mere measurement, serving also in biophysical and biochemical analyses, such as drug delivery system design,[145,146] mixture analysis,[147] and biosensing applications. Among these, the accurate determination of hydrodynamic radius in pharmaceutical and bioactive solutes is particularly critical. Because such analytes often originate from biological sources and are present at extremely low concentrations, analytical techniques with high sensitivity and precision—such as TDA—are essential for their detection and quantification.

With the growing global interest in nanomaterials and nanotechnology, TDA has been increasingly recognized as a valuable tool for nanoparticle characterization. Numerous studies have benchmarked TDA against other conventional particle sizing and characterization techniques, revealing its superior performance in many cases. Techniques such as dynamic light scattering (DLS), field-flow fractionation (FFF), size exclusion chromatography (SEC), pinched flow fractionation (PFF), transmission electron microscopy (TEM), scanning electron microscopy (SEM), atomic force microscopy (AFM), nuclear magnetic resonance (NMR), fluorescence correlation spectroscopy (FCS), ultraviolet-visible (UV-vis) spectroscopy, nanoparticle tracking analysis (NTA), analytical ultracentrifugation (AUC), and flow-based techniques like TDA itself are frequently used for particle size determination.[148–152] However, each of these methods comes with its own set of advantages and limitations.

Table 1 provides a comparative overview of the advantages and drawbacks of several such methods, with particular emphasis on TDA. As is evident, TDA presents fewer limitations

Table 1 Advantages and disadvantages of different particle size determination methods

Measurement	Advantages	Disadvantages	Ref.
DLS	■ Rapid analysis capability for simple samples ■ Used for biological complex samples, such as blood plasma with minimal preparation required ■ Determination of hydrodynamic diameter and assessment of colloidal stability	■ High sensitivity to analytes aggregation ■ Limited accuracy in characterizing small particles in the presence of larger ones in complex samples	153, 154
SEC	■ Efficient particle separation based on size ■ Suitable for analyzing nanoparticles, proteins and polymers	■ Requires precise calibration ■ Demands large sample volumes, laborious sample preparation & lengthy analysis time ■ Undesired interactions between sample and experimental media (for example: analyte with chromatography column)	155, 156
TEM	■ Providing precise insights into particle size and core structure with direct nanometer-resolution imaging	■Advanced and very expensive instrumentation ■ Requires a vacuum environment ■ Inability to measure the hydrodynamic diameter of particles	157, 158
NTA	■ Measurement of heterogeneous particle size distribution ■ Determination of hydrodynamic diameter and assessment of colloidal stability	■ Advanced and very expensive instrumentation	159
TDA	■ No prior knowledge of sample concentration details or precise calibration require ■ Minimal sample volume consumption (nanoliter range) ■ Brief analysis time ■ Not being limited the technique for a particular shape of nanoparticle ■ Applicable across a wide range of particle sizes from angstrom to sub-micron scale ■ Simple sample preparation and direct analysis without requiring filtration, dilution, or centrifugation ■ Not as reliant on sample polydispersity in comparison to DLS	■ Limited to precisely separating particles with similar properties, such as particles with closely matched sizes, and in measuring very large or very small particles ■ Sensitivity to flow conditions like fluid viscosity	160–162

Table 2 General, simplified, and modified equations in TDA for determining the molecular diffusion coefficient

Equation/calculated parameter	Relation	Description	Ref.
Stokes–Einstein/hydrodynamic radius (R_h)	$R_h = \frac{k_B T}{6\pi\eta D_m}$	k_B: Boltzmann constant [J/K] T: Absolute temperature [K] η: Dynamic viscosity of solution [Pa s] D_m: Molecular diffusion coefficient [m^2 s^{-1}] ✓ Inverse relationship between the molecular diffusion coefficient and hydrodynamic radius of particles	129
Taylor–Aris (general mode)/molecular diffusion coefficient (D_m)	$D_m = \frac{l_D}{4t_R}\left(\frac{l_D\sigma^2}{{t_R}^2} - \sqrt{\frac{{l_D}^2\sigma^4}{{t_R}^4} - \frac{R^2}{3}}\right)$	l_D: Length of the channel or tube to reach solute to detector [m] t_R: Average residence time [s] σ^2: The degree of analyte band broadening in TDA (analyte peak variance) [m^2 or s^2] R: Channel or capillary tube radius [μm] ✓ Average residence time ≫ characteristic diffusion time across a specified distance and equivalent to the capillary tube's or microchannel's radius (R) ✓ $t_R \gg \frac{2R^2}{3.8^2 D_m}$, $\tau = \frac{D_m t_R}{R^2} \Leftrightarrow \tau \gg 0.14$, for ratio of 1 : 10 ⇒ $\tau \gg$ 1.4	127
Taylor–Aris (general mode for chromatographic parameters)/ molecular diffusion coefficient (D_m)	$D_m = \frac{U}{4}\left(H - \sqrt{H^2 - \frac{R^2}{3}}\right)$,	h: Theoretical plate height [m] U: Linear average fluid velocity [m s^{-1}] τ: Dimensionless residence time [–] ✓ $t_R \gg \frac{2R^2}{3.8^2 D_m}$, $\tau = \frac{D_m t_R}{R^2} \Leftrightarrow \tau \gg 0.14$, for ratio of 1 : 10 ⇒ $\tau \gg$ 1.4	127
Taylor–Aris (simplified mode)/molecular diffusion coefficient (D_m)	$D_m = \frac{R^2 t_R}{24\sigma^2}$	ε_{RE}: Relative error during determination of D [–] ✓ Usable for single – point detection window ✓ Usable for axial diffusion negligible compare to convection mechanism (TDA measurements that only include radial diffusion consideration) ✓ $D_m \ll \frac{R^2 u^2}{48D} \Rightarrow Pe \gg 6.9$, for ratio of 1 : 10 ⇒ Pe ≫ 69 & $\tau \gg$ 2.5 (ε_{RE} = 1%) ✓ For ratio of 1 : 10 ⇒ Pe ≥ 40 & $t_R \gg \frac{3R^2}{80 D_m \varepsilon_{RE}} \Rightarrow \tau \gg 1.25$ (ε_{RE} = 3%)	163
Taylor–Aris (modified form)/molecular diffusion coefficient (D_m)	$D_m = \frac{R^2(t_2 - t_1)}{24({\sigma_2}^2 - {\sigma_1}^2)}$	✓ t_1, t_2: Times required for the analyte band to reach both detectors or sensors ✓ ${\sigma_1}^2$, ${\sigma_2}^2$: Temporal fluctuations of the concentration profile at detector 1 & 2 ✓ Usable for dual – point detection window	164, 165

and greater flexibility, especially in systems involving low analyte concentrations, delicate biological samples, or non-invasive requirements. Moreover, the analytical robustness of TDA addresses many of the deficiencies and challenges associated with traditional techniques, positioning it not only as an alternative but increasingly as a primary method for nanoparticle and solute characterization across various disciplines. Consequently, TDA is now being employed more extensively than many conventional approaches and continues to demonstrate expanding utility in both fundamental research and applied technologies.

In accordance with Table 2 and the practical applications of TDA method, both the Stokes–Einstein relation and generalized or simplified forms of the Taylor–Aris equation are utilized for calculating the hydrodynamic radius of solutes and determining their molecular diffusion coefficients under various experimental conditions. These adaptations include chromatographic versions of the Taylor–Aris model and other corrected expressions tailored to specific analytical systems. Furthermore, Table 2 presents not only the equations themselves but also the definitions and descriptions of all relevant parameters, along with the validity criteria and inequality conditions necessary to ensure the accuracy of their application. The "1 : 10 ratio" noted in the last column refers to a situation in which the contribution of convective transport is ten times greater than that of molecular diffusion, a condition frequently assumed to validate the Taylor dispersion regime. The table also distinguishes between single-point and dual-point detection systems. A single-point detection window involves a solitary sensor along the capillary or channel, whereas a dual-point system utilizes two detection points. The latter provides higher precision, as it mitigates early-stage disturbances and injection instabilities that often affect single-point systems, such as sample fluctuations, pressure variations, or baseline drifts.

According to the mathematical relationships presented in Table 2, solute particles with lower molecular diffusion

Table 3 Summary of key terms, scaling relations, and regime-defining criteria in the context of TDA. Column 1 presents the primary terms of the advection–diffusion equation in axial and radial directions, along with their approximate dimensional analogues for physical insight. Column 2 outlines the characteristic time scales governing axial convection and radial diffusion processes. Column 3 classifies the principal transport regimes—such as pure convection or pure diffusion—and defines the corresponding validity conditions for TDA based on dimensionless inequalities and Péclet number thresholds[166]

Column 1		Column 2		Column 3		
Unsteady convective diffusion equation in two direction: $\frac{\partial C}{\partial t}+U(r)\frac{\partial C}{\partial x}=D\left(\frac{1}{r}\frac{\partial}{\partial r}\left(r\frac{\partial C}{\partial r}\right)\right)+D\left(\frac{\partial^2 C}{\partial x^2}\right)$, $U(r)=2U\left(1-\left(\frac{r}{R}\right)^2\right)$	Terms definition	Temporal scaling for effects of convection & diffusion in TDA	Diffusion/convection	Taylor Dispersion Analysis original conditions & limits	Different regions/limits	Governing inequality to satisfy regions
	$\frac{\partial C}{\partial t}\sim\frac{C}{t_R}$ Transient concentration		$\left(\frac{R^2}{D}\right)$ Radial molecular diffusion		Pure axial diffusion	✓ Diffusion rate ≫ convection rate (second condition for low Peclet number) ✓ $\frac{R^2}{D},\ \frac{L^2}{D}\ll\frac{L}{U},\ L\gg R,\ \frac{tD}{R^2}\gg 1$ ✓ $\mathrm{Pe}\ll\frac{L}{R},\ \mathrm{Pe}\ll\frac{R}{L}$
	$2U\left(1-\left(\frac{r}{R}\right)^2\right)\frac{\partial C}{\partial x}\sim\frac{UC}{L}$ Convection mechanism		$\left(\frac{L^2}{D}\right)$ Axial molecular diffusion		Axial diffusion + convection	✓ $\frac{1}{\gamma}\gg\mathrm{Pe}\gg\frac{R}{L}$
	$D\left(\frac{1}{r}\frac{\partial}{\partial r}\left(r\frac{\partial C}{\partial r}\right)\right)\sim\frac{DC}{R^2}$ Radial diffusion mechanism		$\left(\frac{L}{U}\right)$ Axial convection		Only Taylor–Aris dispersion	✓ $D_{\mathrm{eff}}=D(1+\gamma\mathrm{Pe}^2)$ ✓ $\frac{L}{R}\gg\mathrm{Pe}\gg\frac{R}{L}$
	$D\left(\frac{\partial^2 C}{\partial x^2}\right)\sim\frac{DC}{L^2}$ Axial diffusion mechanism		$\left(\frac{R}{U}\right)$ The time scale for movement across any radial distance due to diffusion, under the influence of axial convection at the mean flow velocity		Only Taylor dispersion condition (RD dominant over AD)	✓ Radial diffusion ≫ axial diffusion ✓ $\frac{DC}{R^2}\gg\frac{DC}{L^2}\rightarrow L\gg R$, $L=Ut$, $t\sim\frac{R^2}{D}$ ✓ 1, $\frac{1}{\gamma}\ll\mathrm{Pe}\ll\frac{L}{R}$
					Pure convection	✓ Convection rate ≫ diffusion rate (first condition for high peclet number) ✓ $\frac{L}{U}\ll\frac{R^2}{D},\ \frac{L^2}{D}L\gg R$, $\mathrm{Pe}\gg 1$ ✓ $\mathrm{Pe}\gg\frac{L}{R}$, for neglect radial diffusion ✓ $\mathrm{Pe}\gg\frac{R}{L}$, for neglect axial diffusion

coefficients tend to exhibit significantly greater hydrodynamic dispersion compared to those with higher diffusion coefficients. This behavior arises because low-diffusivity solutes lack the capacity for lateral movement across flow streamlines and thus remain confined to their initial velocity zones for extended periods. Consequently, they experience a broader range of local velocities, resulting in larger deviations from the mean flow speed and a more pronounced axial spreading of the solute band. In contrast, particles with higher diffusivity are capable of rapidly migrating between regions of different flow velocity, thereby averaging out these differences and concentrating their velocity distribution more tightly around the mean flow speed. In effect, high-diffusivity particles self-adjust to the mean flow velocity, whereas low-diffusivity species remain segregated within localized velocity gradients, amplifying dispersion.

This contrast in behavior is elegantly captured by eqn (3), which highlights the inverse relationship between the molecular diffusion coefficient and the Taylor dispersion coefficient. The greater the molecular diffusivity, the smaller the Taylor dispersion, and *vice versa*.

$$D = \frac{R^2 U^2}{48 D_{TH}} \tag{3}$$

Table 3 consists of three primary columns, each representing a specific conceptual and mathematical aspect of TDA methodology. The first column introduces the terms from the advection–diffusion (or continuity) equation, separately addressing the axial and radial directions. To enhance comprehension of the mechanisms involved and to support the approximate analytical framework proposed by Taylor, each term is accompanied by a dimensionally equivalent expression that serves as a physical-scale surrogate. Since the full continuity equation, as shown in column 1, does not possess an exact analytical solution, Taylor[45] applied a methodology known as scaling analysis to derive an approximate yet insightful expression. This scaling analysis technique involves assigning characteristic scales to each physical variable in the governing equation to assess the relative importance of different terms under varying experimental or flow conditions. By identifying which terms dominate and which can be neglected within a given regime, this approach provides a rational basis for simplifying the governing equations without losing essential physical meaning. In essence, scaling analysis enables researchers to derive tractable models that accurately capture the leading-order behavior of solute dispersion in micro- and nano-scale systems.

The parameters introduced in Table 3 include the solute concentration C, molecular diffusion coefficient D, average linear flow velocity U, axial characteristic length L, capillary or channel radius R, residence time t_R or t, radial coordinate r, axial position x, Péclet number Pe, and a geometric-flow-dependent parameter γ. The local flow velocity $U(r)$, which varies with radial position, is a critical term in the dispersion process, especially in systems exhibiting parabolic or otherwise non-uniform flow profiles. Notably, the parameters L and R represent the spatial domains over which axial and radial concentration gradients, respectively, are observed and are fundamental in defining the relevant time scales for solute dispersion. Column 2 of Table 3 lists the characteristic time scales corresponding to advection and diffusion in both axial and radial directions. Understanding these time scales is crucial for accurate modeling of the TDA process, as they determine the temporal evolution of solute spreading. For instance, the time required for radial diffusion to homogenize concentration variations across the channel cross-section often dictates the validity of Taylor's dispersion model.

The final column provides the principal regimes of the TDA framework, delineated by specific Péclet number ranges and associated inequality conditions derived from the previously defined time scales. For example, in the pure convection regime, which arises at very high Péclet numbers, axial solute transport is dominated by advection, and axial diffusion can be neglected. This regime represents the first essential condition for Taylor's analytical derivation. Conversely, at very low Péclet numbers, the system enters a diffusion-dominated regime where axial diffusion is non-negligible, and radial concentration gradients are rapidly smoothed out due to sufficient residence time. This "pure axial diffusion" condition defines the second foundational criterion for the validity of the Taylor dispersion approximation.

Ultimately, Table 3 integrates these conceptual elements to outline the full scope of operational regimes in Taylor dispersion analysis, highlighting the balance between advection and diffusion in determining solute transport behavior. The framework provided here aids in selecting the appropriate regime for modeling, interpreting experimental results, and designing accurate, robust microfluidic and capillary-based separation systems.

2.5. Governing equations and influential parameters

In microfluidic systems, where understanding mass transfer mechanisms is critical for the design and optimization of analytical and separation processes, a comprehensive set of governing equations is essential for accurate modeling and prediction of solute transport behaviors. To numerically or analytically model hydrodynamic dispersion of different solutes under various flow and boundary conditions, typically four fundamental classes of equations are employed. These include the Navier–Stokes and continuity equations for describing the velocity field of the fluid, Laplace or Poisson equations for determining the electrostatic potential distribution, and the advection–diffusion equation for capturing the cross-sectional average concentration profiles of the analyte species. Depending on the nature of the problem—whether steady-state or transient—these equations may be solved accordingly to yield time-dependent or time-invariant insights into the dispersion behavior. The coupled solution of these equations, incorporating appropriate initial and boundary conditions

based on system geometry and external driving forces (*e.g.*, pressure-driven flow, electroosmotic flow, *etc.*), enables a detailed quantitative analysis of Taylor dispersion across different microfluidic scenarios. This modeling framework is essential for uncovering the interplay between flow field non-uniformities, solute diffusion, and electrokinetic effects, particularly in complex configurations such as channels with charged or soft walls, patterned zeta potentials, or externally applied electric fields.[167,168]

$$\nabla^2\phi = -\frac{\rho_e}{\varepsilon} \tag{4}$$

$$\begin{cases} \nabla\cdot j = Q_{j,v} \\ j = \sigma E + j_e \\ E = -\nabla\phi \\ \nabla^2\phi = 0 \end{cases} \tag{5}$$

$$\nabla\boldsymbol{u} = 0 \tag{6}$$

$$-\nabla p + \eta\nabla^2\boldsymbol{u} = 0 \tag{7}$$

$$\frac{\partial c}{\partial t} + \nabla\cdot(-D\nabla c + \boldsymbol{u}c) = 0 \tag{8}$$

The parameters influencing the control, intensity, and mechanistic understanding of hydrodynamic dispersion in microfluidic systems are highly system-dependent, necessitating a case-by-case approach tailored to the specific features of each microenvironment. For accurate experimental characterization, theoretical investigation, and numerical modeling of transport processes—including Taylor dispersion—it is essential to identify and isolate the dominant factors for the system under consideration. Drawing from extensive prior research in the literature, it becomes evident that these parameters must be selected carefully and customized for each system architecture. In general, for any given microfluidic platform, several universal yet critical parameters govern the dispersion behavior. These include the cross-sectional geometry of the channel (*e.g.*, straight, curved, converging–diverging), the nature of the working fluid (Newtonian or non-Newtonian), and the type of driving force applied to induce flow. The latter encompasses pressure gradients (pressure-driven flow), steady and oscillatory electric fields (electroosmotic and AC electroosmotic flows), as well as external magnetic fields in magnetohydrodynamic systems. Each of these factors plays a decisive role in determining the velocity field, the solute distribution, and ultimately, the extent and characteristics of hydrodynamic dispersion.

3. Principal strategies for controlling hydrodynamic dispersion

In microfluidic technologies—particularly in LOC platforms where precise control over transport, mixing, and separation of analytes is of paramount importance—regulating hydrodynamic dispersion, or Taylor dispersion, of solute species is an inevitable requirement. Effective control over dispersion is critical for ensuring reliable analytical outcomes, reproducible diagnostics, and efficient micro-scale processing. Consequently, a thorough understanding of the core methods used to minimize or regulate hydrodynamic dispersion in microfluidic environments is essential. Among the most prominent and foundational approaches are geometrical modifications of the micro- or nanochannel cross-section, optimization of aspect ratios, and structural reconfiguration to influence flow behavior. Surface engineering techniques such as the application of chemical reactions of varying orders, solute adsorption at channel walls, imposition of asymmetric slip lengths, and manipulation of wall zeta potential heterogeneities also play vital roles. Furthermore, tuning surface roughness or choosing appropriate working fluids—Newtonian or non-Newtonian—based on their rheological properties, represent core methodologies for influencing the dispersion characteristics. This section synthesizes findings from a wide range of studies, offering a comprehensive overview of key dispersion control strategies. Through critical comparison of these methods, the effectiveness and limitations of each technique are highlighted in the context of diverse microfluidic configurations. The overarching objective is to identify persistent challenges in the current literature, uncover overlooked opportunities for innovation, and establish a foundational understanding that will enable targeted improvement in microfluidic separation techniques. A deep and integrated grasp of the physical principles underpinning hydrodynamic dispersion not only enables precise modulation of the phenomenon but also significantly enhances the performance and resolution of microscale systems in both analytical and functional applications.

3.1. Channel cross-sectional geometry

Modifying the cross-sectional geometry of microfluidic platforms—such as micro/nanochannels or microchips—has emerged as one of the most fundamental strategies for controlling hydrodynamic (Taylor) dispersion, particularly due to its significant influence on flow behavior and solute transport. The primary aim in this context is to identify sources of dispersion intrinsic to various geometrical configurations (*e.g.*, velocity retardation near channel walls due to no-slip conditions) and to optimize channel design through geometric tuning, as extensively explored in past studies, with the overarching goal of effectively mitigating hydrodynamic dispersion. Dutta *et al.*[94] conducted a combined analytical and numerical study to investigate the influence of aspect ratio and different channel cross-sections—including rectangular, isotropically etched, elliptical, trapezoidal, and parallel-plate channels—on Taylor–Aris dispersion of solutes under pressure-driven flow. Although pressure-driven flow often introduces higher dispersion due to shear stress effects, it remains a practical choice in many

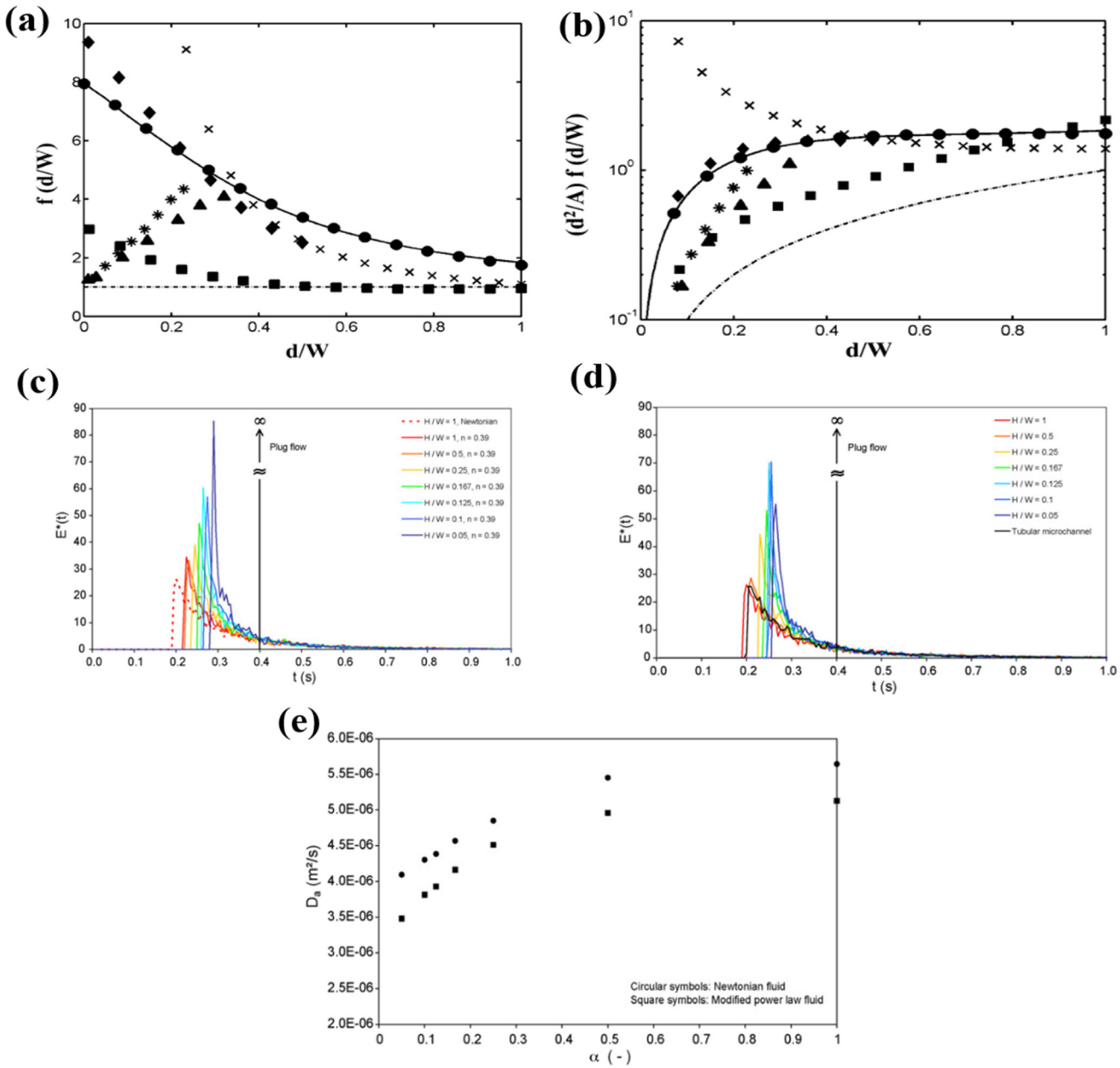

Fig. 6 Influence of channel aspect ratio (AR) on the geometric factor (f) of Taylor–Aris dispersion, residence time distribution (E(t)), and axial dispersion coefficient (D_a). (a and b) Effect of AR on dispersion under pressure-driven flow for fixed depth and fixed cross-sectional area, respectively, across various geometries including rectangular, isotropically etched, parallel-plate, elliptical, and optimally curved channels. Adapted from ref. 94 with permission from Springer-Verlag, copyright 2006. Variations in residence time distribution and axial dispersion for (c) Newtonian and (d) shear-thinning non-Newtonian fluids, and (e) corresponding axial dispersion coefficients, under different aspect ratios in microchannels. Adapted from ref. 173 with permission from Elsevier B.V., copyright 2008.

electrokinetic systems where electroosmotic flow is limited by operational constraints. By introducing a geometric factor (F_g) as a function of channel aspect ratio (depth-to-width), they quantified the variation of dispersion with respect to aspect ratio under two scenarios: fixed channel depth and fixed cross-sectional area. Under constant depth, both the geometric factor and dispersion minimized at high aspect ratios (narrower channels). Conversely, at constant cross-sectional area, dispersion increased with higher aspect ratios and decreased with lower ones, indicating the importance of selecting appropriate geometry to minimize dispersion in practical microfluidic devices (Fig. 6a and b). Interestingly, elliptical channels exhibited the highest dispersion due to pronounced variations in streamline velocity, while wide rectangular or isotropically etched channels showed increased dispersion relative to parallel-plate geometries at low aspect ratios.

In addition to standard shapes, researchers numerically assessed the influence of alternative geometries such as pinched ducts, tapered ducts, and I- and T-shaped channels,

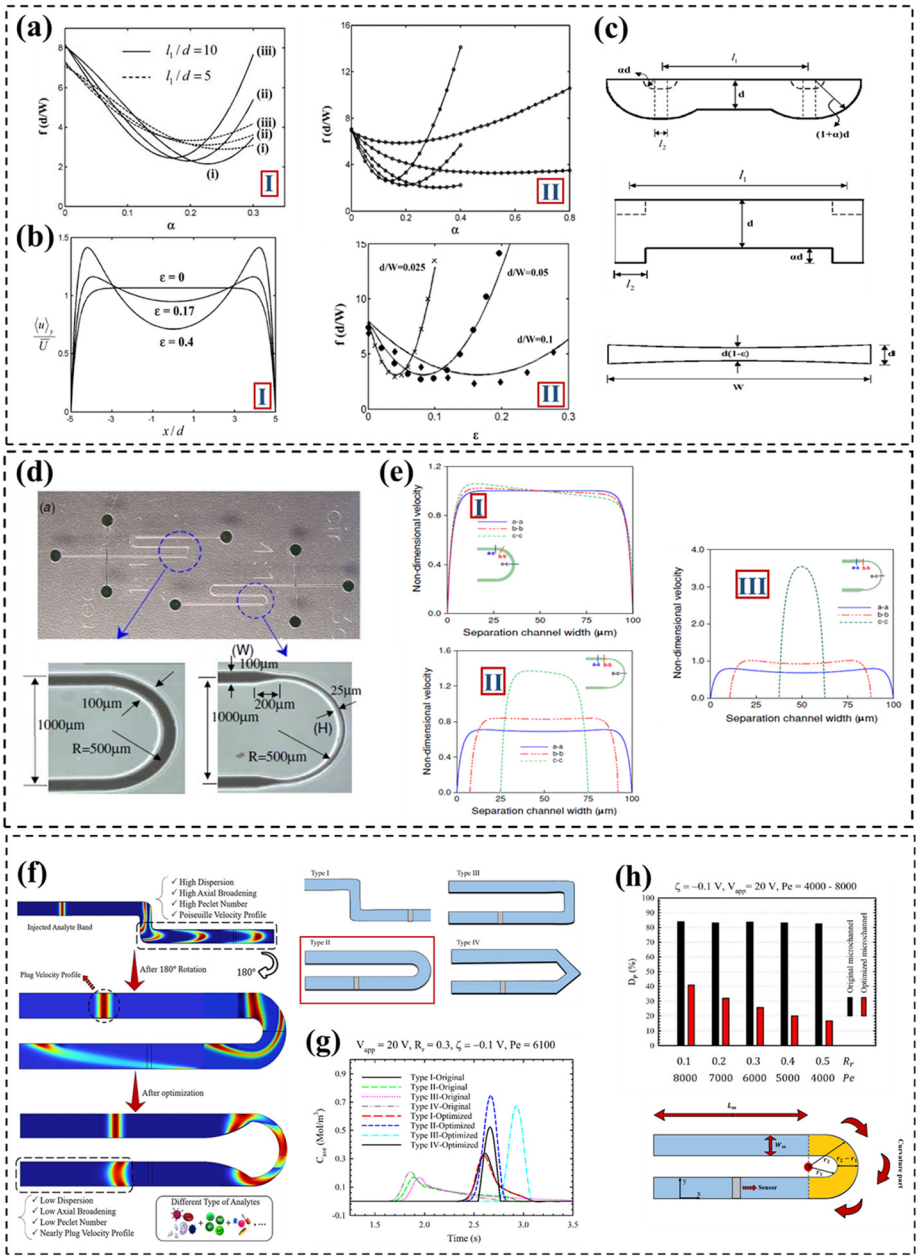

Fig. 7 (a) Impact of introducing additional depth in the lateral regions through secondary etching on the significant reduction of the hydrodynamic dispersion factor for solutes, aiming to identify the optimal value of the dimensionless parameter α in dual-etched (a-I) isotropic and (a-II) rectangular channels with high aspect ratios. In panel (a-I), the symbols i, ii, and iii represent different values of the ratio l_2/d = 0, 0.2, and 0.4, respectively, for the solid and dashed lines. (b) Effect of applying positive curvature degree values (ε or δ) to both the upper and lower channel walls in the inward bowing direction on: (b-I) the variation of mean velocity along the channel depth at a constant aspect ratio d/w = 0.1, and (b-II) the reduction of dispersion coefficient across different aspect ratios. (c) Schematic overview of the dual-etching process applied to the lateral regions of isotropic and rectangular channels with an etching depth of αd, and representation of a curved (inward-bowed) channel. The total width of the isotropic channel after secondary etching is defined as $w = l_1 + l_2 + 2(1 + \alpha)d$. The term $d(1 - \varepsilon)$ denotes the amount of wall curvature toward the channel interior or exterior, which alters the depth at the center and sidewalls depending on the curvature parameter. Adapted from ref. 94 with permission from Springer-Verlag, copyright 2006. (d) Schematic of serpentine U-shaped separation microchannels with varying curvature ratios. (e) Velocity profile plots across the microchannel width for three sections—two before the solute band enters the curved region and one at the midpoint of the curve—for curvature ratios (e-I) 1, (e-II) 2, and (e-III) 4. Adapted from ref. 174 with permission from IOP Publishing Ltd, copyright 2004. (f) Schematic illustrating improved control of analyte band dispersion in the optimized second U-shaped geometry compared to the first S-shaped configuration, along with an overview of the four considered geometries. In the three U-shaped designs, decreasing the shape factor from 1 to 0 progressively transitions the curved section from wide to tapered. (g) Temporal variation of the analyte band's mean concentration profile for each of the four geometries before and after optimization. (h) Geometric characteristics and schematic diagram showing the influence of the radius ratio and Péclet number on the analyte band dispersion percentage in the optimized second U-shaped geometry, before and after optimization, under conditions of ζ = −0.1 V and V_{app} = 20 V. Here, V_{app} and ζ represent the applied system voltage and the wall zeta potential, respectively. The width and length of the rectangular section (preceding the curved region) are denoted by W_m and L_m, set to 100 μm and 1000 μm, respectively. Adapted from ref. 167 with permission from Elsevier B.V., copyright 2025.

which mimic near-rectangular configurations, to further mitigate Taylor–Aris dispersion.[169] Ajdari *et al.*[170] and Vikhansky[171] provided theoretical insights using lubrication approximation, predicting that in shallow microchannels with pseudo-rectangular cross-sections—such as triangular, parabolic, or elliptical profiles—dispersion is primarily governed by channel width rather than depth. They derived analytical expressions for effective dispersion (D_{eff}) in the long-time limit (Taylor regime), where axial solute concentration approaches a Gaussian distribution and the dispersion coefficient becomes dominant in describing transport behavior. These theoretical predictions were later validated experimentally by Bontoux *et al.*,[172] who studied hydrodynamic dispersion in shallow parabolic microchannels and confirmed the accuracy of the models proposed.

Further exploring this relationship, Aubin and colleagues[173] employed computational fluid dynamics (CFD) to analyze the effects of channel aspect ratio (AR = H/w) on axial dispersion and residence time distribution (RTD) in both Newtonian and shear-thinning non-Newtonian fluids. Their findings (Fig. 6c–e) demonstrated that rectangular channels with small aspect ratios—particularly below AR = 0.3—exhibited significantly narrower and more uniform RTD curves (Fig. 6c and d), as well as reduced axial dispersion (Fig. 6e), even under constant cross-sectional area. This behavior stems from the transition of velocity profiles toward plug-like flow as channel width increases and height decreases, leading to reduced velocity gradients and a more homogeneous transport field. Such geometric configurations, which promote plug-flow behavior and minimize axial dispersion, offer substantial benefits for a wide range of microfluidic systems—including microreactors, separation platforms, drug delivery devices, biosensors, LOCs, and chromatographic columns—where control over dispersion is critical for enhancing resolution, efficiency, and analytical accuracy under laminar flow conditions.[173]

Moreover, the analysis conducted by Dutta *et al.*[94] revealed that the slow movement of solute species in the lateral regions of the specified cross-sectional geometries—especially in channels with high aspect ratios—significantly contributes to the broadening of the solute band. To minimize and optimize the cross-sectional profile and address the issue of flow deceleration near the channel sidewalls, they suggested that appropriate surface modification techniques could substantially improve this problem by altering the pressure-driven flow pattern. Accordingly, they applied a secondary etching technique to increase the depth of the lateral regions in rectangular and isotropically etched channels, thereby accelerating fluid flow in those regions and ultimately reducing overall hydrodynamic dispersion by optimizing these channels (Fig. 7a-I, II and c). They further noted that smaller curvature degrees (ε)—referring to the extent of inward curvature of the upper and lower channel walls—lead to reduced disparities in velocity distribution and dispersion across the channel width compared to those with larger curvature degrees. When the curvature degree assumes a small positive value, the curvature behaves analogously to an increased channel depth near the sidewalls. In other words, under this condition, the fluid near the sidewalls moves at a speed similar to that in the channel center, which reduces both the velocity gradient and dispersion coefficient across the channel depth. Conversely, as the curvature degree increases beyond a certain threshold (*i.e.*, larger positive values), the disparity and heterogeneity in the mean velocity between the sidewalls and the channel center rise significantly, resulting in increased dispersion (Fig. 7b-II). According to Fig. 7b-I, especially for larger curvature values, two prominent peaks correspond to maximum mean velocity near the sidewalls (due to increased depth), and one trough indicates the minimum velocity at the channel center (due to reduced depth). Hence, as observed, for smaller curvature values, the absence of these peaks and reduced velocity fluctuations along the channel depth help suppress dispersion. Ultimately, a relationship was derived between the curvature degree and the geometric factor, determining the optimal value that minimizes dispersion. Fig. 7c displays the isotropically and rectangularly double-etched channels after side region optimization, aimed at equalizing the mean flow velocity between the lateral and central regions, as well as the curved channels.

Tsai *et al.*,[174] through numerical simulations, investigated the flow velocity profile and control of sample band dispersion of a fluorescent dye with a concentration of 10^{-4} M in a 1 mM $Na_2B_4O_7{\cdot}10H_2O$ buffer solution at pH = 9.2, under electroosmotic flow through a serpentine U-shaped microchannel fabricated on glass with a total length of 3 cm. They evaluated different curvature ratios at the turning regions of the U-shaped microchannel (Fig. 7d). As illustrated in Fig. 7d, the geometric curvature ratio was defined as the width of the channel prior to the bend (100 μm) divided by the channel width at the compact turning region, which varied between 100, 50, and 25 μm. This resulted in curvature ratios of 1 (100/100 μm), 2 (100/50 μm), and 4 (100/25 μm), respectively. Numerical simulations demonstrated that a curvature ratio of 4 yielded the highest uniformity and improvement in the flow velocity profile and the most effective control of sample band dispersion—particularly reducing the so-called racetrack effect—compared to the other two configurations (Fig. 7e). They then validated these findings experimentally by assessing the electrophoretic separation efficiency of a DNA sample in serpentine U-shaped separation microchannels. Additionally, they showed that by designing a multi-turn serpentine U-shaped channel of only 7 cm in length embedded within a chip-scale area, one can achieve a 99% separation efficiency equivalent to that of a straight channel of the same length.[174]

In a recent and highly innovative study in 2025, Aslani *et al.*[167] conducted a numerical optimization of four different curved microchannel geometries with fixed negative surface charge, including one S-shaped and three U-shaped configurations, before and after optimization. Using the finite element method implemented in COMSOL Multiphysics, they

evaluated the transport of a neutral analyte band containing dissolved molecules with initial concentration c_0 through an aqueous electrolyte under a direct current electroosmotic flow (Fig. 7f). The three U-shaped geometries differed by a shape factor parameter (n) ranging from 0 to 1, with values of n = 0.5, n = 1, and n = 0.01 assigned to the second, third, and fourth U-shaped geometries, respectively. The objective function of the optimization was defined such that the time discrepancy between the analyte band's passage through the inner and outer curvatures of the microchannels would be minimized. This would ensure velocity profile uniformity in these curved sections and balance the electric field strength across both inner and outer bends (*i.e.*, convergence of equipotential lines), thereby significantly controlling hydrodynamic dispersion in the optimized state relative to the unoptimized state.

Furthermore, by incorporating a detection sensor to measure the cross-sectional mean concentration of the analyte band (*i.e.*, how much of the solute had dispersed before reaching the sensor), they achieved dispersion control of 60%, 48%, and 32% for the three optimized U-shaped microchannels compared to their original states. Among them, the second U-shaped configuration was identified as the optimal geometry yielding the least dispersion (Fig. 7g). According to Fig. 7g, the S-shaped geometry (type 1) performed poorly in both its original and optimized forms, with approximately 70% longitudinal stretching and broadening of the analyte band in both cases. They also discovered that by increasing the geometric parameter $R_r = \frac{r_1}{r_2}$ (the ratio of inner to outer curvature radius in the U-shaped section) from 0.1 to 0.5 and reducing Pe, the analyte band dispersion decreased from 42% to 15% in the optimized case, whereas it remained nearly constant in the unoptimized case (Fig. 7h). In other words, as shown in Fig. 7h, larger values of R_r yielded significantly better optimization performance. During simulation, the outer curvature radius was fixed at 150 μm, while the inner radius varied from 15 to 75 μm to produce R_r values between 0.1

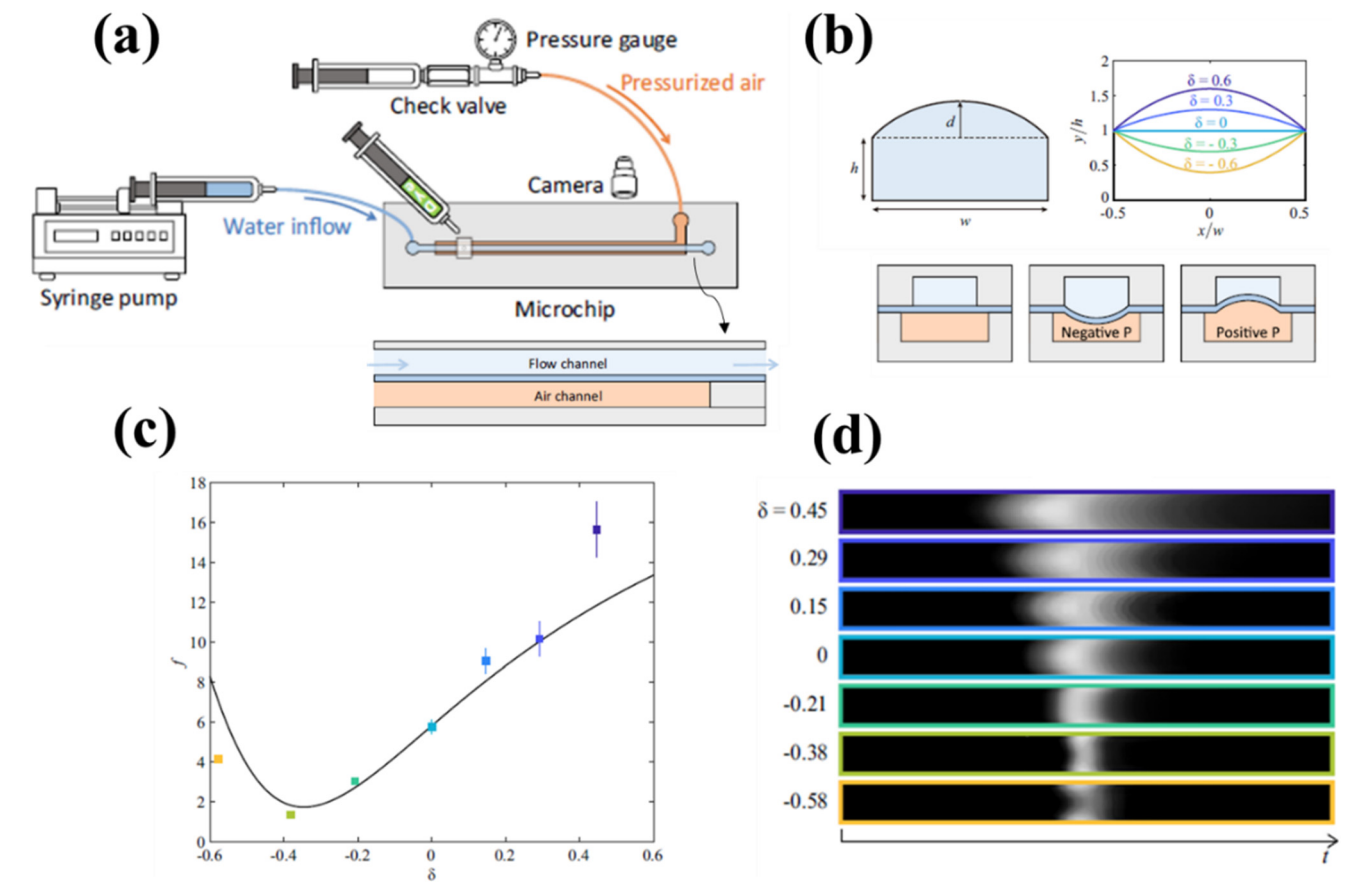

Fig. 8 (a) Schematic of the experimental setup used by Lee *et al.* for dispersion analysis. The air channel pressure was regulated using a pressure gauge, while deformation of the top microchannel wall was controlled by an external pressure source, allowing adjustment of the deflection parameter. Fluid was introduced into the microchannel *via* a syringe pump, and a high-resolution camera was employed to capture the temporal evolution of tracer dispersion. (b) Geometric schematic of the channel cross-section, where h, w, and d denote the original channel height (without wall deflection), width, and maximum wall deformation, respectively. The dimensionless deflection parameter, $\delta = d/h$, was used to represent undeformed ($\delta = 0$), outward ($\delta > 0$), and inward ($\delta < 0$) deformation of the top wall. (c and d) Variation of the dispersion factor as a function of the deflection parameter for a fixed aspect ratio of AR = h/w = 4.8, showing that the undeformed channel ($\delta = 0$) yields a baseline dispersion level. Greater dispersion, particularly under outward deformation (positive δ), is demonstrated through time-resolved dispersion intensity profiles. Adapted from ref. 175 with permission from Springer-Verlag, copyright 2021.

and 0.5. The observed 27% reduction in dispersion for R_r = 0.5 was attributed first to the broader boundary over which velocity was distributed (resulting in a more uniform velocity profile), and second, to the critical role of secondary flows in enhancing mixing and transverse mass transport, which effectively suppresses axial dispersion.[167]

In line with exploring the impact of geometrical deformation or wall curvature on microchannel performance, a straightforward and cost-effective strategy was developed by Lee *et al.*[175] in 2021 to control and manipulate hydrodynamic dispersion in a rectangular microchannel under fully developed pressure-driven flow, where only the top wall was deformed, using three different aspect ratios. In this study (Fig. 8a and b), a multilayer microfluidic chip was fabricated, and the deformation of its upper wall was modulated using a controlled pressure source (Fig. 8a). The authors found that the dispersion was strongly dependent on the wall deflection parameter relative to a standard, undeformed channel, as well as on the aspect ratio (Fig. 8b). For a given aspect ratio, they identified an optimal value of the deformation or deflection parameter, denoted as δ, which significantly minimized the dispersion coefficient or factor (Fig. 8c). As shown in Fig. 8c and d, an inward deflection value of approximately $\delta = -0.4$ at a fixed aspect ratio of AR = h/w = 4.8 was determined to be optimal, yielding the lowest dispersion distribution. Notably, the experimentally obtained data closely matched the numerically predicted values under this condition, where the numerical predictions were represented by solid black lines and the experimental results were shown as colored error bars.[175]

Practical considerations. While geometric optimization is conceptually straightforward, fabricating complex three-dimensional or curved microchannel structures often requires multi-step soft lithography or two-photon polymerization, which can be costly and time-consuming. Channel deformations during bonding or replication may also alter flow profiles, making the predicted dispersion control less precise in large-scale production.

3.2. Wall slip length

Another fundamental and influential approach to controlling hydrodynamic dispersion in microfluidic systems involves manipulating the slip length or slip boundary conditions at the channel walls. The extent of solute dispersion is significantly affected by this parameter. For instance, when slip conditions are applied to the walls of microfluidic structures such as microchannels or microlines, the fluid flow exhibits partial slip at the surface, particularly under minimal friction or adhesive interaction between fluid molecules and the channel surface. In such cases, the flow velocity at the wall becomes non-zero, contrasting with the classical no-slip condition. Wall slip is highly dependent on the physicochemical properties and surface features of the channel. Factors such as surface hydrophilicity or hydrophobicity, roughness or smoothness, surface coating with polymeric layers, the presence of micro- or nano-bubbles, and the type of fluid can all modulate slip behavior, leading to either enhancement or suppression of the slip velocity. Furthermore, wall slip directly alters the flow velocity profile. However, it does not necessarily reduce the velocity gradients across the channel cross-section and, therefore, does not always lead to a reduction in hydrodynamic dispersion. In other words, while slip boundary conditions certainly modify the flow profile, they do not always attenuate the lateral velocity differences across the channel. For example, when a fluid flows through a channel under pressure-driven conditions with constant slip length at the walls, the velocity profile may be uniformly shifted due to wall slip. Yet, the internal velocity gradient across the cross-section remains unchanged. Nevertheless, under asymmetric slip conditions (*i.e.*, unequal slip lengths on opposing walls), substantial alterations in transverse velocity gradients may occur.

In a seminal study, Ng (2011)[61] numerically and analytically investigated the influence of wall slip on Taylor–Aris dispersion in pressure-driven flows through parallel-plate and cylindrical channels. He derived expressions for the dispersion coefficient as a function of slip length for both geometries. To illustrate how slip length, in comparison to the no-slip condition, could serve as a critical control parameter for solute dispersion, he examined two flow scenarios separately: constant pressure gradient and constant flow rate, particularly in parallel-plate channels. His results indicated that when both walls possessed equal slip lengths ($\lambda_1 = \lambda_2 = \lambda$) or had only minor differences, the dispersion coefficient of the solute band was significantly reduced in both cases (Fig. 9a-I and II), and the velocity profile remained close to a plug-flow regime without transition to a parabolic (Poiseuille) profile.

Conversely, when a substantial difference existed between the slip lengths of the two channel walls, the dispersion coefficient increased drastically under both pressure-driven and fixed-flow-rate conditions, leading to heterogeneous dispersion of the solute band along the channel, governed by a non-uniform velocity profile. Ng concluded that large disparities in wall slip lengths (unequal slip) could override and even reverse the favorable effects of uniform slip conditions on reducing dispersion (Fig. 9b-I). Moreover, he observed that an increase in the dimensionless phase exchange parameter ($\hat{\alpha}$) could suppress the beneficial influence of wall slip by flattening the slope of the dispersion coefficient *versus* slip length (Fig. 9b-II). He further noted that mass or phase exchange between the fluid and the wall—such as in the case of porous or reactive boundaries—could have effects analogous to those of non-uniform slip lengths, typically resulting in increased dispersion.

In a follow-up study in 2012, Ng and Zhou[77] examined the combined effect of slight variations in surface zeta potential and non-uniform wall slip on solute dispersion in electroosmotic flow through microchannels with circular cross-sections. Their findings revealed that the interaction between spatially varying zeta potential and slip length

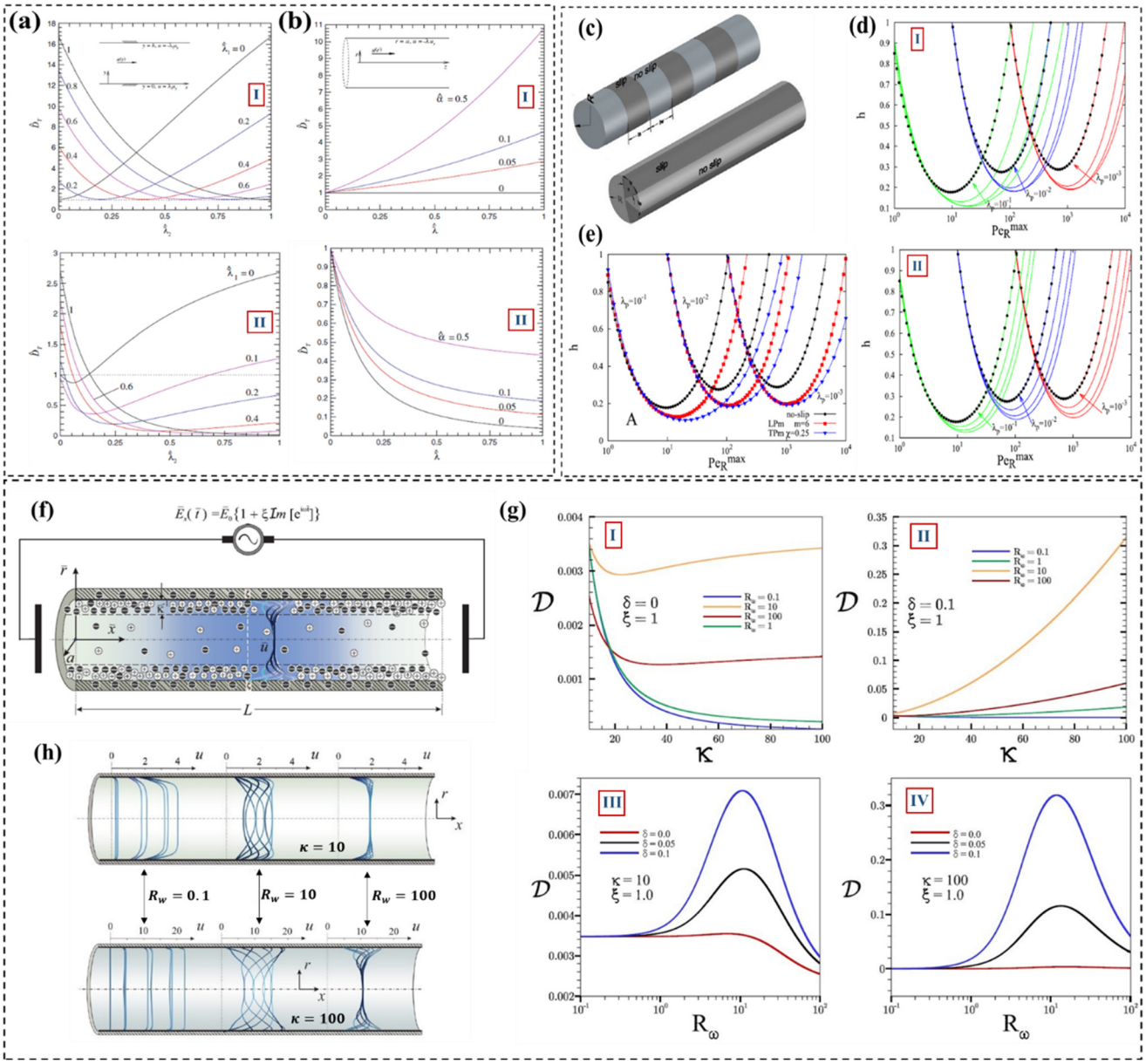

Fig. 9 (a) Normalized Taylor dispersion coefficient ($\hat{D}_T$) as a function of unequal wall slip lengths (λ_1, λ_2) for parallel-plate channels under (a-I) constant pressure gradient and (a-II) constant flow rate conditions. (b) $\hat{D}_T$ plotted *versus* a uniform slip length λ^ for various values of the dimensionless phase exchange parameter in circular microchannels under (b-I) pressure-driven flow and (b-II) constant flow rate. In all subplots, dashed lines represent the no-slip condition with $\hat{D}_T = 1$. Adapted from ref. 61 with permission from Springer-Verlag, copyright 2011. (c) Schematic of two alternating wall slip patterns: transversely patterned microtube (TPm, top) and longitudinally patterned microtube (LPm, bottom), showing periodic slip/no-slip stripes along the tube wall. (d) Effect of the geometric parameters χ and mm on the minimum height equivalent to a theoretical plate (HETP or *h*)—an indicator of separation efficiency—*versus* maximum radial Péclet number for particles with different radii λ_p: (d-I) TPm configuration, (d-II) LPm configuration. (e) Comparative performance of TPm and LPm designs with respect to minimum hh, alongside the reference case of a classical no-slip microcolumn (dashed black line), demonstrating improved particle separation and reduced axial dispersion. Adapted from ref. 101 with permission from AIP Publishing, copyright 2018. (f) Schematic of a microcapillary subject to electroosmotic flow under a time-varying (oscillatory) electric field *E*(t), examining the effect of slip length δ. (g) Impact of dimensionless Debye length (κ), slip length (δ), and angular Reynolds number (Rw) on the effective dispersion coefficient DeffDeff: (g-I, II) variation of *D* with κ for different Rw values in the absence (I) and presence (II) of slip; (g-III, IV) variation of *D* with Rw at κ = 10 (III) and κ = 100 (IV) for three slip lengths. (h) Non-dimensional velocity profiles over one oscillation period *t* = 0 to 2π for δ = 0.1, showing flow structure under different frequencies and Debye lengths. Adapted from ref. 176 with permission from APS Publishing, copyright 2018.

had a markedly different impact on dispersion compared to the uniformly distributed case. Notably, the presence of wall slip could enhance the dispersion that originated from non-uniform zeta potentials, especially under pressure-driven flow, leading to maximum dispersion levels in certain configurations.

Given the detrimental impact of axial dispersion—stemming from the combined effects of transverse diffusion and axial advection—on the separation efficiency of sample particles, Adrover *et al.*[101] conducted a theoretical and numerical study in 2018 using the generalization of Brenner's macrotransport framework. They examined hydrodynamic dispersion of finite-sized particles in hydrodynamic chromatography microcolumns (microtubes) by introducing two distinct types of periodically patterned structures on the inner surfaces of the columns (*i.e.*, generating surface heterogeneity). They found that applying alternating patterns of slip and no-slip regions along the wall—implemented as periodic stripes—enhanced transverse mixing and significantly attenuated axial dispersion. This, in turn, improved particle separation performance compared to conventional microcolumns with fully no-slip walls. Two distinct surface patterning configurations were proposed: transversely patterned microcolumns (TPm) and longitudinally patterned microcolumns (LPm), as depicted in Fig. 9c. For TPm, a key geometrical parameter $\chi = R/l_S$ was defined, where R is the column radius and l_S is the longitudinal length of a slip stripe. For LPm, the parameter m denoted the number of evenly spaced slip bands encircling the column wall. According to Fig. 9d-I, for TPm configurations, reducing the parameter χ (with values χ = 0.25, 0.5, and 1) led to stronger secondary flows due to elongated longitudinal slip stripes, ultimately decreasing the height equivalent to a theoretical plate (HETP, denoted as h), particularly for χ = 0.25. This corresponded to improved separation and better axial dispersion control across all particle sizes λ_p.

Similarly, as shown in Fig. 9d-II, for LPm configurations, reducing m (values considered were 6, 8, and 16) increased the width and surface coverage of slip regions around the column, which enhanced the wall slip effect. Consequently, both the dispersion coefficient and HETP decreased for all particle sizes, with the lowest dispersion achieved at m = 6. Based on a comparative analysis of Fig. 9d-I and II, TPm structures showed more consistent HETP values regardless of particle size, indicating higher robustness and performance stability. As a result, the authors concluded that TPm designs with low χ values outperform both LPm and conventional columns with fully no-slip walls (represented by dotted lines in Fig. 9e), offering superior control over axial dispersion and higher separation efficiency. In a separate analytical study in 2018, Muñoz *et al.*[176] employed a homogenization method with multiple scales to investigate the effect of hydrodynamic slip length in the presence of an oscillatory electroosmotic field (AC electroosmosis) on the effective Taylor dispersion of a neutral, passive analyte band in a microcapillary. The capillary was filled with a symmetric electrolyte solution and had a low constant zeta potential on the interior wall.

Four dimensionless parameters were analyzed: (i) the Debye length $\kappa^{-1} = \lambda_D$ (with values 10 and 100), (ii) the angular Reynolds number (0.1, 1, 10, and 100), (iii) the amplitude of the oscillatory electric field ξ (0, 0.5, 1), and (iv) the dimensionless Navier slip length $\delta = \lambda_N/a$ (with values 0 and 0.1). One of their key findings was that at moderate oscillation frequencies (Rw = 10) and for high Debye lengths (κ = 100), the presence of wall slip (δ = 0.1) led to a two-order-of-magnitude increase in effective dispersion compared to the no-slip case (δ = 0), as shown in Fig. 9g(I–IV).

In other words, under conditions δ = 0.1, Rw = 10, and κ = 100, the maximum dispersion and severe distortion of the velocity profile occurred due to the slip condition (Fig. 9h). However, for very low (Rw = 0.1) or very high (Rw = 100) frequencies, the velocity profile flattened (becoming more plug-like), resulting in minimal changes to the effective dispersion for both δ = 0 and δ = 0.1. Thus, by operating at very low or very high oscillation frequencies and increasing the Debye layer thickness, hydrodynamic dispersion under oscillatory electroosmotic flow can be substantially suppressed—even in the presence of slip.

In a more recent study, Ebrahimi *et al.*[177] derived an analytical expression for slip length as a function of the effective Taylor–Aris dispersion coefficient in carbon nanotubes (CNTs) containing Newtonian fluids. Their model was validated using molecular dynamics (MD) simulations. The results underscored the importance of understanding dispersion in nanoscale systems, where controlling mass transport and mixing is crucial. They concluded that for improved mixing, CNTs with low slip lengths are more favorable, while for minimized mixing or dispersion, high-slip CNTs are preferred under pressure-driven conditions. In summary, although modifying the wall slip length is not universally effective in reducing hydrodynamic dispersion—it may in some cases exacerbate it—it nonetheless remains a critical tool in dispersion control. Combining wall slip strategies with other system-specific factors and engineering complexities can significantly enhance dispersion regulation in microfluidic systems.

Practical considerations. Although wall slip can be exploited to tune axial dispersion, its experimental implementation remains challenging. Achieving reproducible slip lengths requires precise surface chemistry and low surface roughness, which may vary across fabrication batches. Furthermore, long-term stability of hydrophobic or lubricant-infused surfaces can deteriorate under continuous flow or biological media exposure, limiting the scalability of this approach for routine lab-on-a-chip applications.

3.3. Wall zeta potential

Another effective strategy for controlling hydrodynamic dispersion of solute species in microfluidic systems involves modifying surface properties—particularly the surface or zeta potential of channel walls. As previously discussed, more than half of microfluidic systems employ electroosmotic flow (EOF) as the primary driving mechanism for manipulating, controlling, and pumping fluid through the system. Consequently, the zeta potential plays a critical role in determining the EOF velocity profile. Upon applying an

external electric field, a slip velocity parallel to the cross-section of the system—such as a microchannel—develops at the boundary of the Debye layer. In cases where the Debye layer is thin, this slip velocity is typically applied as a boundary condition at the wall surface, and the Helmholtz–Smoluchowski velocity $u_{\text{EOF-HS}}$, given by eqn (9), is used to describe the EOF. When the zeta potential is constant and uniformly distributed along the channel walls (*i.e.*, surfaces with consistent positive or negative surface charge), the resulting electroosmotic velocity profile remains plug-like and stable. However, when the zeta potential distribution along the channel wall becomes non-uniform—either due to spatial variations in magnitude or by applying alternating patterns of positive and negative zeta potentials—the electroosmotic flow profile is distorted. This deviation disrupts the characteristic plug-like flow, induces local pressure gradients, and ultimately leads to increased hydrodynamic dispersion of the analyte band.[178]

$$u_{\text{EOF-HS}} = \frac{-\varepsilon\zeta}{\eta}E \tag{9}$$

Where, the parameters ζ, η, and E, represent zeta potential, fluid viscosity, and electrical field respectively.

Several surface heterogeneity factors can contribute to the non-uniformity of zeta potential, such as changes in the pH of the electrolyte solution, variations in ionic strength or electrolyte concentration, adsorption of solute molecules onto the channel wall, surface functionalization with different chemical groups, or polymeric surface coatings. Such zeta potential heterogeneity not only affects the EOF velocity profile and electric potential distribution but also significantly influences the effective dispersion coefficient—a key parameter for characterizing band broadening. Therefore, to prevent excessive hydrodynamic dispersion of solute species in microfluidic systems, maintaining a uniform zeta potential distribution is desirable—though not easily achievable in practice. Between approximately 2000 and 2009, extensive theoretical and numerical studies explored the effects of non-uniform zeta potential distributions—particularly stepwise distributions, where abrupt discrete jumps in zeta potential occur at specific channel locations—on EOF behavior and analyte band dispersion.[179–183]

In a parallel-plate microchannel with asymmetric wall zeta potentials (*i.e.*, $\zeta_1 \neq \zeta_2$), Medina *et al.*[184] developed an analytical model to investigate the conditions under which mass transfer and, consequently, species mixing can be enhanced. Their study focused on the hydrodynamic dispersion of neutral solutes under pulsatile electroosmotic flow (a combination of steady DC-EOF and oscillatory PEOF), generated by an externally applied sinusoidal electric field (Fig. 10a). To determine the electric potential distribution under asymmetric wall zeta potentials and within the electrical double layer, they employed the linearized Debye–Hückel approximation to solve the Poisson–Boltzmann equation. They then used the resulting distributions of electric field, flow velocity, and solute concentration to evaluate the effective dispersion coefficient under different flow conditions. Their analysis revealed that the resulting transport behavior strongly depends on several dimensionless parameters, including the non-uniform wall zeta potentials ($\tilde{\zeta}_{1,2}$), the oscillatory Reynolds number (Re_w), the Schmidt number ($\text{Sc} = \nu/D$), and the dimensionless Debye parameter ($\kappa H = H/\lambda D$). According to their results in Fig. 10b-I, when $\text{Re}_w = 1$ and the wall zeta potentials are symmetric ($\zeta_1 = \zeta_2 = 1$), the electroosmotic velocity profile remains uniform, flat, and plug-like over the oscillation cycle. However, increasing the oscillation frequency to $\text{Re}_w = 5$ and imposing strongly asymmetric wall potentials ($\zeta_1 = 1$, $\zeta_2 = -1$) led to significantly non-uniform and temporally varying velocity profiles (Fig. 10b-II).

In addition to the flow behavior, they also observed substantial changes in the cross-sectional concentration profiles and effective dispersion coefficient under conditions of zeta potential asymmetry and increased oscillation frequency. Specifically, both the solute concentration gradient (Fig. 10c-I and II) and the effective dispersion coefficient (Fig. 10c-III) exhibited strong oscillations and substantial increases under such conditions. Importantly, they demonstrated that while increased axial dispersion under uniform zeta potential generally improves longitudinal mixing, controlling Re_w at low values (*e.g.*, $\text{Re}_w = 0.1$ in Fig. 10c-I) can effectively suppress axial dispersion (lower D_{eff} as shown in Fig. 10c-III) and promote lateral mixing, even under strong zeta potential asymmetry. This enhanced transverse mixing—induced by the presence of cross-sectional flows under oscillatory fields—can be advantageous for homogenizing solute concentration distributions.

Conversely, at higher Re_w values (*e.g.*, 1 or 5), in the presence of asymmetric zeta potentials (*e.g.*, $\zeta_1 = 1,\ \zeta_2 = -\frac{3}{4}$), the increased non-uniformity of velocity and concentration profiles (Fig. 10b-II and c-II) led to a significant rise in axial dispersion (Fig. 10c-III). This, in turn, enhanced the mass transfer rate from high to low concentration zones and improved separation of species with distinct properties, such as differential migration velocities. In other words, larger particles with lower molecular diffusivity (*i.e.*, higher Schmidt number), which otherwise undergo slow mass transfer, experienced enhanced dispersion and separation when subjected to oscillatory flow fields and zeta potential heterogeneity (Fig. 10c-IV). In contrast to Medina *et al.*, Peralta *et al.*[185] examined the dispersion of a viscoelastic Maxwell fluid (non-Newtonian) with an elasticity number of 0.5 in a parallel-plate microchannel with spatially varying zeta potentials under oscillatory electroosmotic flow. Their findings showed that, unlike in Newtonian fluids, increasing the elasticity number and oscillatory Reynolds number significantly enhanced hydrodynamic dispersion. The velocity profiles exhibited stronger wave-like oscillations due to the combined effects of inertial, electric, elastic, and viscous forces.

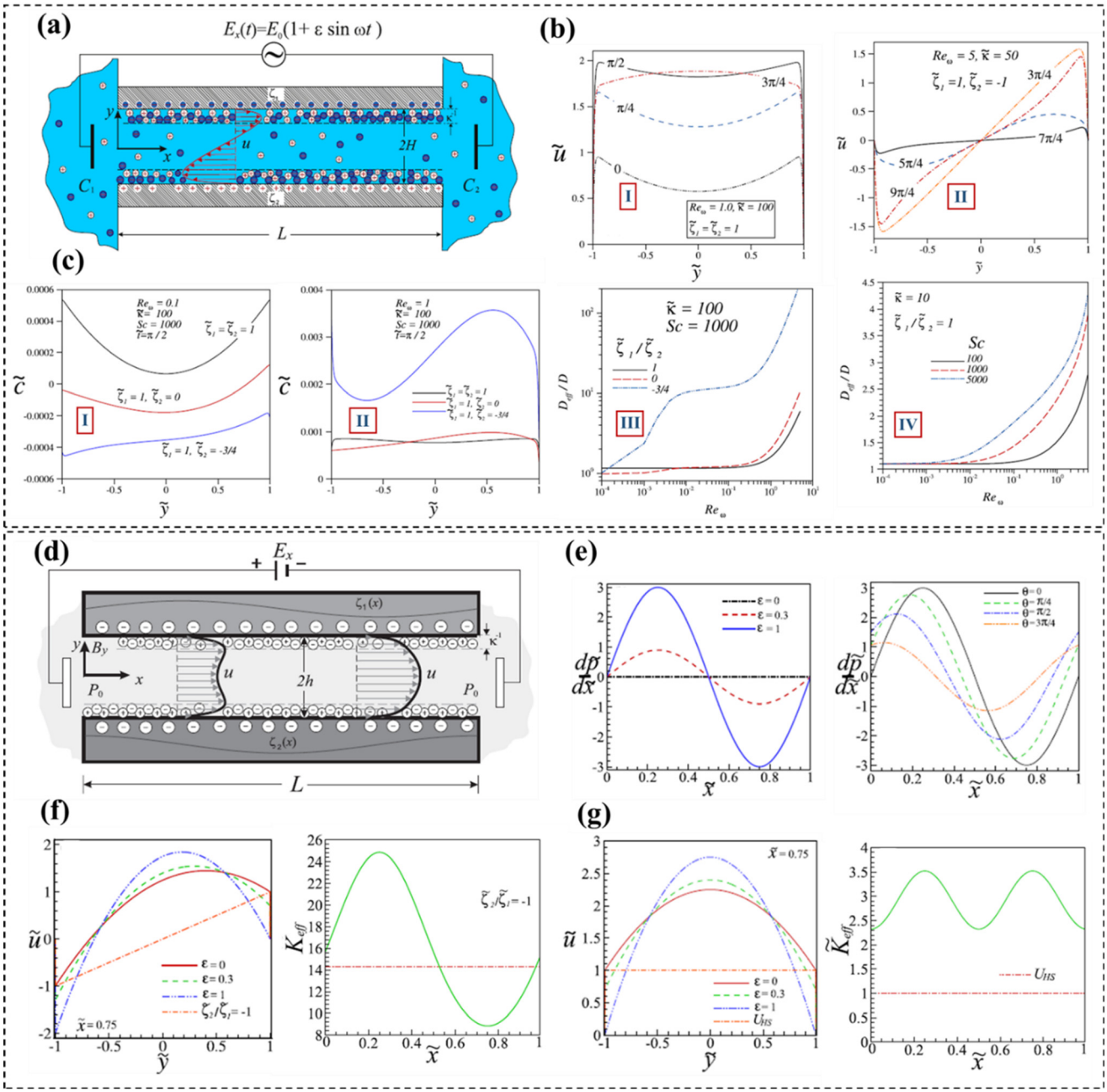

Fig. 10 (a) Schematic of neutral solute dispersion and mass transfer in a parallel-plate microchannel under asymmetric and non-uniform zeta potentials on the walls, driven by a time-varying sinusoidal external electric field inducing oscillatory electroosmotic flow and a constant concentration gradient. (b) Impact of zeta potential symmetry/asymmetry and increasing electric field oscillation Reynolds number on transverse velocity profiles at different oscillation times: (b-I) for symmetric zeta potentials, low Re_w, and thick EDL; (b-II) for asymmetric zeta potentials, high Re_w, and thin EDL. (c) Effect of increasing asymmetry in zeta potential and varying Re_w on: (c-I,II) the evolution of cross-sectional average concentration profiles, (c-III) the effective dispersion coefficient D_{eff}, and (c-IV) mass transfer rate as a function of Re_w for different Schmidt numbers under oscillatory electric fields. Adapted from ref. 184 with permission from Elsevier B.V., copyright 2018. (d) Schematic of solute dispersion under combined axial electric (Ex) and transverse magnetic (By) fields in a parallel-plate microchannel with weak sinusoidal zeta potential variations along the walls. (e) Influence of zeta potential fluctuation amplitude ($\varepsilon = \Delta\zeta/\zeta_0$) and phase difference θ on axial pressure gradients. (f) Velocity patterns and axial dispersion distribution under type I sinusoidal zeta potential variation; (g) results for type II zeta potential distribution. Adapted from ref. 76 with permission from AIP Publishing, copyright 2017.

Given that the majority of microfluidic systems—such as LOC diagnostic platforms, targeted drug delivery systems, microfluidic pumps, and micromixers—typically operate with viscoelastic biofluids (*e.g.*, blood, cerebrospinal fluid, DNA- or RNA-containing solutions, plasma, and saliva), several valuable investigations have been conducted to evaluate how hydrodynamic dispersion and mass transport of solutes are affected under EOF in such fluids. In particular, the Phan–

Thien–Tanner (PTT) model has been widely employed to describe the rheological behavior of viscoelastic non-Newtonian fluids under both asymmetric[186] and symmetric[98] zeta potential distributions on the microchannel walls.

In general, increasing the parameter εWe^2—which reflects the strength of viscoelastic effects—leads to a significant enhancement of hydrodynamic dispersion. Specifically, Mozafari *et al.*[186] showed that under a fixed zeta potential ratio $R_\zeta = \frac{\zeta_2}{\zeta_1} = 0.5$ (representing maximum asymmetry), increasing R_ζ up to 1 (indicating symmetric wall potentials) leads to reduced dispersion in the case of thick EDL, regardless of fluid rheology. However, in the case of thin EDLs, the trend is reversed—dispersion increases with higher symmetry. Here, We denotes the Weissenberg number, a dimensionless parameter defined as $We = \frac{\Lambda u_{EOF\text{-}HS}}{\lambda_D}$, where Λ is the relaxation time of the fluid, $u_{EOF\text{-}HS}$ is the Helmholtz–Smoluchowski electroosmotic velocity, and λ_D is the Debye length. This number quantifies the relative magnitude of elastic forces compared to viscous forces and serves as a key indicator of viscoelasticity in flow behavior.

In a separate analytical study, Vargas *et al.*[76] in 2017 investigated the simultaneous application of axial electric (Ex) and transverse magnetic (By) fields—resulting in combined EOF and magnetohydrodynamic (MHD) flows—and their influence on the axial effective dispersion coefficient of an electro-neutral solute in a parallel-plate microchannel filled with Newtonian fluid. The study introduced sinusoidally varying wall zeta potentials with different phase shifts (θ) along the axial direction for the top and bottom walls of the channel (Fig. 10d). Two types of zeta potential distributions were considered: in the first type, the top and bottom walls had opposing signs of base zeta potential, while in the second type, both walls had similar (positive) base zeta potentials. The authors used the linearized Debye–Hückel approximation to solve the Poisson–Boltzmann equation for the symmetric electrolyte solution and employed the lubrication approximation to derive the hydrodynamic velocity field. They demonstrated that through careful tuning of key parameters—such as the type of zeta potential distribution, the amplitude of zeta potential oscillations relative to a reference potential (ε), the phase shift θ, and the dimensionless Hartmann number (ΩHa^2) associated with the magnetic field—one can selectively maximize or minimize the axial dispersion coefficient at specific positions along the channel.

As one of the study's key findings, it was shown that the pressure gradient fluctuated significantly along the channel for both types of zeta distributions (Fig. 10e). However, under the combined effects of EOF and MHD flows, the first distribution type (opposite-sign wall potentials) led to more pronounced variations in velocity and effective dispersion (Fig. 10f), compared to the second type (same-sign potentials, Fig. 10g). Ultimately, under the first distribution type with conditions such as high ε (*e.g.*, 0.3), a phase shift of $\theta = \pi$, and a strong magnetic field (ΩHa^2 = 2.5), the system exhibited a complex velocity pattern and peak axial dispersion (Fig. 10f). In contrast, the second distribution type with $\varepsilon \approx 0$, $\theta = 0$, and zero magnetic field yielded a uniform velocity profile close to the classical Helmholtz–Smoluchowski EOF and resulted in minimum axial dispersion (Fig. 10g).

So far, the majority of studies on the effects of various parameters—especially asymmetric zeta potential distributions—on hydrodynamic dispersion in microfluidic systems have primarily focused on the presence of either a constant electric field (DC electroosmosis), an oscillatory electric field (AC electroosmosis), or a magnetic field (magnetohydrodynamics, MHD) in isolation. However, the combined influence of oscillatory electric and magnetic fields on solute dispersion has rarely been addressed. In a recent 2024 study, Das *et al.*[187] presented a comprehensive mathematical model and numerical analysis (Fig. 11a) of solute transport and dispersion in a microchannel under fully developed Newtonian flow. The study involved simultaneous application of a time-dependent sinusoidal oscillatory electric field in the flow direction (comprising both a steady DC and a time-varying AC component) and a uniform transverse magnetic field perpendicular to the flow direction. The key focus was placed on the role of wall zeta potential—examined in three configurations: fully symmetric ($\zeta1 = 1$, $\zeta2 = 1$), partially asymmetric ($\zeta1 = 1$, $\zeta2 = 0$), and fully asymmetric ($\zeta1 = 1$, $\zeta2 = -1$)—as well as the influence of key dimensionless parameters including the Hartmann number, the angular Reynolds number, and zeta potentials on the dispersion coefficient (DT) and average solute concentration profiles (C_m).[187]

One of the major findings was that, under combined DC/AC electroosmotic flow along the axial direction and MHD flow in the transverse direction, and with fixed angular Reynolds number α (or), constant oscillation amplitude ξ, and other parameters (Péclet number, Schmidt number, and Debye length) held constant, an increase in the Hartmann number (Ha)—a measure of magnetic field influence—led to a notable reduction in hydrodynamic dispersion under symmetric zeta potential conditions. This damping effect of the magnetic field results in sharper and taller peaks in the cross-sectional concentration distribution due to reduced dispersion at higher Hartmann numbers (Fig. 11b and c).

Moreover, even under fully asymmetric zeta potentials, increasing the Hartmann number still reduced the overall dispersion; however, the peak values of the dispersion coefficient at any given Hartmann number were significantly higher compared to the symmetric case due to stronger asymmetries in the potential distribution (Fig. 11d). The enhanced damping effect—*i.e.*, the progressive reduction of fluid velocity fluctuations and velocity gradients due to opposing resistive forces such as the Lorentz force under high magnetic field intensity—plays a crucial role here. The Hartmann number, as a key dimensionless parameter in MHD-driven systems, quantifies the ratio of Lorentz to

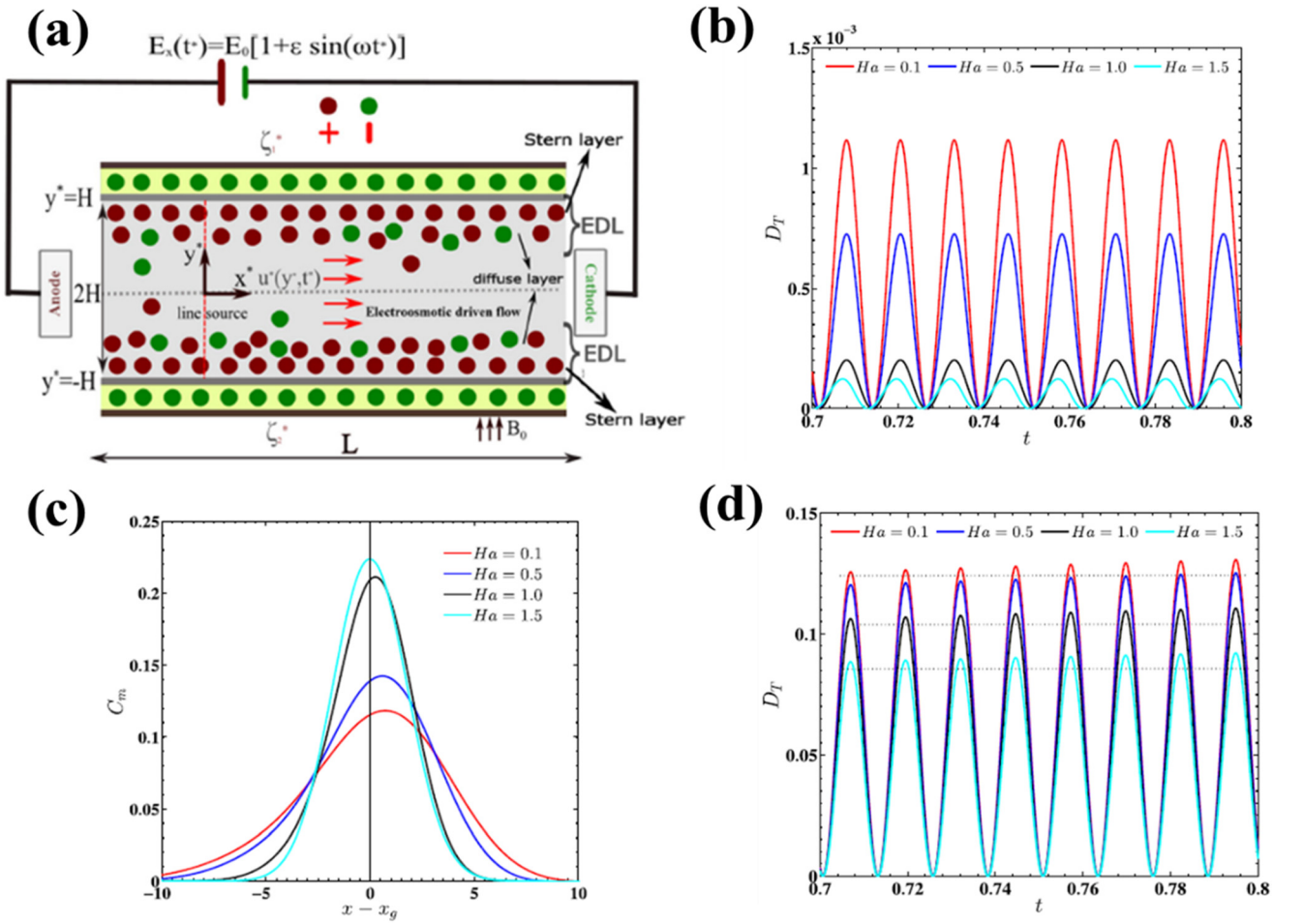

Fig. 11 (a) Schematic illustration of solute dispersion in a microchannel under asymmetric wall zeta potential and simultaneous application of steady (DC) and oscillatory (AC) electroosmotic flows along the axial direction (x), combined with a uniform transverse magnetic field in the y-direction. (b and d) Effect of varying dimensionless Hartmann numbers on the long-time dispersion coefficient under (b) fully symmetric (ζ_1 = 1, ζ_2 = 1) and (d) fully asymmetric (ζ_1 = 1, ζ_2 = −1) zeta potential configurations. (c) Corresponding changes in the cross-sectional average concentration profiles under symmetric zeta conditions. All simulations are performed with fixed values of κ = 10, $\alpha = \mathrm{Re_w}$ = 0.5, Pe = 100, ξ = 1, and Sc = 1000. Adapted from ref. 187 with permission from AIP Publishing, copyright 2024.

viscous forces and is fundamental to controlling velocity profiles and solute dispersion in microfluidic platforms. Overall, this study demonstrated that if the goal is to optimize chemical reactions in microreactors or improve the performance of microfluidic systems for targeted drug delivery or lab-on-a-chip applications, the synergistic use of oscillatory electric fields alongside magnetic fields can significantly enhance control over solute dispersion—more so than using magnetic fields alone.[187]

Practical considerations. Field-driven control methods rely on precise voltage regulation and electrode placement, which may introduce joule heating, bubble formation, or electrolysis in aqueous systems. Moreover, the electrical and thermal conditions required for dispersion suppression must remain within biocompatible limits, restricting the applicability of strong-field actuation in biosensing and cell-based lab-on-a-chip devices.

Although reducing axial hydrodynamic dispersion is often favorable—particularly in electroosmotic mixing processes within microchannels that rely on non-uniform zeta potential distributions or oscillatory flow fields—dispersion itself can act as an effective mechanism for generating transverse concentration gradients and enhancing electroosmotic mixing efficiency. However, due to the inherently low Reynolds numbers and laminar flow regime characteristic of microfluidic systems, transverse mixing of solutes is typically dominated by slow molecular diffusion (*i.e.*, diffusive Péclet numbers), which significantly limits mixing efficiency unless the channel is excessively long with extended residence times. To overcome these limitations and accelerate transverse mixing by complementing diffusion with convective mechanisms, several techniques have been proposed. Among these, introducing non-uniform zeta potential patterns on channel walls—*via* surface patterning with discrete regions of differing surface charge—is a promising strategy. For instance, by embedding multiple patches with locally opposite surface

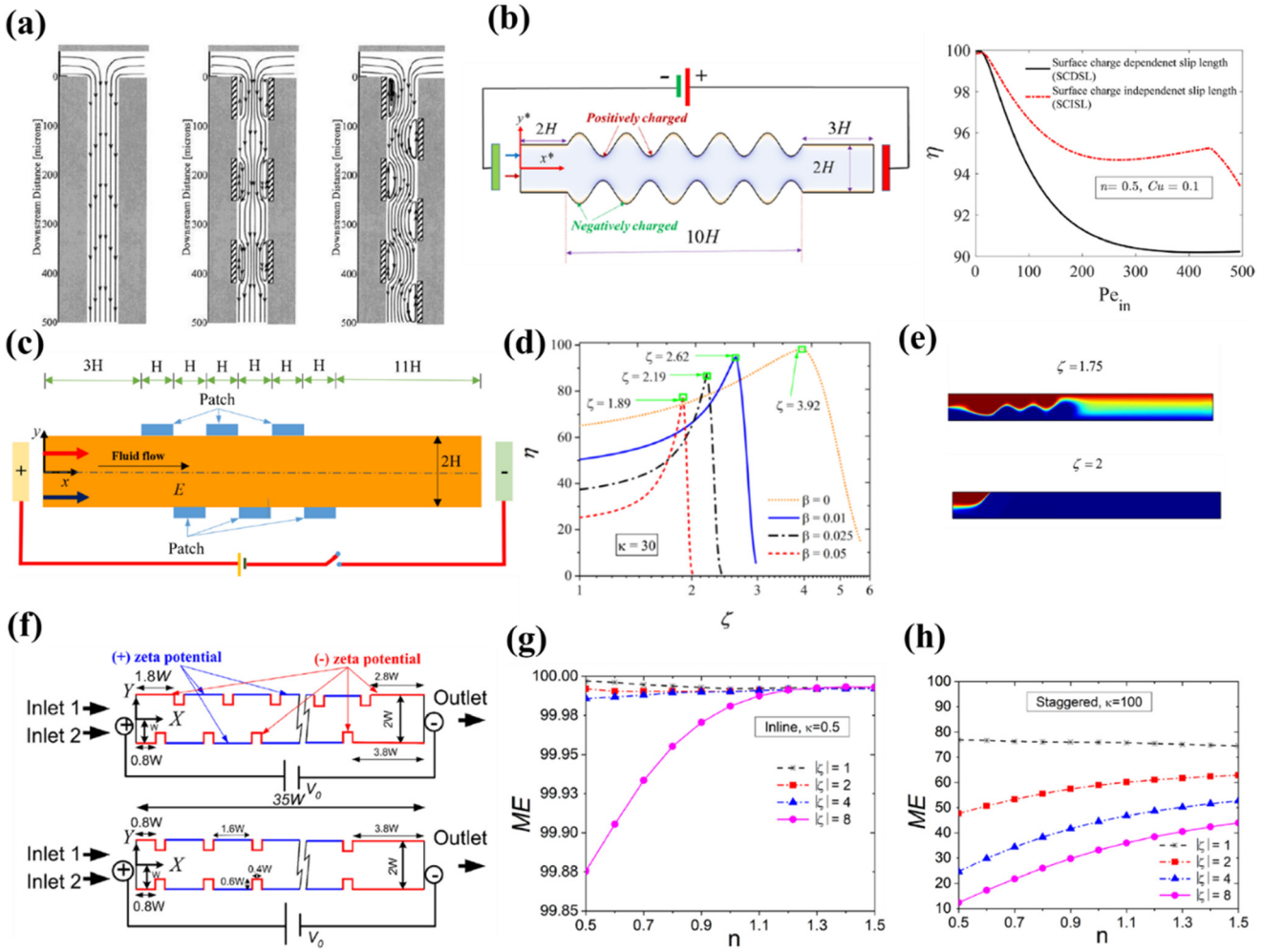

Fig. 12 (a) Comparison of electroosmotic mixing performance in three surface conditions of a T-shaped micromixer: (left) a homogeneous wall with constant zeta potential ζ = −42 mV, (middle) six uniformly distributed heterogeneous zeta potential patches, and (right) a stepwise heterogeneous patch distribution across the mixing channel walls. Adapted from ref. 188 with permission from ACS Publishing, copyright 2002. (b) Schematic of a sinusoidally wavy micromixer with spatially varying surface charge, and the corresponding mixing efficiency under two slip-length conditions—surface charge dependent (SCDSL) and independent (SCISL)—over a wide range of Péclet numbers, for a non-Newtonian fluid with power-law index n = 0.5 and Carreau number Cu = 0.1. Adapted from ref. 189 with permission from AIP Publishing, copyright 2024. (c) Schematic of a rectangular hydrophobic micromixer with slip boundaries composed of positively charged heterogeneous patches and negatively charged homogeneous zones, used for the electroosmotic mixing of fluorescent tracer and dilute Newtonian buffer. (d) Electroosmotic mixing efficiency as a function of patch zeta potential for different dimensionless slip lengths, at fixed parameters κ = 30 and Pe = 100. (e) Contour plots of tracer concentration for two distinct patch zeta potentials at β = 0.05 and κ = 30, illustrating enhanced mixing for moderate patch potentials and primary flow choking at excessively high values. Adapted from ref. 190 with permission from Elsevier B.V., copyright 2022. (f) Schematic of two micromixer designs with differently arranged obstacles: staggered (top) and inline (bottom). In both configurations, negative zeta potential is applied to the inlet/outlet walls and obstacle surfaces, while the rest of the channel wall is positively charged. (g and h) variation of electroosmotic mixing efficiency *versus* power-law index n for different zeta potential levels, comparing (g) inline configuration with κ = 0.5 and (h) staggered configuration with κ = 100. Adapted from ref. 191 with permission from Elsevier B.V., copyright 2022.

charges along the channel walls, recirculation zones or vortical structures can be induced. These zones alter the direction of electroosmotic streamlines locally, promoting secondary flows that significantly enhance transverse mixing performance.

In this context, Erickson and Li[188] employed 3D numerical simulations using the finite element method to investigate the impact of heterogeneous surface zeta potential on electroosmotic mixing efficiency in a T-shaped micromixer. They applied a 500 V cm^{-1} electric field to drive the electroosmotic flow along a 15 mm mixing channel and introduced six equal-sized surface patches with zeta potentials of ζ = −42, −21, 0, +21, +42 mV in both symmetric and asymmetric arrangements (Fig. 12a). For comparison, a baseline homogeneous surface with ζ = −42 mV was used. Their results showed that greater differences in zeta potential between heterogeneous patches and surrounding regions (*i.e.*, increased surface heterogeneity) led to stronger recirculation flows and higher mixing efficiency. In the most extreme case—contrasting ζ = +42 mV patches with a ζ = −42

mV background—a 30% reduction in required mixing length and a 70% mixing efficiency were achieved.

Building on this concept, Khatibi *et al.*[189] conducted a comprehensive numerical simulation using coupled solutions of the Laplace, Poisson–Boltzmann, Navier–Stokes, and advection–diffusion equations *via* finite element analysis. They investigated the impact of wall slip length, both dependent and independent of surface zeta potential (SCDSL and SCISL conditions), on the flow field and mixing efficiency in a wavy micromixer with sinusoidally varying surface charge (Fig. 12b). The slip length formulation was derived from molecular dynamics simulations and treated as a function of local surface charge. A Carreau model was adopted to characterize the non-Newtonian shear-thinning fluid, with behavior index $n < 1$. The results revealed that for a fixed Carreau number Cu = 0.1 and flow behavior index n = 0.5, electroosmotic mixing efficiency under SCISL conditions was consistently superior to SCDSL across most values of the diffusive Péclet number—particularly within the 0–100 range. At Pe = 200, the mixing efficiency dropped from 95.5% (SCISL) to 91.5% (SCDSL), indicating that a slip length independent of local surface charge results in more effective electroosmotic mixing.

Vasista *et al.*[190] conducted a theoretical and numerical investigation using the finite element method to explore electroosmotic mixing efficiency in a hydrophobic micromixer (with slip surfaces), incorporating heterogeneous surface conditions composed of patches with non-uniform zeta potential embedded among homogeneous wall segments (Fig. 12c). The surface zeta potential was modeled as a nonlinear function dependent on the dimensionless zeta potential of patches, background wall zeta potential, wall slip length, and the Debye–Hückel parameter. As shown in Fig. 12d, for constant parameters κ = 30 and Pe = 100, and for various dimensionless slip lengths, the electroosmotic mixing efficiency η increased gradually with the dimensionless zeta potential of the patch region, reaching a maximum at a critical zeta potential value specific to each case. However, beyond this critical value, further increases in patch zeta potential led to a sharp decline in mixing efficiency, attributed to the excessive velocity of recirculation zones (UR) and primary flow choking. Based on Fig. 12e, this phenomenon was particularly evident for β = 0.05 and ζ_{patch} = 2 $\gg$ ζ_{crit} =1.89, where the primary flow was obstructed by intensified secondary vortices. In contrast, for ζ_{patch} = 1.75 $\ll$ 1.89, efficient electroosmotic mixing was achieved through moderate recirculation near the patches. Notably, in the no-slip case (β = 0), the critical zeta potential shifted to a higher value (ζ_{crit} = 3.92) due to reduced flow perturbation and enhanced convective mixing stability, resulting in near-perfect (~100%) mixing efficiency.

In a subsequent study, Mehta *et al.*[191] performed a two-dimensional numerical simulation in 2022 to investigate electroosmotic mixing of non-Newtonian fluids obeying the power-law model, focusing on the role of zeta potential heterogeneity and geometric obstacles within a micromixer featuring two inlets and one outlet (Fig. 12f). In their model, the red lines on the inlet, outlet, and surface of embedded obstacles carried negative zeta potentials, while the rest of the channel walls had positive values. The dimensionless zeta potential ranged from 1 to 8 (corresponding to ~±25 mV to ±200 mV), the Debye parameter κ varied from 0.5 to 100, and the power-law index nn ranged from 0.5 to 1.5. These represented Newtonian fluids (*e.g.*, water, n = 1), shear-thickening fluids ($n > 1$), and shear-thinning fluids (*e.g.*, blood, dilute polymer solutions, $n < 1$). Their findings emphasized the critical dependence of recirculation zone formation and mixing performance on obstacle layout, zeta potential patterns, and rheological properties. Under inline obstacle arrangements (bottom layout in Fig. 12f), thick Debye layers (κ = 0.5), high zeta potential (ζ = 8), and increasing nn led to nearly 100% mixing efficiency (Fig. 12g). In contrast, for staggered obstacle arrangements (top layout in Fig. 12f), thin Debye layers (κ = 100) and low zeta potential (ζ = 1), along with shear-thickening behavior, yielded a maximum of ~75% efficiency (Fig. 12h). These results highlight the tunability of electroosmotic mixing through combined control of surface charge heterogeneity, electrical double-layer thickness, and fluid rheology.

3.4. Surface roughness

The Surface roughness or wall irregularities in micro- or nano-scale microfluidic systems represent another critical morphological factor that can be effectively leveraged to control and enhance the hydrodynamic dispersion of solutes. Typically manifested as micro- or nano-scale surface perturbations or cavities along the channel walls, surface roughness can induce localized fluctuations in the velocity field and disrupt the structure of the boundary layer, thereby significantly altering transverse transport, modifying axial velocity profiles, and ultimately influencing the global dispersion behavior of solutes. These irregular cavities, especially in microporous systems, can feature various geometric configurations such as sinusoidal, triangular, rectangular, square, elliptical, random, or complex disordered morphologies, arranged in symmetric, asymmetric, periodic, or non-periodic patterns. Thus, surface roughness functions not only as a structural property of the channel morphology but also plays a pivotal role in critical applications such as precision-guided analyte transport in LOC platforms, performance optimization in mass transport systems, and targeted drug delivery in biomicrochannels. Furthermore, surface roughness can substantially affect other aspects such as fluid–wall interactions, velocity distributions, solute concentration profiles, and various transport and interfacial phenomena.

In 2021, Zheng *et al.*[192] conducted a numerical investigation using the lattice Boltzmann method (LBM) at the pore scale and developed a novel triple-effect analytical model to quantify the effective dispersion coefficient under the simultaneous influence of three key surface complexity mechanisms: hydraulic tortuosity

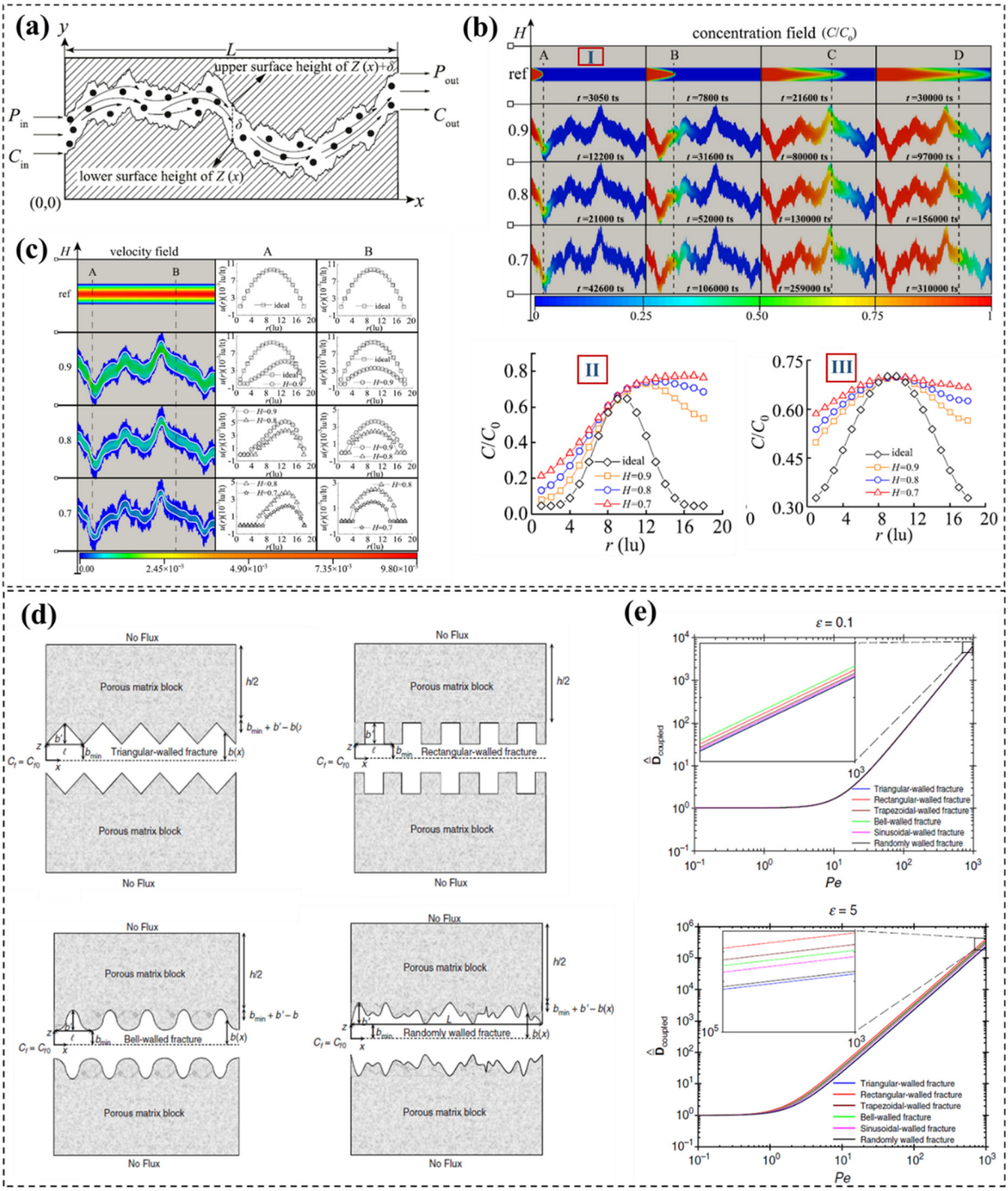

Fig. 13 (a) Schematic illustration of solute dispersion in fluid flow through a naturally designed rough and tortuous micro-aperture. The parameter δ denotes the aperture size of the microfracture. (b-I) Time-dependent solute concentration contours during advection–diffusion transport for both ideal and non-ideal rough microfractures with various surface roughness levels characterized by different H parameters, shown across four cross-sections of the fracture. Here, l_u and ns represent the length and time units, respectively. The parameter H is a statistical and critical index used to quantify surface roughness complexity; smaller H values indicate higher roughness and greater tortuosity, whereas larger values correspond to smoother surfaces. (b-II and b-III) Comparisons of dimensionless solute concentration profiles at sections A and D, respectively, for all four types of microfracture surfaces. (c) Velocity field profiles in ideal and rough microfractures at two different cross-sections, illustrating the effects of varying H. The spatial uniformity of velocity and suppression of advection-driven dispersion are evident in H = 0.7. Regions of stagnant flow (dead zones) near the rough walls are shown in dark blue, whereas flowing regions are shown in light blue, separated by white lines. Adapted from ref. 192 with permission from Elsevier B.V., copyright 2021. (d) Schematic representation of a coupled system consisting of a permeable matrix structure and a rough-walled fracture featuring different geometrical patterns, including triangular, rectangular, sinusoidal, and randomly rough (disordered) morphologies. (e) Influence of different rough fracture geometries on the variation of the dimensionless average shear dispersion coefficient of the coupled system as a function of the Péclet number, evaluated at two different values of relative roughness parameter. Adapted from ref. 99 with permission from SPE Publishing, copyright 2018.

(τ_h), surface tortuosity (τ_s), and stationary surface roughness (f_σ). This framework was applied to analyze advection–diffusion transport in a natural rough-walled aperture with intricate geometric features (Fig. 13a). They showed that incorporating these three effects into the transport process fundamentally alters the classical Taylor–Aris dispersion formulation derived for ideal smooth fractures such as parallel-plate channels. Notably, they found that increasing the stationary surface roughness significantly suppresses advection-driven dispersion due to the presence of dead zones—regions near rough surfaces with negligible flow velocity. Consequently, the overall effective dispersion becomes dominated by the slow molecular diffusion mechanism. To support these findings, Zheng *et al.* used steady-state LBM simulations to extract spatial velocity and concentration profiles for both idealized and rough apertures at different values of the roughness parameter H (Fig. 13b and c). From the concentration distributions at cross-section D (Fig. 13b-I), it was evident that dispersion in the rough aperture (H = 0.7) occurred over a significantly longer timescale than in the ideal case, highlighting the reduced contribution of advection and enhanced dominance of molecular diffusion. Moreover, the transition from a partial Gaussian to a full Gaussian distribution (Fig. 13b-II) and the increased uniformity of concentration profiles (Fig. 13b-III) further confirmed the impact of increased roughness on solute transport behavior. In Fig. 13c, they illustrated how in ideal channels the velocity peaks at the center and vanishes near the walls due to no-slip conditions, while in rough apertures with decreasing H, the presence of geometric obstructions and dead zones leads to decreased flow velocities and increased stagnant regions, thereby reducing the effective cross-sectional area for solute transport.

In a complementary experimental study, Togi *et al.*[193] investigated the influence of controlled lateral wall roughness in 2D microchannels on solute dispersion. Using absorption photometry to visualize copper sulfate dispersion in glycerol (a viscous solvent used to ensure low Reynolds numbers), they varied the geometric parameters of roughness, such as amplitude and wavelength, across a wide Péclet number range (100–1000). Their results indicated that increased roughness amplitude or reduced wavelength enhanced the formation of stagnant water regions and thereby increased dispersion, whereas the absence of such zones led to a notable reduction in velocity gradients and solute spreading. Dou *et al.*[194] further explored how multiscale roughness features—primary (large-scale) and secondary (small-scale)—independently or jointly affect the scaling relation between axial dispersion and the Péclet number. While ideal channels follow a quadratic Pe–dispersion relationship, rough channels deviate depending on the dominant transport mechanism (diffusion, Taylor dispersion, or macrodispersion), resulting in polynomial, linear, or power-law correlations.

In 2018, Dejam *et al.*[99] developed an analytical model relating the shear dispersion coefficient to the Péclet number and relative roughness parameter (ε_R, defined as the ratio of maximum wall protrusion height to the shortest distance from the fracture center to the wall). They considered various deterministic and random geometries—triangular, rectangular, trapezoidal, sinusoidal, bell-shaped, and random (Fig. 13d). Their results (Fig. 13e) showed that both increasing Péclet number and roughness ratio ε_R led to enhanced dispersion, though the degree varied by geometry. Bell-shaped roughness yielded the highest dispersion in the low roughness regime (ε_R = 0.1), while rectangular roughness dominated in the moderate regime (ε_R = 5). In contrast, triangular and random patterns consistently exhibited the lowest shear dispersion across both ranges. Finally, Haugerud *et al.*[195] numerically modeled Taylor dispersion under periodic square roughness and varying fluid inertia to assess the combined effects of surface discontinuity and inertial forces. In a related study, Sengupta *et al.*[196] investigated solute dispersion in sinusoidally rough-walled microtubes under combined EOF and pressure-driven flows, illustrating how such complex configurations can critically modulate mass transfer dynamics.

3.5. Surface adsorption, bulk reaction, and desorption

Another important approach to controlling the hydrodynamic dispersion of reactive solutes in microfluidic systems is to consider surface boundary conditions involving adsorption and desorption reactions on the channel walls. Surface adsorption refers to the accumulation of solute species on the solid walls from the bulk fluid, whereas desorption corresponds to the release of previously adsorbed molecules back into the fluid phase. When reactive solute species undergo surface adsorption on the channel walls, they are effectively removed from the bulk flow, generating significant transverse concentration and velocity gradients—especially in the near-wall regions where both solute concentration and flow velocity are considerably lower than those in the channel center. This creates a driving force for solute transport from the central region toward the wall, thus influencing the dispersion behavior. By controlling the rate parameters of surface adsorption and desorption, it is possible to either enhance or suppress transverse gradients of concentration and velocity, thereby modulating the extent of hydrodynamic dispersion. In general, the influence of adsorption/desorption and bulk reactions on dispersion is nonlinear and highly dependent on the extent of solute interaction with the channel surfaces. For example, in the case of high surface adsorption rates (high Damköhler number, Da), the solute concentration near the walls drops sharply, suppressing solute redistribution between slow- and fast-moving streamlines and resulting in reduced overall dispersion. Conversely, under low adsorption rates (low Da), the solutes have sufficient time to redistribute across streamlines, leading to enhanced hydrodynamic dispersion.

In addition to surface reactions, chemical reactions may also occur in the bulk of the fluid. Two main types of surface reactions are commonly considered: (i) reversible adsorption–desorption reactions, where solutes attach to the wall with

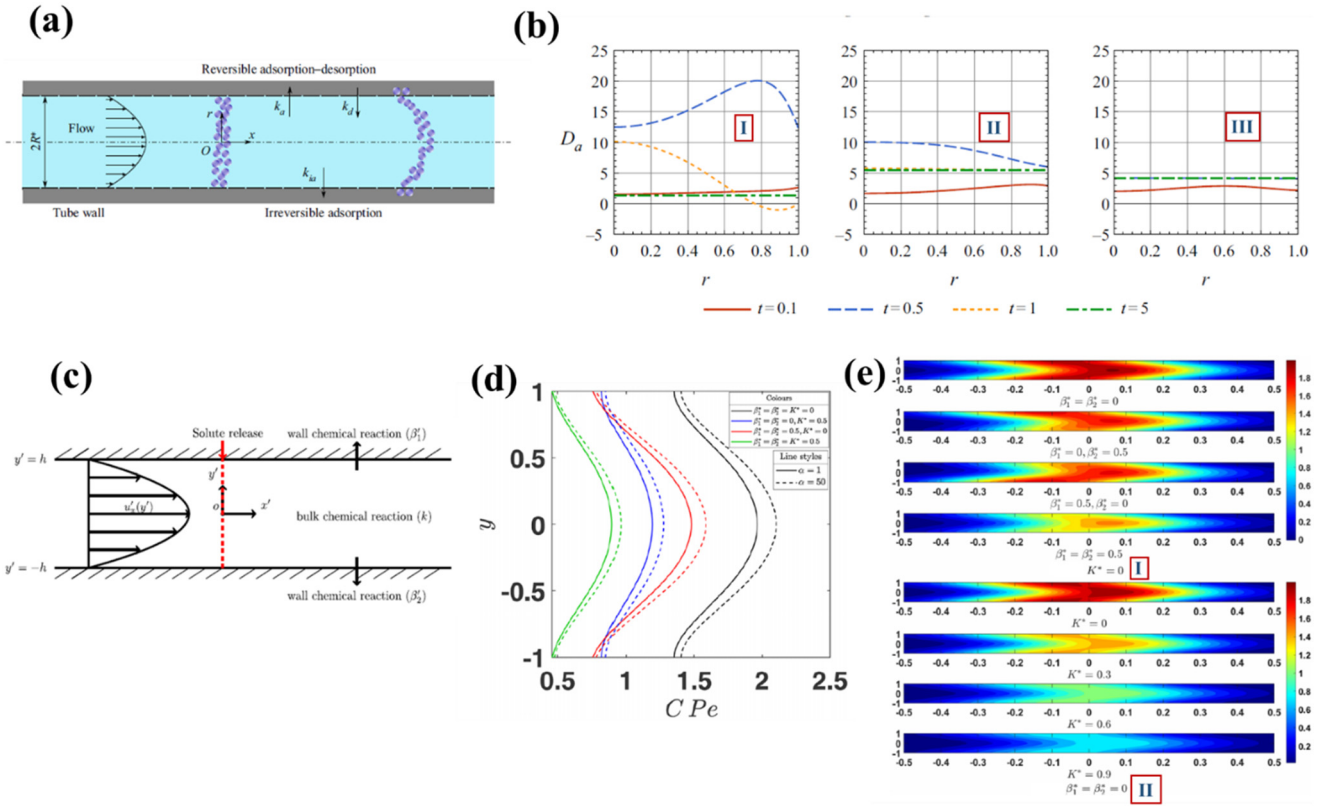

Fig. 14 (a) Schematic illustration of solute dispersion in shear-driven fluid flow through a microtube, with reversible surface adsorption–desorption reaction on the upper wall and irreversible wall absorption on the lower wall. (b) Axial growth rate of solute dispersion in the fluid bulk Da across the radial direction of the tube, over early to long-time regimes for various desorption rate constants: (b-I) k_d = 1, (b-II) k_d = 10, and (b-III) k_d = 100, under fixed conditions: k_a = 10, k_{ia} = 0, and Pe = 10. Adapted from ref. 201 with permission from Cambridge University Press, copyright 2022. (c) Schematic of solute band injection in a parallel-plate channel subjected to asymmetric surface adsorption reactions on both walls and a first-order homogeneous bulk reaction. (d) Effect of couple stress parameter α and varying wall reaction rates β1, β2, and bulk reaction rate k_{BR} on the transverse solute concentration profile at a fixed time and position. (e) Two-dimensional concentration contours showing (e-I) the effect of β1, β2 without bulk reaction, and (e-II) the effect of different kBRkBR values in the absence of surface reactions, for α = 1. Adapted from ref. 204 with permission from APS Publishing, copyright 2025.

rate constant k_a and detach back into the fluid with rate k_d, and (ii) irreversible wall absorption, where solutes are permanently adsorbed on the wall at a rate, without returning to the fluid phase. Reversible reactions are particularly relevant in practical systems such as biosensors, gas chromatography, and physiological processes like oxygen exchange between alveoli and blood flow.[197,198]

The Damköhler number, a dimensionless parameter quantifying the relative importance of reaction kinetics to transport processes, is defined for adsorption as $\mathrm{Da} = \frac{k_a C H^2}{D}$, where kaka is the adsorption rate constant, C is solute concentration, H is a characteristic length scale (*e.g.*, channel half-height), and D is the molecular diffusion coefficient.[199,200]

Several studies have examined the effects of wall and bulk reactions on solute dispersion. Jiang *et al.*[201] analytically investigated transient shear dispersion of reactive solutes in a channel with reversible and irreversible surface reactions on opposite walls (Fig. 14a). Their results (Fig. 14b) show that at early times and with low desorption rate $\ll k_a$, dispersion is dominated by longitudinal diffusion, resulting in uniform Da across the cross-section. As time progresses, shear-induced dispersion becomes more prominent, especially near the walls. However, at long times, dispersion is again reduced due to solute depletion near the walls caused by strong adsorption. Other studies explored more complex flow behaviors. For example, in a parallel-plate channel rotating about an axis normal to the flow, Coriolis forces were shown to shift peak velocities toward the wall, flatten the velocity profile, and produce nonlinear variations in dispersion along the primary and secondary flow directions.[202]

Roy and Bég[203] developed a two-fluid model to describe the unstable dispersion of reactive solutes like oxygen in blood, modeled as a micropolar fluid in the core region and Newtonian plasma in the surrounding layer, under axial pressure-driven flow. Analytical expressions for dispersion and concentration profiles were derived. They found that increasing the micropolar coupling number and bulk reaction rate significantly reduces dispersion, whereas increasing the viscosity ratio slightly enhances it. In a recent study, Radha S *et al.*[204] used multiscale homogenization to derive high-order

analytical expressions for average and transverse concentration distributions in a couple stress fluid subjected to simultaneous surface and bulk first-order reactions (Fig. 14c). They showed that small values of the couple stress parameter (α) lead to higher dispersion, while large $\alpha\alpha$ reduces it. Moreover, the presence of both wall and bulk reactions significantly suppressed hydrodynamic dispersion compared to the no-reaction case (Fig. 14d and e).[205]

Additional studies have addressed electro-magnetohydrodynamic (EMHD) flows of couple stress fluids under nonuniform wall absorption,[206] dispersion in Carreau–Yasuda fluids in circular channels,[207] and combined effects of bulk and heterogeneous surface reactions in oscillatory MHD flows through porous media, where dispersion was shown to increase with the Darcy number due to higher permeability.[208]

Practical considerations. Surface modification strategies, such as charge patterning or grafted polymer coatings, can effectively tune electroosmotic flow and dispersion, yet they present reproducibility and durability challenges. Many coatings degrade under prolonged exposure to buffers, organic solvents, or cleaning agents, and large-scale patterning on curved microchannels remains technically demanding. Ensuring uniform coating thickness and maintaining optical transparency further constrain their integration into diagnostic microfluidic systems.

4. Auxiliary methods for controlling hydrodynamic dispersion

Considering the main objective of this study and the inherent inevitability of hydrodynamic dispersion in microscale systems, in addition to the primary control strategies discussed in previous sections, there exist several auxiliary approaches that can effectively modulate or enhance solute band dispersion in microfluidic environments. These include the introduction of secondary flow streams by applying lateral or transverse flows within the channel cross-section, the use of electrolyte solutions with tailored physical properties, and the modification of channel walls through polyelectrolyte coatings. Furthermore, the engineering of customized flow velocity profiles can also serve as a powerful means to influence solute spreading. Each of these supplementary strategies can play a significant role in precisely regulating the extent and behavior of dispersion, thereby contributing to improved control over mass transport in lab-on-a-chip devices and other microfluidic applications.

4.1. Secondary lateral flows

The One alternative strategy to significantly reduce the overall effective dispersion coefficient—and consequently hydrodynamic dispersion of solutes—is to enhance transverse diffusion (*i.e.*, diffusion perpendicular to the main flow direction) or lateral mixing mechanisms. While operating under turbulent flow conditions is one obvious means of achieving this goal, excessive turbulence is often accompanied by undesirable increases in axial advective dispersion. Moreover, the development of turbulent flow is fundamentally infeasible in most micro- or nanoscale microfluidic systems, which typically operate under very low Reynolds number regimes. In recent years, researchers have explored various approaches to enhance sample separation performance in chromatographic columns by effectively suppressing axial Taylor–Aris dispersion. These improvements have largely been attributed to the generation of cross-sectional vortices, either induced by EOF under DC electric fields or by employing chaotic advection mechanisms.[209–212] Another promising approach for mitigating axial dispersion, particularly under laminar flow conditions, involves the induction of lateral or secondary flows within the channel cross-section. These lateral circulations (also referred to as spin-up flows) act to reduce axial dispersion while enhancing cross-sectional mixing. This is particularly beneficial in microfluidic chromatography applications, where efficient separation of solute bands depends heavily on minimizing axial dispersion and accelerating mass transfer between the mobile and stationary phases. For the effective implementation of such methods, certain criteria must be satisfied—namely, uniform distribution of secondary flows across the entire channel cross-section, avoidance of inducing additional axial flow components, and compatibility with micro- and nanoscale system geometries. Among the most practical techniques for inducing such flows and reducing Taylor dispersion are: AC electroosmotic actuation;[213,214] excitation of magnetic nanoparticles using rotating magnetic fields;[215,216] use of spiral, coiled, or curved channels to generate Dean vortices;[217–219] and acoustic streaming induced by acoustic waves.[220,221] These methods have found diverse applications in improving chromatographic separation, homogenizing residence time distribution, enhancing reaction yields in microreactors, and accelerating mixing and mass transfer. In addition, some studies have investigated the control of solute dispersion through uniform cross-flow application in channels featuring surface adsorption or porous wall interactions, where increasing the cross-flow rate contributes to dispersion mitigation.[222]

In a notable experimental study, Hajiani and Larachi (2012)[215] introduced a novel mechanism termed lateral nanomixing—based on the excitation of suspended iron-oxide magnetic nanoparticles in dilute ferrofluid *via* a uniform transverse rotating magnetic field (TRMF)—as an effective means of suppressing axial Taylor dispersion and enhancing cross-sectional mass transfer in laminar Poiseuille flow within a capillary tube. Their system (Fig. 15a) demonstrated a significant narrowing of residence time distribution (RTD) peaks as the magnetic field intensity increased from 10.4 to 36.5 kA m^{-1} at a constant rotation frequency of 50 Hz, indicating reduced axial dispersion due to formation of nanoscale lateral convective vortices (Fig. 15b). Additionally, increasing rotation frequency further decreased the slope of axial dispersion *versus* Reynolds

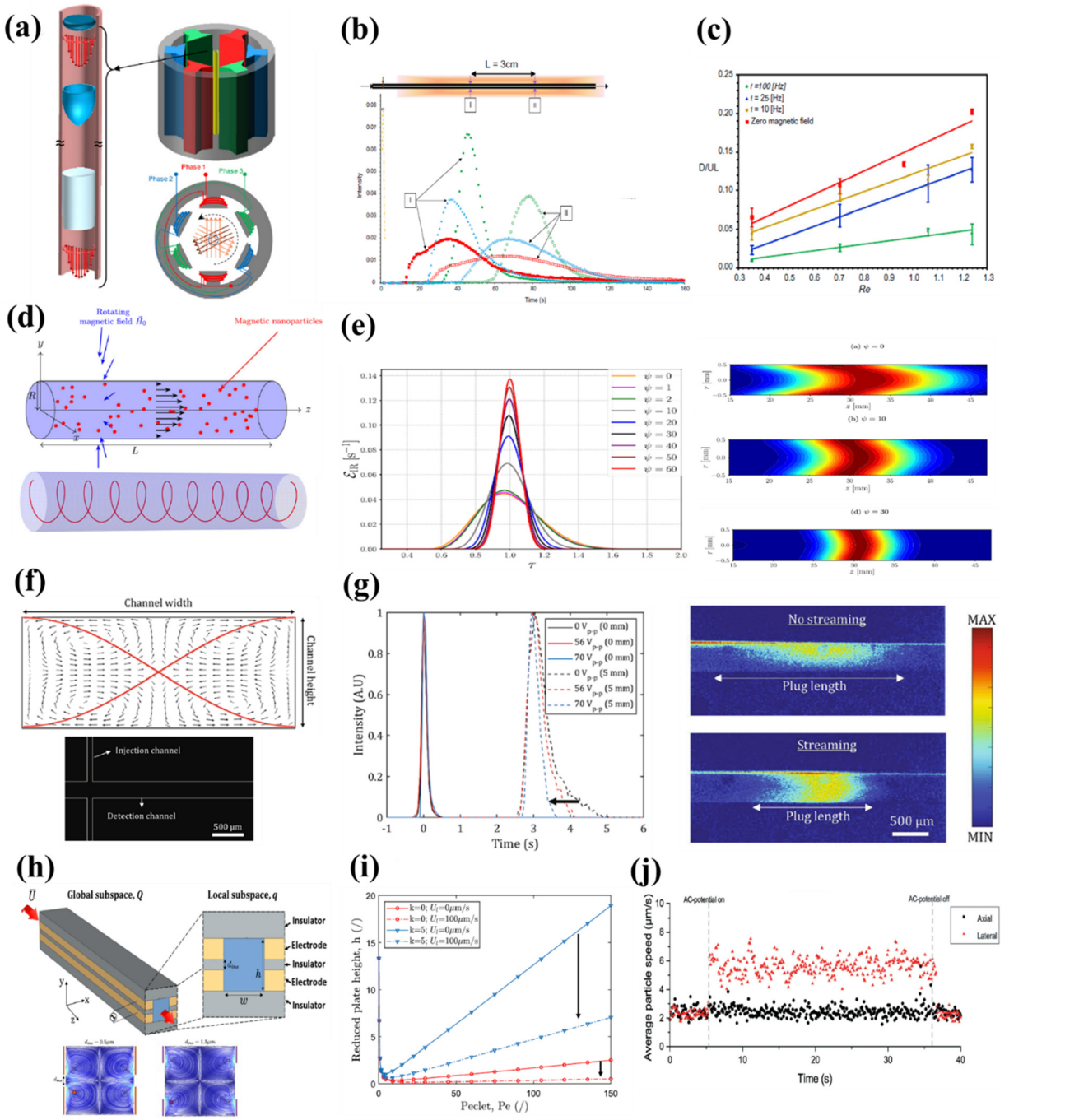

Fig. 15 Implementation of various secondary lateral flows for controlling axial hydrodynamic dispersion of solute bands. (a) Experimental setup for generating a lateral nanomixing/convective mechanism by exciting nanoparticles suspended in a dilute ferrofluid using a transverse rotating magnetic field (TRMF) within a glass capillary under laminar Poiseuille flow. (b and c) Effect of varying TRMF intensity and frequency, respectively, on the system's time response to tracer pulse injection (as detected by RTD profiles) and the enhancement of lateral nanomixing in the presence or absence of TRMF. Adapted from ref. 215 with permission from Elsevier B.V., copyright 2012. (d) Formation of spin-up flows across the capillary cross-section *via* magnetic excitation of nanoparticles under TRMF. (e) Impact of the dimensionless mixing factor on the RTD response and solute band broadening visualized *via* 2D concentration contours. Adapted from ref. 107 with permission from Elsevier B.V., copyright 2024. (f) Velocity field lines following application of acoustic streaming as a lateral secondary flow. (g) Influence of varying acoustic excitation voltages on the peak width of injected tracer bands, under conditions with and without acoustic streaming. The location labeled "0 mm" denotes the initial tracer plug injection point, while "5 mm" indicates the downstream position 5 mm beyond the initial injection site. The tracer plug was injected at a velocity of 1.76 mm s^{-1} in a shallow microchannel of 33 μm depth. Adapted from ref. 63 with permission from Elsevier B.V., copyright 2021. (h) Schematic of a rectangular chromatographic column showing lateral vortices formed around electrodes following AC electroosmotic actuation. (i) Effect of retention factor and the presence/absence of AC electroosmotic flow on the reduced plate height, used as a measure of sample band dispersion in vortex-assisted chromatographic columns. Adapted from ref. 108 with permission from Elsevier B.V., copyright 2024. (j) Differential impact of AC electroosmotic flow (as a lateral secondary flow) on the time evolution of particle average lateral and axial velocities. Adapted from ref. 214 with permission from RSC Publishing, copyright 2020.

number, signifying more efficient lateral mixing and dispersion suppression (Fig. 15c). In their follow-up 2013 study, Hajiani and Larachi[216] extended their experimental analysis by comparing the effects of rotating (TRMF), oscillating (TOMF), and stationary axial magnetic fields (ASMF), finding that TOMF alone failed to induce meaningful lateral mixing.

In a recent theoretical and numerical investigation, Larbi *et al.* (2024)[107] developed a comprehensive mathematical model to describe the centrifugal spin-up flows generated by transverse rotating magnetic fields and their impact on axial dispersion reduction. They introduced a new dimensionless parameter, the mixing factor (ψ), defined as the ratio of lateral to axial convective velocities, and used it to predict axial dispersion behavior *via* RTD analysis. As ψ increased, RTD peaks became sharper with reduced tailing and variance, reflecting enhanced radial concentration uniformity and minimized axial spreading (Fig. 15d and e).

Another innovative approach was demonstrated by Gelin *et al.* (2021),[63] who employed acoustic streaming as a means of generating lateral vortices and reducing axial Taylor–Aris dispersion in rectangular microchannels with varying depths (33–210 μm). By injecting fluorescent tracer plugs and applying a 2 MHz acoustic field using a PZT transducer at 62 Vp-pp-p, they observed a twofold reduction in axial dispersion (Fig. 15g), particularly in the shallower channels, as evidenced by narrower RTD peaks. However, despite its potential, the application of acoustic streaming remains technically limited in deeply miniaturized systems (*e.g.*, submicron-scale nanofluidic channels) due to lower efficiency and reduced scalability of acoustic actuation methods.[223]

In addition to the implementation of steady lateral secondary flows in most prior studies, unsteady or time-dependent lateral flows (*e.g.*, periodic or oscillatory in nature) have also demonstrated promising effects in effectively suppressing axial Taylor–Aris dispersion. One of the key advantages of such unsteady lateral flows—such as periodic electroosmotic flow—is their reduced voltage requirement compared to steady lateral flows like conventional DC-driven electroosmosis.[224] In 2020, Westerbeek *et al.*[214] utilized time-periodic lateral electroosmotic flow, applied transversely (radially) to a pressure-driven axial flow, and introduced a new method termed vortex chromatography in a 40 μm × 20 μm microchannel (aspect ratio AR = 2) under unretained conditions. Their results showed a threefold reduction in the kariskaris parameter, which corresponds directly to a suppression in Taylor–Aris axial dispersion and a decrease in the reduced plate height—both of which enhance chromatographic resolution. Later in 2023,[213] under the same unretained conditions and lateral electroosmotic flow configuration, they further demonstrated that decreasing the channel size or increasing its aspect ratio could lead to even greater reductions in the kariskaris parameter, particularly for larger solute molecules such as dextran. Using channels of 3 μm × 20 μm and 5 μm × 20 μm (aspect ratios up to ~6.7), they achieved dispersion reductions of 44% and 80%, respectively. The retention factor (denoted K) quantifies the chemical or physical interaction of analyte molecules with the channel walls, indicating how long an analyte resides in the stationary phase (walls) *versus* the mobile phase (bulk flow). For $K = 0$, the analyte flows entirely in the mobile phase, whereas for $K > 0$, it experiences some degree of wall interaction or surface adsorption.

Unlike these previous unretained-flow studies, Bihi *et al.*[108] investigated the retained case and developed a numerical model using COMSOL Multiphysics, based on the Generalized Dispersion Theory (GDT) or Macrotransport Theory. They evaluated the effects of lateral AC electroosmotic flow, geometric aspect ratio (AR), retention factor K, and molecular diffusivity on axial Taylor–Aris dispersion—one of the primary limiting factors in the separation performance of open-tubular vortex chromatography columns. As depicted in Fig. 15h, they placed four electrodes on the vertical walls of a rectangular microchannel with a width of 3 μm and variable depth (AR = 1, 4, and 8). Upon applying an alternating electric field across these electrodes, four lateral AC electroosmotic vortices were generated around the electrode regions.

These vortices induced a significant velocity difference between the lateral and axial motion of solute particles, indicating the presence of a strong lateral electric field due to the micrometer-scale spacing of electrodes. Before exposure to the lateral AC flow, particle velocities in both directions were approximately equal, as shown in Fig. 15j. One of the main findings by Bihi *et al.* was that under an applied lateral voltage of up to 300 mV at 10 kHz and for AR = 1, a strong lateral AC electroosmotic flow with an average velocity of 100 μm s^{-1} was established. Under these conditions, the reduced plate height hh or axial dispersion decreased by a factor of 5 for $K = 0$ and by 2.7 for $K = 5$, compared to the baseline case without lateral flow ($U_l = 0$) (see Fig. 15i). Moreover, they observed that increasing the aspect ratio of the channel reduced the effectiveness of lateral flow in suppressing axial dispersion compared to the AR = 1 condition.

4.2. Polyelectrolyte layer (soft surface) and electrolyte nature

Another approach that can fundamentally influence transport phenomena such as hydrodynamic (Taylor) dispersion of solute species is the introduction of surface soft coatings and the investigation of how the physical properties of both these coatings and the bulk electrolyte solution affect solute transport behavior. Generally, the interaction between an electrolyte solution containing mobile ions and a polyelectrolyte layer (PEL) leads to the formation of a complex structure consisting of flow regions with varying velocities, a nonlinear potential field, and non-uniform concentration profiles, all of which collectively impact solute dispersion.[225,226] While the majority of studies reviewed in the previous sections have focused on hydrodynamic dispersion in rigid-wall micro/nanochannels without surface coatings, many recent investigations have demonstrated that coating the inner walls

of such microfluidic channels with PELs—which are polymers comprising long chains with charged groups—can significantly alter electroosmotic flow, electrostatic potential profiles, hydrodynamic fields, and mass transport behavior.[227–229] These PELs, structured like brushes, typically have thicknesses ranging from nanometers to micrometers, allow ionic exchange with the surrounding electrolyte, and may possess fixed or neutral charge densities. They essentially convert the rigid channel into a semi-permeable soft-wall micro/nanochannel, introducing new pathways for tuning and controlling solute band dispersion.[230–243]

In studies involving soft-coated microchannels, two major modeling strategies are generally adopted. In some investigations, to simplify analytical or numerical efforts under low polymer grafting densities, the physical properties (*e.g.*, dielectric constant, dynamic viscosity, and diffusivity) of the electrolyte and the polyelectrolyte layer are assumed identical, effectively neglecting the ion partitioning effects at the interface. Conversely, in other studies where high grafting densities are considered, the inclusion of ion partitioning—especially due to differences in dielectric constants between the PEL and the bulk electrolyte—has been shown to significantly affect solute dispersion intensity and band broadening, depending on system conditions. These changes may result in either increased or decreased dispersion and thus highlight the importance of accounting for ion partitioning in the design and modeling of soft-coated microfluidic systems. While solute band dispersion in rigid micro- or nanochannels is primarily influenced by geometric features and the thickness of the electrical double layer near charged surfaces, in soft channels, key factors such as PEL thickness, dynamic viscosity, dielectric constant, diffusivity, and surface charge density distribution (which can be uniform, non-uniform, or pH-dependent[244–247]) critically govern dispersion behavior. In a 2016 study, Li *et al.*[232] examined the difference in AC electroosmotic flow and solute dispersion between soft and rigid nanochannels under conditions excluding ion partitioning. By solving the electrostatic potential in the PEL using the linearized Debye–Hückel approximation (valid for small zeta potentials), they derived expressions for the electroosmotic velocity in regions with both uniform and non-uniform drag coefficients. Their results showed that, in soft nanochannels, the amplitude of the AC electroosmotic velocity increased with PEL thickness—leading to more pronounced differences in flow and dispersion behavior compared to rigid channels. In contrast, when the soft layer was thin, both systems exhibited similar characteristics. They also found that the velocity amplitude decreased significantly with increasing oscillatory Reynolds number, thereby limiting dispersion to regions near the PEL–electrolyte interface.

In a 2017 follow-up study, Li *et al.*[248] extended this analysis to viscoelastic non-Newtonian fluids, and later, they incorporated slip boundary conditions. They found that at low oscillatory Reynolds numbers, increasing the slip length and PEL thickness significantly enhanced the effective solute dispersion. Focusing on combined DC electroosmotic and pressure-driven flows with oscillatory fields, Reshadi and Saidi[238] investigated dispersion control of a reactive solute undergoing irreversible catalytic reactions in a capillary with a PEL, considering the ion partitioning effect.

In one of the most comprehensive studies to date (2024), Saha *et al.*[236] presented a hybrid analytical–numerical model for electroosmotic flow and solute band dispersion in a hydrophobic nanochannel with a PEL, incorporating the modified Poisson–Boltzmann, Debye–Bueche, and Stokes equations. This model accounted for ion partitioning, steric effects, and non-uniform monomer and charge distributions (represented as a soft-step function) across the PEL. Their results provided deeper insights into how the interplay of soft interface physics and electrolyte properties can modulate electrokinetic transport and solute dispersion in nanoscale systems.

Practical considerations. The deposition of soft or polyelectrolyte layers (PELs) offers tunable dispersion control but faces fabrication and operational constraints. Multilayer assembly processes are often time-intensive and sensitive to pH, ionic strength, and temperature. In addition, maintaining PEL integrity under flow conditions and ensuring compatibility with biological analytes (*e.g.*, proteins or cells) can limit their long-term use in organ-on-chip or diagnostic devices.

4.3. Flow profile scenarios as driving forces

This section aims to evaluate the extent of hydrodynamic dispersion of solute species and the significant differences in how various velocity profiles impact dispersion, by exploring different flow scenarios—particularly electroosmotic and pressure-driven flows. By "flow scenarios," we refer to diverse types of driving forces, including pressure-driven (Poiseuille) flow, magnetohydrodynamic flow, electroosmotic flow, as well as oscillatory and pulsatile flows. Some of these flow regimes may also be employed in combination under specific conditions to investigate dispersion behavior. Examples include pulsatile electroosmotic flow, electrohydrodynamic flow (a combination of pressure-driven and electroosmotic flow), combined electroosmotic and magnetohydrodynamic flow, and AC electroosmotic flow under alternating electric fields. The choice of driving force is a key factor in manipulating and controlling hydrodynamic dispersion. In fact, as reviewed in earlier sections, most studies have employed various types of driving mechanisms to modulate fluid flow in order to examine solute dispersion, with electroosmotic and pressure-driven flows being the most commonly utilized.

In recent years, dispersion in electrokinetic flows—especially electroosmosis (compared to other electrokinetic effects such as electrophoresis, sedimentation potential, and streaming potential)—has garnered significant attention in microfluidic systems. Among all electrokinetic phenomena, electroosmosis stands out as a highly attractive mechanism for initiating, guiding, and regulating flow in

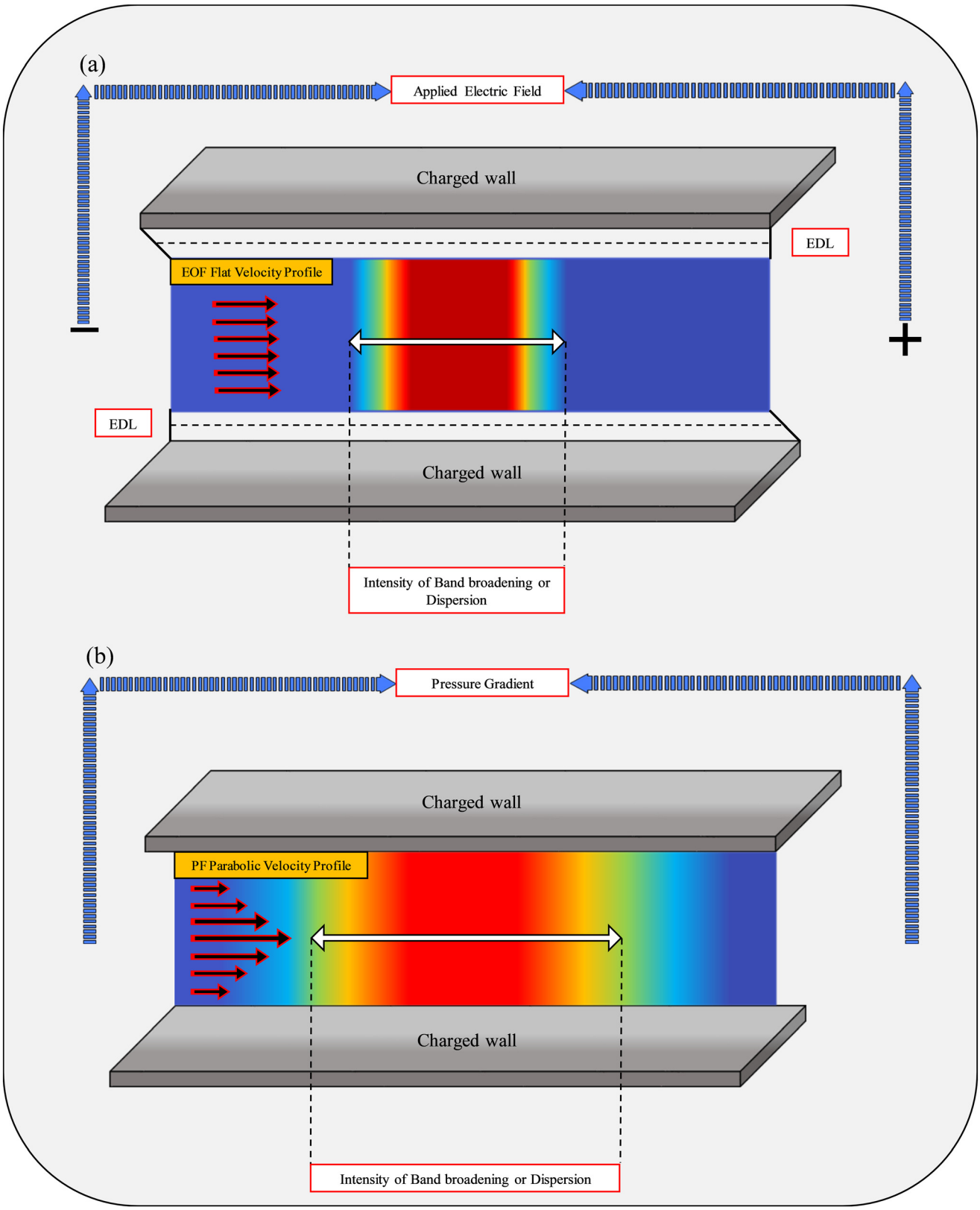

Fig. 16 Comparison of solute band broadening and dispersion under different flow conditions, along with corresponding velocity profiles, for: (a) electroosmotic flow induced by a steady external electric field, and (b) pressure-driven (Poiseuille) flow established by applying a pressure gradient across two charged parallel plates.

microchannels.[249] In over 90% of microfluidic systems, electroosmotic and pressure-driven flows are employed to control fluid motion. Electroosmotic flow refers to the bulk movement of fluid (such as ionic liquids or electrolyte solutions) induced by an externally applied electric field in confined systems—ranging from micro- and nanochannels and nanopores to porous media, membranes, nanostructured surfaces, hydrogels, and biological tissues.[250–252] As illustrated in Fig. 16a (in contrast to the pressure-driven system shown in Fig. 16b), electroosmotic flow is established when an electric field is applied across the microfluidic domain, initiating an interaction between the charged solid walls (*e.g.*, channel or tube surfaces) and the fluid containing ionic or neutral analytes. This interaction leads to the formation of an EDL, consisting of the Stern and diffuse layers, at the interface under no-slip boundary conditions. This ultimately generates an electroosmotic flow as part of the broader electrokinetic phenomena.[253] Once established, the electroosmotic flow exhibits a plug-like velocity profile (*i.e.*, flat and uniform across the channel), driven by the net charge density within the EDL. It is worth noting that the formation of electroosmotic flow is not solely due to the presence of the EDL. In cases where the EDL is extremely thin, the velocity distribution across the shear plane can be described by the Helmholtz–Smoluchowski equation (eqn (9)), which characterizes electroosmotic slip velocity.[254,255]

The key distinction between electroosmotic and pressure-driven (Poiseuille) flow lies in their dependence on channel dimensions and their velocity distributions. As depicted in Fig. 16a and b, EOF offers multiple advantages in microscale systems compared to pressure-driven flow. In pressure-driven flow, the application of a pressure gradient across a microchannel results in a parabolic velocity profile. As channel dimensions decrease, the average flow velocity significantly drops unless the pressure gradient is proportionally increased, scaling with the square of the minimum transverse channel dimension. In contrast, electroosmotic velocity remains independent of channel dimensions when thin EDL conditions are satisfied. Therefore, in miniaturized systems, electric fields become far more effective than pressure gradients in driving fluid flow.[256,257]

Consequently, under thin EDL conditions, the electroosmotic flow adopts a flat, plug-like velocity profile (Fig. 16a), minimizing solute hydrodynamic dispersion due to the absence of velocity gradients across the channel. In this case, dispersion is mainly governed by molecular diffusion alone, particularly at low Péclet numbers. Conversely, pressure-driven flow (Fig. 16b) generates considerable dispersion due to its parabolic velocity profile, where solute molecules at the center move significantly faster than those near the walls. This non-uniformity intensifies with increasing Péclet number, resulting in pronounced band broadening.[258,259] The red and blue regions in Fig. 16a and b correspond to zones of high and low solute concentration, respectively. Notably, the uniform velocity field in Fig. 16a implies that axial dispersion in this case is driven solely by pure diffusion, with no contribution from shear-induced transverse solute migration.

In addition to these differences, electroosmotic flow is particularly advantageous due to its dependence on surface charge properties (surface electric potential and EDL characteristics), its ability to operate without mechanical components (being actuated solely by an applied electric field), and its sensitivity to environmental factors such as fluid conductivity, electrolyte concentration, pH, and temperature.[260–262] These characteristics make electroosmotic flow an ideal candidate for solute transport in microfluidic systems—especially in applications where the ability to suppress and control dispersion is critical. In both pressure-driven and electroosmotic flows, several dimensionless numbers—including the Péclet number, Reynolds number, Schmidt number, and Sherwood number—are essential in describing flow behavior, mass transport, and dispersion dynamics. In microfluidic systems, the Reynolds number is typically less than one, implying that the flow operates in the creeping (Stokes) regime.[263,264] This regime is characterized by viscous-dominated behavior, rather than inertia-driven dynamics.

Practical considerations. Combining multiple control strategies, such as electrokinetic modulation with surface engineering, can yield synergistic dispersion control but also multiplies fabrication complexity. Alignment between patterned electrodes and chemically modified walls requires high-precision microfabrication, and cross-coupling between electric fields and chemical stability must be considered during long-term device operation.

The theoretical and mechanistic discussions in Sections 3 and 4 form a foundation for translating dispersion control into practical microfluidic design. The scaling laws of Taylor–Aris and electrokinetic dispersion directly inform geometry optimization, indicating how channel dimensions, aspect ratios, and curvature can be tuned to tailor longitudinal spreading. Likewise, the surface-related parameters—such as zeta potential, slip length, and interfacial softness—correspond to experimentally controllable variables that can be adjusted through chemical coatings, plasma treatments, or polymer grafting techniques compatible with standard lab-on-a-chip fabrication.[265,266] The non-dimensional expressions for effective dispersion coefficients derived in section 3 provide quantitative metrics that can be integrated into COMSOL-based optimization loops to identify geometry–surface combinations minimizing dispersion prior to fabrication. In this way, the unified framework presented here bridges the gap between theoretical understanding and experimental realization, enabling a rational design cycle for microfluidic devices that couple predictive modeling, simulation, and fabrication toward controlled dispersion performance.[267–269]

The control of dispersion discussed above is central to the functionality of modern lab-on-a-chip and organ-on-chip devices. In microreactors, optimized dispersion ensures uniform reactant distribution and predictable residence times, improving yield and selectivity. In electrophoretic and

Table 4 Summary and comparison of studies conducted to control the hydrodynamic dispersion in microfluidic systems

Flow profile	Fluid/solute	Channel geometry	Dimensionless number or parameters	Research topic	Type of study	DH app.	Ref
PDF	Electrolyte solution containing neutral solute	Rectangular, elliptical, isotropic etched, trapezoidal	Peclet number	Investigation of effects of different geometries, sidewall effects, and microchannel bending on solute dispersion in microfluidic systems	Numerical/analytical	No	85
PDF	Electrolyte solution	Parallel flat plates	Different slip length, zeta potential	Examination of effects of zeta potential non-uniformity and different wall slip lengths on Taylor dispersion	Numerical/analytical	No	61
EOF + PDF	Non-reactive neutral solute	Coupled system including capillary tube and porous medium	Peclet number, Poiseuille flow fraction, Debye–Höckel electrokinetic parameter	Investigation and study of effects of Debye–Höckel parameter and Poiseuille flow fraction on shear dispersion for neutral solute transport	Analytical	No	270
EOF + MHD	Newtonian fluid	Parallel flat plates	Hartman number & ratio of half microchannel height to Debye length	Effect of channel wall zeta potential variations and magnetic field presence on axial hydrodynamic dispersion	Analytical	Yes	76
EOF	Viscoelastic fluid containing neutral solute	Slit microchannel	Peclet number, relative thickness parameter of electric double layer & fluid elasticity	Evaluation of fluid elasticity effects (elasticity or fluid resilience capability) on Taylor dispersion	Numerical/analytical	Yes	98
PDF	Single-phase, incompressible fluid with constant physical properties	Coupled system including porous matrix structure and slit with rough wall	Peclet number & relative roughness parameter	Assessment of the effect of different slit geometries of a rough wall in terms of relative roughness degree on Taylor dispersion	Analytical	No	99
EOF	Electrolyte solution	Microchannel with slit containing soft layer	Peclet number, PEL friction, zeta potential	Evaluation of effects of properties and characteristics of polyelectrolyte layer on dispersion rate under conditions of ignoring ion partitioning effect and uniform channel wall potential	Numerical/analytical	Yes	106
PEOF	Dilute neutral solute electrolyte solution	Parallel flat plates	Schmidt number, angular Reynolds number, and ratio of half microchannel height to Debye length	Effect of channel wall zeta potential asymmetry on dispersion and mass transfer rate	Analytical	Yes	184
EOF + PDF	Single-phase, incompressible fluid with constant physical properties	Microchannel with porous and non-porous walls	Peclet number & bluntness parameter	Investigation of mass transfer under laminar flow conditions and dispersion in various flow profile scenarios	Numerical/analytical	No	50
Pulsating	Non-active solute (non-participating actively in fluid flow)	Annular cavity	Cavity geometry, temporal frequency, and pressure force wavelength	Investigation of distribution and Taylor dispersion of drug and biological molecules in subarachnoid space (vital region filled with cerebrospinal fluid) and its impact on neural processes in central nervous system	Numerical/analytical	No	38
EOF	Newtonian fluid	Rectangular microchannel with polyelectrolyte coating	Peclet number, Damköhler number & charge density	Investigation of unsteady solute dispersion under surface absorption conditions of walls and fully developed flow	Numerical/analytical	Yes	120
EOF	Electrolyte solution	Slit microchannel containing non-porous PEL	Peclet number, diffusion coefficient, permittivity and viscosity of soft layer and the electrolyte solution	Effects of physical properties of PEL and electrolyte solution on solute hydrodynamic dispersion rate	Numerical/analytical	Yes	105

Table 4 *(continued)*

Flow profile	Fluid/solute	Channel geometry	Dimensionless number or parameters	Research topic	Type of study	DH app.	Ref
EOF	Viscoelastic fluids	Parallel flat plates	Hartman number, electric field strength parameter, zeta potential ratio of channel walls, slip coefficients	Investigation of magnetic field effects on electroosmotic flow velocity profile for viscoelastic fluid and Taylor dispersion	Numerical/analytical	Yes	54
PDF	Brownian tracer solute particles	Parallel flat plates	Peclet number, particle size ratio, rotational diffusion and rotational convection	Hydrodynamic dispersion of elongated, narrow and non-spherical particles (nanorods, cells, and polymers) in fluid flow	Numerical/analytical	No	37
PDF	Blood flow	Cylindrical channel (blood vessels)	Peclet number, Darcy number, Forchheimer number	Taylor dispersion in non-Darcy porous medium with chemical reaction (model presentation for drug transport process in blood vessels with deposits or blockages)	Analytical	No	122
EOF	Non-Newtonian viscoplastic fluid	Parallel flat plates	Debye–Höckel electrokinetic parameter & stress	Investigation of transient solute dispersion in viscoplastic fluid flow	Analytical	Yes	14
Forced and free convection	—	Parallel flat plates	Peclet number, grash of number, and wall boundary absorption parameters	Solute dispersion phenomenon inside a channel with boundary absorption and bulk reactions	Analytical	No	47
PEOF	Non-Newtonian fluid (Carreau fluid)	Circular channel	Peclet number, pulsatile Reynolds number, and Weissenberg number	Understanding dispersion phenomenon and drug transport (reactive solutes) in blood flow and development of artificial tools in biomedical engineering fields	Numerical/analytical	Yes	271
PDF + EOF	Incompressible Newtonian fluid	Micro-tube with porous and sinusoidal wavy wall	Peclet number, Schmidt number, Reynolds number, Sherwood number	Rough and porous channel wall effects on mass transfer or neutral solute transport in microfluidic systems	Numerical/analytical	Yes	196
PEOF + MHD	Incompressible Newtonian fluid	Parallel flat plates	External electric field strength, wall zeta potential ratio, slip coefficients, Hartmann number, and Peclet number	Investigation and understanding of how to control solute species dispersion in combined PEOF + MHD flow for improving design and optimization of microfluidic systems used in targeted drug delivery systems and lab-on-chip	Numerical/analytical	Yes	187
PDF	Magnetic nanoparticles (Ferrofluid)	Capillary tube	Peclet number, dimensionless mixing factor, Reynolds number, and residence time distribution	Investigation of rotating flow effects (creating tangential flow) resulting from rotating magnetic field on mixing efficiency and Taylor dispersion reduction in a capillary tube containing ferrofluid	Numerical/analytical	No	107
AC EOF	Newtonian, incompressible, monovalent electrolyte solution containing a neutral solute	Micro-tube with porous wall	Sherwood number, Schmidt number, Reynolds number, and frequency	AC electric field effects on neutral solute mass transfer & dispersion behavior (study for better understanding of drug delivery through microfluidic channels and nutrient transport in physiological systems)	Analytical	Yes	53

Table 4 *(continued)*

Flow profile	Fluid/solute	Channel geometry	Dimensionless number or parameters	Research topic	Type of study	DH app.	Ref
PDF	Incompressible viscous fluid	Rotating microchannel confined by two parallel plates	Peclet number, rotation parameter, and absorption parameter	Investigation of solute transport in primary and secondary flow through a rotating channel with wall boundary surface absorption conditions (creating comprehensive view of solute dispersion under rotating flow conditions and boundary absorption of solute molecules and their effects on average and vertical concentration distribution)	Analytical	No	202

biosensing platforms, suppression of axial broadening enhances analyte resolution and detection accuracy. Conversely, controlled dispersion can be deliberately exploited for micromixing, analyte focusing, and biofluid homogenization. The same physical principles now inform emerging AI-assisted and hybrid channel designs, where predictive models couple geometric and electrokinetic tuning to achieve target dispersion characteristics. These applications collectively demonstrate how the theoretical control strategies reviewed here translate directly into measurable improvements in device-level performance across diverse microfluidic technologies (Table 4).

5. Summary and outlook

Looking forward, the unified framework presented here provides a foundation for incorporating new physical and computational paradigms into dispersion analysis. The integration of data-driven optimization, multi-field coupling, and bioinspired microenvironments presents both challenges and opportunities to reimagine dispersion control in intelligent microfluidic systems. By synthesizing classical theory with these emerging domains, this review highlights the evolving significance of hydrodynamic dispersion in contemporary lab-on-a-chip research. The phenomenon of hydrodynamic (Taylor–Aris) dispersion remains one of the most critical challenges and concurrently promising opportunities in the design and optimization of microfluidic systems. In this review, we have provided a comprehensive, structured, and critical examination of the governing mechanisms, historical evolution, and state-of-the-art strategies for understanding and controlling solute dispersion in micro- and nanofluidic environments. By unifying diverse approaches across analytical, numerical, and experimental domains, the manuscript articulates a cohesive framework for how shear-induced advection and radial molecular diffusion coalesce to define the longitudinal spreading of solutes under various flow regimes.

The current work is unique in its breadth and analytical depth. It transcends the classical scope of Taylor dispersion by systematically incorporating effects stemming from geometric asymmetries, surface physicochemical heterogeneities, external fields (electroosmotic, magnetic, and acoustic), and soft interface modifications. Specifically, we explored three major axes of dispersion control: (i) modulation of channel geometry and flow profiles, (ii) engineering of soft, polyelectrolyte-coated walls, and (iii) implementation of secondary flows and dynamic field-driven perturbations. Each axis not only offers distinct mechanistic pathways for minimizing undesirable band broadening but also introduces nuanced control over local hydrodynamics and electrokinetics within confined domains.

Of particular note is the in-depth treatment of soft-wall micro/nanochannels bearing polyelectrolyte layers (PELs), which embody a paradigm shift in dispersion science. These surface-engineered interfaces—featuring variable thickness, ionic permeability, pH-sensitivity, and spatially heterogeneous charge densities—significantly alter the interplay between electric double layers, fluid flow, and solute migration. Moreover, accounting for ion-partitioning phenomena and differences in physicochemical properties between the PEL and the bulk electrolyte allows for the predictive design of solute transport and dispersion, even under complex reaction–diffusion–electrokinetic scenarios.

Our investigation also revealed the transformative potential of dynamic, time-dependent secondary flows—such as pulsatile electroosmotic, acoustic streaming, and alternating current electroosmosis—in enhancing mixing or suppressing axial dispersion. These methods challenge the long-held belief that dispersion is an inevitable byproduct of laminar flow and instead offer compelling routes for active flow field engineering.

From an application standpoint, the insights garnered here have far-reaching implications for next-generation microfluidic systems including lab-on-a-chip diagnostics, high-resolution microchromatography, biosensing, microreactor design, drug delivery platforms, energy conversion modules, and nanofluidic separation technologies. In all of these, the ability to suppress or harness dispersion directly translates to enhanced

analytical resolution, throughput, and control over reaction environments.

Despite significant progress, several critical challenges and research gaps persist:

- Multiphysics coupling: fully integrated models that couple electrokinetics, thermodynamics, and interfacial chemistry in soft-walled, dynamically modulated microchannels remain sparse.
- Experimental validation: many theoretical and numerical predictions—especially concerning ion partitioning, field-induced anisotropies, and reactive dispersion—lack systematic experimental confirmation due to fabrication and measurement complexities at the nanoscale.
- Non-classical transport regimes: with the advent of ultra-narrow, porous, and deformable channels, the assumptions of classical Taylor–Aris theory may no longer hold. This necessitates the development of extended or hybrid theories incorporating steric, surface conduction, and nano-confinement effects.
- Scalability and integration: bridging the gap between single-channel investigations and real-world, multichannel or multiplexed systems suitable for commercial deployment remains a formidable challenge.

Looking forward, the evolution of this field will likely be shaped by a synergistic blend of advanced simulation (*e.g.*, COMSOL multiphysics, machine-learning-assisted modeling), high-resolution *in situ* diagnostics (such as micro-PIV, electrochemical imaging, and fluorescence correlation spectroscopy), and micro/nanofabrication breakthroughs (*e.g.*, 3D printing, soft lithography, and surface patterning). These tools will be critical in unraveling the full complexity of dispersion phenomena and converting theoretical advances into deployable technologies.

Beyond its theoretical significance, the control of hydrodynamic dispersion plays a pivotal role in the performance of advanced microfluidic platforms. In organ-on-chip systems, minimizing axial dispersion preserves concentration gradients essential for physiological mimicry and tissue viability. In point-of-care diagnostic devices and biosensors, dispersion suppression enhances detection precision and temporal resolution by stabilizing analyte bands. Likewise, in drug delivery microdevices, controlling Taylor dispersion enables accurate dosage release and spatiotemporal targeting in vascular and neural microenvironments. Finally, in microscale energy systems such as microfluidic fuel cells and catalytic microreactors, optimized dispersion improves reactant utilization and conversion efficiency. Collectively, these interdisciplinary applications underscore that dispersion management constitutes not only a fundamental transport phenomenon but also a practical design principle governing the performance of next-generation lab-on-a-chip technologies.

Looking ahead, several promising research avenues are poised to reshape the understanding and control of hydrodynamic dispersion in next-generation microfluidic systems. First, machine-learning-assisted inverse design frameworks can enable predictive optimization of channel geometry, surface charge patterning, and actuation fields, significantly accelerating the discovery of dispersion-minimizing architectures. Second, the integration of smart or stimuli-responsive materials offers new opportunities for real-time, adaptive modulation of flow profiles and solute distribution, providing dynamic control capabilities far beyond static channel designs. Third, exploring coupled electro-hydrodynamic and nanoconfinement effects at soft and biofunctional interfaces represents a fertile ground for innovation, particularly in organ-on-chip, biosensing, and drug delivery platforms. Collectively, these directions bridge classical Taylor–Aris theory with emerging intelligent, adaptive, and bioinspired microfluidic paradigms, setting the stage for transformative developments in precision transport and microscale diagnostics.

In conclusion, this review not only consolidates the current understanding of hydrodynamic dispersion in microfluidics but also charts a forward-looking roadmap for researchers and engineers. By systematically dissecting and reconstructing the mechanisms, control strategies, and applications of dispersion, it aspires to catalyze innovation across disciplines—ranging from chemical engineering and materials science to bioanalytical chemistry and soft matter physics.

Abbreviations

AFM	Atomic force microscopy
AR	Aspect ratio
AD	Axial diffusion
AC	Alternating current
AUC	Analytical ultracentrifugation
ASMF	Axial stationary magnetic field
CE	Capillary electrophoresis
DC	Direct current
DLS	Dynamic light scattering
EOF	Electroosmotic flow
EMHD	Electro-magneto-hydrodynamic
EDL	Electrical double layer
FFF	Field flow fractionation
FCS	Fluorescence correlation spectroscopy
GTDT	Generalized Taylor dispersion theory
HD	Hydrodynamic dispersion
HETP	Height equivalent of a theoretical plate
HS	Helmholtz–Smoluchowski
LOC/LOD	Lab on a chip/disk
LBM	Lattice Boltzmann method
LPM	Longitudinally patterned micro column or tube
LAT	Lubrication approximation theory
MEMS	Micro electro-mechanical systems
NMR	Nuclear magnetic resonance
NTA	Nanoparticle tracking analysis
OMHD	Oscillating magnetohydrodynamic
PDF	Pressure driven (Poiseuille) flow
PEOF	Pulsating electroosmotic flow

PFF	Pinched flow fractionation
PEL	Polyelectrolyte layer
RTD	Residence time distribution
RD	Radial diffusion
SCDSL	Surface charge dependent slip length
SCISL	Surface charge independent slip length
SEM	Scanning electron microscopy
SEC	Size exclusion chromatography
TPM	Transversely patterned micro column or tube
TRMF	Transverse rotating magnetic field
TOMF	Transverse oscillating magnetic field
TEM	Transmission electron microscopy
TDA	Taylor dispersion analysis
μTAS	Micro total analysis system
Cu	Carreau number [–]
D_m, D	Analyte band molecular diffusion coefficient [m^2 s^{-1}]
D_{ax}	Axial dispersion coefficient [m^2 s^{-1}]
D_{TH}	Taylor hydrodynamic dispersion coefficient [m^2 s^{-1}]
d, H	Channel height depth [μm]
Da	Damköhler number [–]
E	Electric field [V m^{-1}]
f_v	Flow velocity profile factor [–]
f_g	Constant geometry factor [–]
f_σ	Stationary surface roughness factor [–]
Ha	Hartman number [–]
H_0	Rotating magnetic field intensity [kA m^{-1}]
h	Reduced plate height [–]
j_e	Applied external current density [A m^{-2}]
j	Current density [A m^{-2}]
K_{eff}, D_{eff}	Taylor–Aris effective dispersion coefficient [m^2 s^{-1}]
k_a	Adsorption wall reaction rate [mol m^{-2} s^{-1}]
k_d	Desorption rate [mol m^{-2} s^{-1}]
k_{BR}	Bulk chemical reaction rate [mol m^{-2} s^{-1}]
K	Retention factor [–]
L	Axial channel characteristic length [m]
m	Bluntness parameter [–]
n	Non-Newtonian fluid flow behavior index [–]
p	Hydrodynamic pressure [Pa]
Pe, N_{Pe}	Peclet number [–]
$Q_{j,v}$	Volume flow [m^3 s^{-1}]
R	Radius of the channel or capillary tube [μm or nm]
r	Radial coordinates [m]
Re	Reynolds number [–]
R_r	Ratio of internal to external curvature radius parameter [–]
Re_w	Dimensionless angular Reynolds number [–]
Sc	Schmidt number [–]
U_R	Recirculation zones velocity [m s^{-1}]
U	Average linear fluid velocity [m s^{-1}]
U_l	Average lateral flow velocity [m s^{-1}]
$u_{EOF\text{-}HS}$	Helmholtz–Smoluchowski electroosmotic velocity [m s^{-1}]
w	Channel width [μm]
We	Weissenberg number [–]
x	Axial coordinates [m]
α	Couple stress parameter [–]
Δx	The longitudinal distance separating two axial positions from each other [m]
$\Delta {\sigma_x}^2$	The amount of increase in the width of the analyte band concentration distribution [m^2]
λ	Slip length [m]ξ
ξ	Amplitude of the oscillatory electric field [V m^{-1}]
ρ_e	Volume charge density of ions in an electrolyte solution [C m^{-3}]
σ	Solute species electrical conductivity [S m^{-1}]
τ_h	Hydraulic tortuosity [–]
τ_s	Surface tortuosity [–]
ϕ, V_{app}	Applied electrostatic potential [mV, V]
ψ	Dimensionless mixing factor [–]
δ	Deviation or bending degree parameter [–]
ε	Permittivity constant [F m^{-1}]
ε_R	Relative roughness [–]
ζ	Surface zeta potential [mV, V]
η_D	Ratio of diffusion coefficient in PEL to electrolyte solution [–]
η_μ	Ratio of dynamic viscosity in PEL to dynamic viscosity of electrolyte solution [–]
κ, λ_D	Debye electrokinetic length parameter [m]
Λ	Relaxation time [s]

Conflicts of interest

The authors declare no conflict of interest.

Data availability

The data that support the findings of this study are available from the corresponding author upon reasonable request.

Acknowledgements

The research council at Iran University of Science and Technology (IUST) and Iran National Science Foundation (INSF) are highly appreciated for their support during the course of this research.

References

1 L. Chen, C. Yang, Y. Xiao, X. Yan, L. Hu, M. Eggersdorfer, D. Chen, D. A. Weitz and F. Ye, *Mater. Today Nano*, 2021, **16**, 100136.
2 T. Kong, H. C. Shum and D. A. Weitz, *Small*, 2020, **16**, 2000070.
3 M. Tokeshi, *Applications of microfluidic systems in biology and medicine*, Springer, 2019.
4 C.-C. Cho, C.-L. Chen and C. o.-K. Chen, *Int. J. Therm. Sci.*, 2012, **61**, 94–105.
5 V. Kordzadeh-Kermani, M. Madadelahi, S. N. Ashrafizadeh, L. Kulinsky, S. Martinez-Chapa and M. Madou, *Biosens. Bioelectron.*, 2022, **214**, 114381.

6 E. K. Sackmann, A. L. Fulton and D. J. Beebe, *Nature*, 2014, **507**, 181–189.
7 J. Zhang, S. Yan, D. Yuan, G. Alici, N.-T. Nguyen, M. E. Warkiani and W. Li, *Lab Chip*, 2016, **16**, 10–34.
8 S. Ayoubi, M. Khatibi and S. N. Ashrafizadeh, *Microfluid. Nanofluid.*, 2021, **25**, 101.
9 J. Lee, M. Lee, E. Kulla and A. Tripathi, *Int. J. Heat Mass Transfer*, 2017, **104**, 813–818.
10 S. Yuan, M. Zhou, X. Liu and B. Jiang, *Int. J. Heat Mass Transfer*, 2023, **206**, 123925.
11 N. Convery and N. Gadegaard, *Micro Nano Eng.*, 2019, **2**, 76–91.
12 E. Noviana, T. Ozer, C. S. Carrell, J. S. Link, C. McMahon, I. Jang and C. S. Henry, *Chem. Rev.*, 2021, **121**, 11835–11885.
13 Y. Guan, T. Yang and J. Wu, *Phys. Fluids*, 2021, **33**, 042006.
14 A. K. Roy, S. Debnath and O. A. Bég, *Z. Angew. Math. Mech.*, 2023, **103**, e202200260.
15 D. Yang, J. S. Lee, C.-K. Choi, H.-P. Lee, S.-W. Cho and W. Ryu, *Acta Biomater.*, 2018, **68**, 249–260.
16 M. W. Dewhirst and T. W. Secomb, *Nat. Rev. Cancer*, 2017, **17**, 738–750.
17 M. Ferreira, V. Carvalho, J. Ribeiro, R. A. Lima, S. Teixeira and D. Pinho, *Micromachines*, 2024, **15**, 873.
18 Y.-Q. Fan, H.-L. Wang, K.-X. Gao, J.-J. Liu, D.-P. Chai and Y.-J. Zhang, *Chin. J. Anal. Chem.*, 2018, **46**, 1863–1871.
19 M. Khatibi, S. N. Ashrafizadeh and A. Sadeghi, *Anal. Chim. Acta*, 2020, **1122**, 48–60.
20 D. Wu, J. Qin and B. Lin, *J. Chromatogr. A*, 2008, **1184**, 542–559.
21 S. Jafari, M. Khatibi and S. N. Ashrafizadeh, *Electrochim. Acta*, 2024, **507**, 145186.
22 M. Khatibi, H. Dartoomi and S. N. Ashrafizadeh, *Langmuir*, 2023, **39**, 13717–13734.
23 M. Khatibi, S. N. Ashrafizadeh and A. Sadeghi, *Electrochim. Acta*, 2021, **395**, 139221.
24 M. Khatibi, A. Sadeghi and S. N. Ashrafizadeh, *Phys. Chem. Chem. Phys.*, 2021, **23**, 2211–2221.
25 H. Fallahi, J. Zhang, H.-P. Phan and N.-T. Nguyen, *Micromachines*, 2019, **10**, 830.
26 M. Zare, M. Khatibi and S. N. Ashrafizadeh, *Phys. Fluids*, 2025, **37**, 022006.
27 A. Aminnia, M. Khatibi and S. Nezameddin Ashrafizadeh, *Sep. Purif. Technol.*, 2023, **325**, 124698.
28 A. Aryasomayajula, P. Bayat, P. Rezai and P. R. Selvaganapathy, in *Springer Handbook of Nanotechnology*, ed. B. Bhushan, Springer Berlin Heidelberg, Berlin, Heidelberg, 2017, pp. 487–536.
29 S. N. Ashrafizadeh, M. Zare and M. Khatibi, *Chem. Eng. Process.*, 2025, **208**, 110087.
30 M. K. D. Manshadi, M. Mohammadi, M. Zarei, M. Saadat and A. Sanati-Nezhad, *J. Micromech. Microeng.*, 2020, **30**, 113001.
31 A. Heydari, M. Khatibi and S. N. Ashrafizadeh, *Phys. Chem. Chem. Phys.*, 2023, **25**, 26716–26736.
32 I. Llorente, S. Fajardo and J. M. Bastidas, *J. Solid State Electrochem.*, 2014, **18**, 293–307.
33 S. Wall, *Curr. Opin. Colloid Interface Sci.*, 2010, **15**, 119–124.
34 Y. Sun, R. Jiang, L. Hu, Y. Song and M. Li, *Electrophoresis*, 2023, **44**(23), 1756–1773.
35 C. Zhao and C. Yang, *Adv. Colloid Interface Sci.*, 2013, **201–202**, 94–108.
36 S. Balog, D. A. Urban, A. M. Milosevic, F. Crippa, B. Rothen-Rutishauser and A. Petri-Fink, *J. Nanopart. Res.*, 2017, **19**, 287.
37 A. H. Kumar, S. J. Thomson, T. R. Powers and D. M. Harris, *Phys. Rev. Fluids*, 2021, **6**, 094501.
38 L. Salerno, G. Cardillo and C. Camporeale, *Phys. Rev. Fluids*, 2020, **5**, 043102.
39 Z. Wu and A. Singh, *J. Hydrol.*, 2018, **566**, 607–615.
40 M. Dejam and H. Hassanzadeh, *AIChE J.*, 2023, **69**, e17928.
41 S. Marbach and K. Alim, *Phys. Rev. Fluids*, 2019, **4**, 114202.
42 B. Mahapatra, R. Jana and A. Bandopadhyay, *Phys. Fluids*, 2024, **36**, 022017.
43 S. K. Bhaumik, A. Kannan and S. DasGupta, *Chem. Eng. Sci.*, 2015, **134**, 251–259.
44 J. H. Masliyah and S. Bhattacharjee, *Electrokinetic and Colloid Transport Phenomena*, Wiley, 2006.
45 G. I. Taylor, *Proc. R. Soc. London, Ser. A*, 1953, **219**, 186–203.
46 R. Aris, *Proc. R. Soc. London, Ser. A*, 1956, **235**, 67–77.
47 G. Saha, N. Poddar, S. Dhar, B. S. Mazumder and K. K. Mondal, *European Journal of Mechanics - B/Fluids*, 2023, **100**, 101–123.
48 R. E. Migacz and J. T. Ault, *Phys. Rev. Fluids*, 2022, **7**, 034202.
49 A. Khodabandehloo and D. D. Y. Chen, *Anal. Chem.*, 2017, **89**, 7823–7827.
50 M. Dejam, *Int. J. Heat Mass Transfer*, 2019, **136**, 87–98.
51 M. Aminian, F. Bernardi, R. Camassa, D. M. Harris and R. M. McLaughlin, *Science*, 2016, **354**, 1252–1256.
52 M. Dejam, *Chem. Eng. Sci.*, 2019, **204**, 298–309.
53 A. Kumar and S. De, *Chem. Eng. Sci.*, 2024, **288**, 119832.
54 X. Wang, Y. Qiao, H. Qi and H. Xu, *Electrophoresis*, 2021, **42**, 2347–2355.
55 S. Das and K. K. Mondal, *Phys. Fluids*, 2024, **36**, 053602.
56 S. Huang, S. Debnath, A. K. Roy, J. Wang, W. Jiang, O. A. Bég and S. Kuharat, *Phys. Fluids*, 2024, **36**, 052011.
57 E. K. Zholkovskij, J. H. Masliyah and A. E. Yaroshchuk, *Microfluid. Nanofluid.*, 2013, **15**, 35–47.
58 N. Poddar, D. Das, S. Dhar and K. K. Mondal, *Phys. Fluids*, 2023, **35**, 043617.
59 A. E. Herr, J. I. Molho, J. G. Santiago, M. G. Mungal, T. W. Kenny and M. G. Garguilo, *Anal. Chem.*, 2000, **72**, 1053–1057.
60 S. Chowdhury, S. K. Pal and P. P. Gopmandal, *Soft Matter*, 2025, **21**, 1085–1112.
61 C.-O. Ng, *Microfluid. Nanofluid.*, 2011, **10**, 47–57.
62 Z. Seifollahi, M. Khatibi and S. N. Ashrafizadeh, *Ind. Eng. Chem. Res.*, 2024, **63**, 10812–10824.
63 P. Gelin, D. Maes and W. De Malsche, *Chem. Eng. J.*, 2021, **417**, 128031.
64 M. Dejam, *Chem. Eng. Res. Des.*, 2019, **150**, 169–178.

65 A. Marion and M. Zaramella, *J. Hydraul. Eng.*, 2006, **132**, 1295–1302.
66 S. Shaw, S. Ganguly, P. Sibanda and S. Chakraborty, *Microvasc. Res.*, 2014, **92**, 25–33.
67 S. Datta and S. Ghosal, *Lab Chip*, 2009, **9**, 2537–2550.
68 C.-C. Cho, C.-J. Ho and C. o.-K. Chen, *Chem. Eng. J.*, 2010, **163**, 180–187.
69 M. Dejam and H. Hassanzadeh, *Phys. Fluids*, 2021, **33**, 116602.
70 M. Dejam, H. Hassanzadeh and Z. Chen, *AIChE J.*, 2015, **61**, 3981–3995.
71 L. R. Mashiku and S. Shaw, *Phys. Fluids*, 2023, **35**, 101909.
72 M. R. Moser and C. A. Baker, *Anal. Methods*, 2021, **13**, 2357–2373.
73 S. M. Saravanakumar and P.-V. Cicek, *Micromachines*, 2023, **14**, 1827.
74 A. Gubbiotti, M. Baldelli, G. Di Muccio, P. Malgaretti, S. Marbach and M. Chinappi, *Adv. Phys.: X*, 2022, **7**, 2036638.
75 N. M. Sanchez-Ballester, F. Sciortino, S. H. Mir and G. Rydzek, *Molecules*, 2022, **27**, 3263.
76 C. Vargas, J. Arcos, O. Bautista and F. Mendez, *Phys. Fluids*, 2017, **29**, 092002.
77 C.-O. Ng and Q. Zhou, *Phys. Fluids*, 2012, **24**, 112002.
78 S. Pennathur, *Lab Chip*, 2008, **8**, 383–387.
79 D. Dutta, in *Encyclopedia of Microfluidics and Nanofluidics*, ed. D. Li, Springer US, Boston, MA, 2013, pp. 1–14.
80 W. N. Gill, R. Sankarasubramanian and G. I. Taylor, *Proc. R. Soc. London, Ser. A*, 1970, **316**, 341–350.
81 W. N. N. Gill, R. Sankarasubramanian and G. I. Taylor, *Proc. R. Soc. London, Ser. A*, 1971, **322**, 101–117.
82 E. J. Watson, *J. Fluid Mech.*, 1983, **133**, 233–244.
83 H.-F. Huang and C.-L. Lai, *Proc. R. Soc. A*, 2006, **462**, 2017–2038.
84 G. Ramon, Y. Agnon and C. Dosoretz, *Microfluid. Nanofluid.*, 2011, **10**, 97–106.
85 S. Barik and D. C. Dalal, *Proc. R. Soc. A*, 2019, **475**, 20180483.
86 N. Poddar, G. Saha, K. K. Mondal, S. Dhar and B. S. Mazumder, *Phys. Fluids*, 2024, **36**, 053601.
87 D. Murugan, A. K. Roy, R. Ponalagusamy and O. A. Bég, *Int. J. Appl. Comput. Math.*, 2022, **8**, 221.
88 D. Das, S. Shaw, K. K. Mondal and R. R. Kairi, *Eur. Phys. J. Plus*, 2023, **138**, 372.
89 C.-O. Ng, *Proc. R. Soc. A*, 2005, **462**, 481–515.
90 I. Frankel and H. Brenner, *J. Fluid Mech.*, 1989, **204**, 97–119.
91 S. K. Griffiths and R. H. Nilson, *Anal. Chem.*, 2000, **72**, 4767–4777.
92 E. K. Zholkovskij, J. H. Masliyah and J. Czarnecki, *Anal. Chem.*, 2003, **75**, 901–909.
93 E. K. Zholkovskij and J. H. Masliyah, *Anal. Chem.*, 2004, **76**, 2708–2718.
94 D. Dutta, A. Ramachandran and D. T. Leighton, *Microfluid. Nanofluid.*, 2006, **2**, 275–290.
95 H. Zhao and H. H. Bau, *Anal. Chem.*, 2007, **79**, 7792–7798.
96 A. Adrover, *Phys. Fluids*, 2013, **25**, 093601.
97 E. K. Zholkovskij, A. E. Yaroshchuk, J. H. Masliyah and J. d. P. Ribas, *Colloids Surf., A*, 2010, **354**, 338–346.
98 V. Hoshyargar, M. Talebi, S. N. Ashrafizadeh and A. Sadeghi, *Microfluid. Nanofluid.*, 2017, **22**, 4.
99 M. Dejam, H. Hassanzadeh and Z. Chen, *SPE J.*, 2018, **23**, 1669–1688.
100 D. A. Urban, A. M. Milosevic, D. Bossert, F. Crippa, T. L. Moore, C. Geers, S. Balog, B. Rothen-Rutishauser and A. Petri-Fink, *Colloid Interface Sci. Commun.*, 2018, **22**, 29–33.
101 A. Adrover, S. Cerbelli and M. Giona, *Phys. Fluids*, 2018, **30**, 042002.
102 C. Amatore, O. V. Klymenko, A. I. Oleinick and I. Svir, *Anal. Chem.*, 2009, **81**, 7667–7676.
103 T. Y. Lin and E. S. G. Shaqfeh, *Phys. Rev. Fluids*, 2019, **4**, 034501.
104 F. Li and Y. Jian, *Int. J. Heat Mass Transfer*, 2019, **141**, 1066–1077.
105 R. Talebi, S. N. Ashrafizadeh and A. Sadeghi, *Chem. Eng. Sci.*, 2021, **229**, 116058.
106 V. Hoshyargar, A. Khorami, S. N. Ashrafizadeh and A. Sadeghi, *Sens. Actuators, B*, 2018, **255**, 3585–3600.
107 Z. Larbi, F. Larachi and A. Azzi, *Chem. Eng. J.*, 2024, **493**, 152528.
108 I. Bihi, P. Gelin, I. Frankel and W. De Malsche, *J. Chromatogr. A*, 2024, **1736**, 465370.
109 B. M. Alessio, S. Shim, A. Gupta and H. A. Stone, *J. Fluid Mech.*, 2022, **942**, A23.
110 M. T. Kreutzer, A. Günther and K. F. Jensen, *Anal. Chem.*, 2008, **80**, 1558–1567.
111 M. H. Oddy, J. G. Santiago and J. C. Mikkelsen, *Anal. Chem.*, 2001, **73**, 5822–5832.
112 S. Ghosal, *Annu. Rev. Fluid Mech.*, 2006, **38**, 309–338.
113 Z. Wu and N.-T. Nguyen, *Microfluid. Nanofluid.*, 2005, **1**, 208–217.
114 H. A. Stone, A. D. Stroock and A. Ajdari, *Annu. Rev. Fluid Mech.*, 2004, **36**, 381–411.
115 M. Guan and G. Chen, *J. Fluid Mech.*, 2024, **980**, A33.
116 E.-C. Ani, S. Wallis, A. Kraslawski and P. S. Agachi, *Environ. Model. Softw.*, 2009, **24**, 1139–1152.
117 B. Wang, W. Jiang and G. Chen, *J. Fluid Mech.*, 2023, **962**, A39.
118 M. Dejam and H. Hassanzadeh, *Phys. Fluids*, 2024, **36**, 092001.
119 Z. Peng and J. F. Brady, *Phys. Rev. Fluids*, 2020, **5**, 073102.
120 M. Sadeghi, M. H. Saidi, A. Moosavi and A. Sadeghi, *J. Fluid Mech.*, 2020, **887**, A13.
121 R. F. Probstein, *Physicochemical Hydrodynamics: An Introduction*, Wiley, 2005.
122 A. K. Roy, O. A. Bég, A. K. Saha and J. V. R. Murthy, *J. Eng. Math.*, 2021, **127**, 24.
123 C.-O. Ng and B. Chen, *J. Fluids Eng.*, 2013, **135**, 101203.
124 Z. Wu and G. Q. Chen, *Int. J. Heat Mass Transfer*, 2015, **84**, 571–577.
125 J. Teng, B. Rallabandi and J. T. Ault, *J. Fluid Mech.*, 2023, **977**, A5.

126 N.-T. Nguyen, *Micromixers: fundamentals, design and fabrication*, William Andrew, 2011.
127 J. Chamieh and H. Cottet, in *Colloid and Interface Science in Pharmaceutical Research and Development*, ed. H. Ohshima and K. Makino, Elsevier, Amsterdam, 2014, pp. 173–192.
128 J. Chamieh, L. Leclercq, M. Martin, S. Slaoui, H. Jensen, J. Østergaard and H. Cottet, *Anal. Chem.*, 2017, **89**, 13487–13493.
129 S. Latunde-Dada, R. Bott, J. Crozier, M. Trikeriotis, O. I. Leszczyszyn and D. Goodall, *J. Chromatogr. A*, 2016, **1472**, 66–73.
130 F. Ye, H. Jensen, S. W. Larsen, A. Yaghmur, C. Larsen and J. Østergaard, *J. Pharm. Biomed. Anal.*, 2012, **61**, 176–183.
131 A. Lewandrowska, A. Majcher, A. Ochab-Marcinek, M. Tabaka and R. Hołyst, *Anal. Chem.*, 2013, **85**, 4051–4056.
132 J. C. Giddings and S. L. Seager, *J. Chem. Phys.*, 1960, **33**, 1579–1580.
133 A. Alizadeh, C. A. Nieto de Castro and W. A. Wakeham, *Int. J. Thermophys.*, 1980, **1**, 243–284.
134 W. L. Hulse and R. T. Forbes, *Int. J. Pharm.*, 2011, **411**, 64–68.
135 T. Le Saux and H. Cottet, *Anal. Chem.*, 2008, **80**, 1829–1832.
136 H. Cottet, M. Martin, A. Papillaud, E. Souaïd, H. Collet and A. Commeyras, *Biomacromolecules*, 2007, **8**, 3235–3243.
137 L. Leclercq and H. Cottet, *Anal. Chem.*, 2012, **84**, 1740–1743.
138 B. M. Belongia and J. C. Baygents, *J. Colloid Interface Sci.*, 1997, **195**, 19–31.
139 J. Chamieh, A. Domènech Tarrat, C. Doudou, V. Jannin, F. Demarne and H. Cottet, *Int. J. Pharm.*, 2019, **559**, 228–234.
140 U. Franzen, C. Vermehren, H. Jensen and J. Østergaard, *Electrophoresis*, 2011, **32**, 738–748.
141 F. d'Orlyé, A. Varenne and P. Gareil, *J. Chromatogr. A*, 2008, **1204**, 226–232.
142 F. Oukacine, A. Morel, I. Desvignes and H. Cottet, *J. Chromatogr. A*, 2015, **1426**, 220–225.
143 M. Höldrich, S. Liu, M. Epe and M. Lämmerhofer, *Talanta*, 2017, **167**, 67–74.
144 W. Hulse and R. Forbes, *Int. J. Pharm.*, 2011, **416**, 394–397.
145 A. Ibrahim, R. Meyrueix, G. Pouliquen, Y. P. Chan and H. Cottet, *Anal. Bioanal. Chem.*, 2013, **405**, 5369–5379.
146 H. Zaman, A. G. Bright, K. Adams, D. M. Goodall and R. T. Forbes, *Int. J. Pharm.*, 2017, **522**, 98–109.
147 S. Latunde-Dada, R. Bott, K. Hampton, J. Patel and O. I. Leszczyszyn, *Anal. Methods*, 2015, **7**, 10312–10321.
148 D.-H. Tsai, F. W. DelRio, A. M. Keene, K. M. Tyner, R. I. MacCuspie, T. J. Cho, M. R. Zachariah and V. A. Hackley, *Langmuir*, 2011, **27**, 2464–2477.
149 H. Hinterwirth, S. K. Wiedmer, M. Moilanen, A. Lehner, G. Allmaier, T. Waitz, W. Lindner and M. Lämmerhofer, *J. Sep. Sci.*, 2013, **36**, 2952–2961.
150 T. L. Moore, L. Rodriguez-Lorenzo, V. Hirsch, S. Balog, D. Urban, C. Jud, B. Rothen-Rutishauser, M. Lattuada and A. Petri-Fink, *Chem. Soc. Rev.*, 2015, **44**, 6287–6305.
151 A. Bootz, V. Vogel, D. Schubert and J. Kreuter, *Eur. J. Pharm. Biopharm.*, 2004, **57**, 369–375.
152 A. Hawe, W. L. Hulse, W. Jiskoot and R. T. Forbes, *Pharm. Res.*, 2011, **28**, 2302–2310.
153 C. Leonid, N. K. Marina, V. K. Svetlana and R. Z. Aleksandr, *J. Biomed. Opt.*, 2015, **20**, 057003.
154 S. Balog, L. Rodriguez-Lorenzo, C. A. Monnier, M. Obiols-Rabasa, B. Rothen-Rutishauser, P. Schurtenberger and A. Petri-Fink, *Nanoscale*, 2015, **7**, 5991–5997.
155 T. Arakawa, D. Ejima, T. Li and J. S. Philo, *J. Pharm. Sci.*, 2010, **99**, 1674–1692.
156 I. K. Ventouri, S. Veelders, M. Passamonti, P. Endres, R. Roemling, P. J. Schoenmakers, G. W. Somsen, R. Haselberg and A. F. G. Gargano, *Anal. Chim. Acta*, 2023, **1266**, 341324.
157 W. Haiss, N. T. K. Thanh, J. Aveyard and D. G. Fernig, *Anal. Chem.*, 2007, **79**, 4215–4221.
158 A. López-Serrano, R. M. Olivas, J. S. Landaluze and C. Cámara, *Anal. Methods*, 2014, **6**, 38–56.
159 V. Filipe, A. Hawe and W. Jiskoot, *Pharm. Res.*, 2010, **27**, 796–810.
160 U. Pyell, A. H. Jalil, D. A. Urban, C. Pfeiffer, B. Pelaz and W. J. Parak, *J. Colloid Interface Sci.*, 2015, **457**, 131–140.
161 H. Cottet, J.-P. Biron, L. Cipelletti, R. Matmour and M. Martin, *Anal. Chem.*, 2010, **82**, 1793–1802.
162 J. Gouyon, A. Boudier, F. Barakat, A. Pallotta and I. Clarot, *Electrophoresis*, 2022, **43**, 2377–2391.
163 H. Cottet, J.-P. Biron and M. Martin, *Analyst*, 2014, **139**, 3552–3562.
164 J. Østergaard and H. Jensen, *Anal. Chem.*, 2009, **81**, 8644–8648.
165 L. D. Casto, K. B. Do and C. A. Baker, *Anal. Chem.*, 2019, **91**, 9451–9457.
166 S. Latunde-Dada, R. Bott, K. Hampton and O. I. Leszczyszyn, *Anal. Chem.*, 2015, **87**, 8021–8025.
167 I. Aslani, M. Khatibi and S. N. Ashrafizadeh, *Chem. Eng. Process.*, 2025, **210**, 110221.
168 M. Khatibi and S. N. Ashrafizadeh, *Anal. Chem.*, 2023, **95**, 18188–18198.
169 M. Callewaert, W. De Malsche, H. Ottevaere, H. Thienpont and G. Desmet, *J. Chromatogr. A*, 2014, **1368**, 70–81.
170 A. Ajdari, N. Bontoux and H. A. Stone, *Anal. Chem.*, 2006, **78**, 387–392.
171 A. Vikhansky, *Microfluid. Nanofluid.*, 2009, **7**, 91–95.
172 N. Bontoux, A. Pépin, Y. Chen, A. Ajdari and H. A. Stone, *Lab Chip*, 2006, **6**, 930–935.
173 J. Aubin, L. Prat, C. Xuereb and C. Gourdon, *Chem. Eng. Process.: Process Intesif.*, 2009, **48**, 554–559.
174 C.-H. Tsai, C.-H. Tai, L.-M. Fu and F.-B. Wu, *J. Micromech. Microeng.*, 2005, **15**, 377.
175 G. Lee, A. Luner, J. Marzuola and D. M. Harris, *Microfluid. Nanofluid.*, 2021, **25**, 34.
176 J. Muñoz, J. Arcos, O. Bautista and F. Méndez, *Phys. Rev. Fluids*, 2018, **3**, 084503.
177 F. Ebrahimi, M. Neek-Amal and M. Sahimi, *J. Phys. Chem. B*, 2024, **128**, 10727–10734.
178 A. K. Nayak, *Int. J. Heat Mass Transfer*, 2014, **75**, 135–144.
179 L. M. Fu, J. Y. Lin and R. J. Yang, *J. Colloid Interface Sci.*, 2003, **258**, 266–275.

180 K. Horiuchi, P. Dutta and C. F. Ivory, *AIChE J.*, 2007, **53**, 2521–2533.
181 L. Chen and A. T. Conlisk, *Biomed. Microdevices*, 2009, **11**, 251–258.
182 S. Ghosal, *Anal. Chem.*, 2002, **74**, 4198–4203.
183 S. Paul and C.-O. Ng, *Microfluid. Nanofluid.*, 2012, **12**, 237–256.
184 I. Medina, M. Toledo, F. Méndez and O. Bautista, *Chem. Eng. Sci.*, 2018, **184**, 259–272.
185 M. Peralta, O. Bautista, F. Méndez and E. Bautista, *Appl. Math. Mech.*, 2018, **39**, 667–684.
186 S. Mozafari, H. Safarzadeh and A. Sadeghi, *Int. J. Heat Mass Transfer*, 2025, **247**, 127165.
187 D. Das, N. Poddar and R. R. Kairi, *Phys. Fluids*, 2024, **36**, 092030.
188 D. Erickson and D. Li, *Langmuir*, 2002, **18**, 1883–1892.
189 M. Khatibi, S. K. Mehta, S. N. Ashrafizadeh and P. K. Mondal, *Phys. Fluids*, 2024, **36**, 073105.
190 K. N. Vasista, S. K. Mehta and S. Pati, *Chem. Eng. Process.*, 2022, **176**, 108940.
191 S. K. Mehta, B. Mondal, S. Pati and P. K. Patowari, *Colloids Surf., A*, 2022, **648**, 129215.
192 J. Zheng, X. Liu, Y. Jin, J. Dong and Q. Wang, *Chem. Eng. J.*, 2021, **414**, 128745.
193 F. Togi, T. Kubota, K. Toyama, A. Ishida and S. Harada, *Microfluid. Nanofluid.*, 2020, **24**, 57.
194 Z. Dou, Z. Zhou, J. Wang and Y. Huang, *Hydrol. Processes*, 2018, **32**, 1461–1475.
195 I. S. Haugerud, G. Linga and E. G. Flekkøy, *J. Fluid Mech.*, 2022, **944**, A53.
196 S. Sengupta, T. Dasgupta, D. Roy, M. Dejam and S. De, *Electrophoresis*, 2023, **44**, 711–724.
197 A. K. Roy, A. K. Saha and S. Debnath, *Int. Commun. Heat Mass Transfer*, 2020, **110**, 104369.
198 D. Hlushkou, F. Gritti, G. Guiochon, A. Seidel-Morgenstern and U. Tallarek, *Anal. Chem.*, 2014, **86**, 4463–4470.
199 K. Subramaniam and S. Chakraborty, *Microfluid. Nanofluid.*, 2011, **10**, 821–829.
200 A. Sadeghi, Y. Amini, M. H. Saidi and S. Chakraborty, *Anal. Chim. Acta*, 2014, **838**, 64–75.
201 W. Jiang, L. Zeng, X. Fu and Z. Wu, *J. Fluid Mech.*, 2022, **947**, A37.
202 A. Aruna, S. Barik and N. Poddar, *Phys. Fluids*, 2024, **36**, 126629.
203 A. K. Roy and O. A. Bég, *Int. Commun. Heat Mass Transfer*, 2021, **122**, 105169.
204 S. Radha, S. Barik and N. Poddar, *Phys. Rev. Fluids*, 2025, **10**, 014502.
205 P. Wang and G. Q. Chen, *Int. J. Heat Mass Transfer*, 2016, **95**, 131–141.
206 R. Sen, K. K. Mondal and R. R. Kairi, *Phys. Fluids*, 2025, **37**, 023138.
207 A. Aruna and S. Barik, *Phys. Fluids*, 2023, **35**, 033103.
208 N. Poddar, G. Saha, S. Dhar and K. K. Mondal, *Phys. Fluids*, 2022, **34**, 093603.
209 V. Biagioni and S. Cerbelli, *Anal. Chem.*, 2022, **94**, 9872–9879.
210 V. Biagioni, C. Venditti, A. Adrover, M. Giona and S. Cerbelli, *J. Chromatogr. A*, 2022, **1673**, 463110.
211 C. Venditti, V. Biagioni, A. Adrover and S. Cerbelli, *J. Chromatogr. A*, 2022, **1685**, 463623.
212 F. Gritti, *J. Chromatogr. A*, 2018, **1570**, 135–147.
213 E. Westerbeek, P. Gelin, W. Olthuis, J. Eijkel and W. De Malsche, *Anal. Chem.*, 2023, **95**, 4889–4895.
214 E. Y. Westerbeek, J. G. Bomer, W. Olthuis, J. C. T. Eijkel and W. De Malsche, *Lab Chip*, 2020, **20**, 3938–3947.
215 P. Hajiani and F. Larachi, *Chem. Eng. J.*, 2012, **203**, 492–498.
216 P. Hajiani and F. Larachi, *Chem. Eng. J.*, 2013, **223**, 454–466.
217 S. S. Wangikar, P. K. Patowari and R. D. Misra, *Microsyst. Technol.*, 2018, **24**, 3307–3320.
218 N. Nivedita, P. Ligrani and I. Papautsky, *Sci. Rep.*, 2017, **7**, 44072.
219 D. Rossi, L. Gargiulo, G. Valitov, A. Gavriilidis and L. Mazzei, *Chem. Eng. Res. Des.*, 2017, **120**, 159–170.
220 E. Y. Westerbeek, P. Gelin, I. Frankel, W. Olthuis, J. C. T. Eijkel and W. De Malsche, *J. Chromatogr. A*, 2022, **1670**, 462970.
221 M. Wiklund, R. Green and M. Ohlin, *Lab Chip*, 2012, **12**, 2438–2451.
222 B. Wang, W. Jiang, G. Chen and L. Tao, *Phys. Rev. Fluids*, 2022, **7**, 074501.
223 P. Gelin, Ö. Sardan Sukas, K. Hellemans, D. Maes and W. De Malsche, *Chem. Eng. J.*, 2019, **369**, 370–375.
224 M. R. Hossan, D. Dutta, N. Islam and P. Dutta, *Electrophoresis*, 2018, **39**, 702–731.
225 M. Karimzadeh, M. Khatibi and S. N. Ashrafizadeh, *Int. Commun. Heat Mass Transfer*, 2021, **129**, 105728.
226 M. Karimzadeh, Z. Seifollahi, M. Khatibi and S. N. Ashrafizadeh, *Electrochim. Acta*, 2021, **399**, 139376.
227 A. Alinezhad, M. Khatibi and S. N. Ashrafizadeh, *Sci. Rep.*, 2024, **14**, 18409.
228 A. Alinezhad, M. Khatibi and S. N. Ashrafizadeh, *Electrochim. Acta*, 2023, **460**, 142625.
229 A. Alinezhad, M. Khatibi and S. Nezameddin Ashrafizadeh, *J. Mol. Liq.*, 2022, **347**, 118324.
230 A. Heydari, M. Khatibi and S. N. Ashrafizadeh, *Phys. Fluids*, 2023, **35**, 082006.
231 S. Saha, P. P. Gopmandal and H. Ohshima, *Meccanica*, 2019, **54**, 2131–2149.
232 F. Li, Y. Jian, L. Chang, G. Zhao and L. Yang, *Colloids Surf., B*, 2016, **147**, 234–241.
233 U. Marini Bettolo Marconi, M. Monteferrante and S. Melchionna, *Phys. Chem. Chem. Phys.*, 2014, **16**, 25473–25482.
234 M. Reshadi and M. H. Saidi, *Chem. Eng. Sci.*, 2018, **190**, 443–458.
235 P. Koner, S. Bera and H. Ohshima, *Phys. Fluids*, 2022, **34**, 062016.
236 B. Saha, S. Chowdhury, S. Sarkar and P. P. Gopmandal, *Soft Matter*, 2024, **20**, 6458–6489.
237 A. Poddar, D. Maity, A. Bandopadhyay and S. Chakraborty, *Soft Matter*, 2016, **12**, 5968–5978.
238 M. Reshadi and M. H. Saidi, *J. Fluid Mech.*, 2019, **880**, 73–112.

239 A. Heydari, M. Khatibi and S. N. Ashrafizadeh, *Phys. Fluids*, 2024, **36**, 112026.
240 P. Koner, S. Bera and H. Ohshima, *Soft Matter*, 2023, **19**, 983–998.
241 B. Kumar and S. Jangili, *Phys. Fluids*, 2025, **37**, 032043.
242 M. Monesi, M. Khatibi and A. Rahbar-Kelishami, *Sci. Rep.*, 2022, **12**, 12170.
243 M. Karimzadeh, M. Khatibi, S. N. Ashrafizadeh and P. K. Mondal, *Phys. Chem. Chem. Phys.*, 2022, **24**, 20303–20317.
244 B. Barman, D. Kumar, P. P. Gopmandal and H. Ohshima, *Soft Matter*, 2020, **16**, 6862–6874.
245 H. Dartoomi, M. Khatibi and S. N. Ashrafizadeh, *Electrochim. Acta*, 2022, **431**, 141175.
246 H. Dartoomi, M. Khatibi and S. N. Ashrafizadeh, *Langmuir*, 2022, **38**, 10313–10330.
247 H. Dartoomi, M. Khatibi and S. N. Ashrafizadeh, *Anal. Chem.*, 2023, **95**, 1522–1531.
248 F. Li, Y. Jian, Z. Xie, Y. Liu and Q. Liu, *RSC Adv.*, 2017, **7**, 782–790.
249 M. Karimzadeh, M. Khatibi and S. N. Ashrafizadeh, *Phys. Fluids*, 2022, **34**, 122008.
250 C. J. C. Biscombe, *Angew. Chem., Int. Ed.*, 2017, **56**, 8338–8340.
251 N. Ghiya and A. Tiwari, *Phys. Fluids*, 2024, **36**, 123606.
252 M. Khatibi, A. Mojavezi and E. Pourjafarabadi, *Phys. Fluids*, 2023, **35**, 102017.
253 A. Alizadeh, W.-L. Hsu, M. Wang and H. Daiguji, *Electrophoresis*, 2021, **42**, 834–868.
254 T. M. Squires and M. Z. Bazant, *J. Fluid Mech.*, 2004, **509**, 217–252.
255 A. Rezk, J. Friend, L. Yeo and Y. Zhou, in *Microfluidic Devices for Biomedical Applications*, ed. X. Li and Y. Zhou, Woodhead Publishing, 2nd edn, 2021, pp. 125–162.
256 B. J. Kirby, *Micro- and Nanoscale Fluid Mechanics: Transport in Microfluidic Devices*, Cambridge University Press, 2010.
257 M. Khatibi and S. N. Ashrafizadeh, *Int. Commun. Heat Mass Transfer*, 2024, **154**, 107448.
258 S. Haeberle and R. Zengerle, *Lab Chip*, 2007, **7**, 1094–1110.
259 M. Khatibi, A. Aminnia and S. N. Ashrafizadeh, *Chem. Eng. Process.*, 2024, **202**, 109849.
260 P. Shahhoseini, M. Khatibi, S. N. Ashrafizadeh and J. F. L. Duval, *Electrochim. Acta*, 2025, **536**, 146756.
261 A. A. Nazari, M. Khatibi, L.-H. Yeh and S. N. Ashrafizadeh, *Desalination*, 2025, **614**, 119153.
262 R. Dolatshahi, M. Khatibi and S. N. Ashrafizadeh, *Phys. Fluids*, 2025, **37**, 102009.
263 H. Dartoomi, M. Khatibi, J. F. L. Duval and S. N. Ashrafizadeh, *Desalination*, 2025, **616**, 119378.
264 M. Zare, M. Khatibi, S. N. Ashrafizadeh and J. F. L. Duval, *Phys. Fluids*, 2025, **37**, 072035.
265 Y. Cai, R. Sun, Y. Ren and Y. Gou, *Microchem. J.*, 2025, **211**, 113101.
266 Y. Tao, Y. Gao, Z. Liu, Y. Chen, W. Liu, G. Yu and Y. Ren, *Phys. Fluids*, 2025, **37**, 082043.
267 Y. Li, Y. Ren, W. Liu, X. Chen, Y. Tao and H. Jiang, *Electrophoresis*, 2017, **38**, 983–995.
268 Q. Ruan, W. Guo, R. Yang, T. Sun, Q. Yang and Y. Ren, *Biomaterials*, 2026, **325**, 123617.
269 Q. Ruan, C. Shi, X. Lin, W. Ruan, M. Xu, C. Yang and Y. Ren, *Chem. Eng. J.*, 2025, **511**, 162099.
270 M. Dejam, H. Hassanzadeh and Z. Chen, *Chem. Eng. Sci.*, 2015, **137**, 205–215.
271 R. Ponalagusamy and D. Murugan, *Chin. J. Phys.*, 2023, **81**, 243–269.